Politecnico di Milano

SCHOOL OF INDUSTRIAL AND INFORMATION ENGINEERING

Master of Science in Energy Engineering

Energy for Development

POLITECNICO
MILANO 1863

Characterization of performance stability in Precious-Group-Metal Free PEMFC cathodes with variable thickness

Advisor:
Prof. Andrea Casalegno

Co-advisors:
Eng. Andrea Bisello
Doct. Andrea Baricci

Candidate:
Giorgia Negro
836266

Academic Year 2015-2016

Ringraziamenti

Vorrei innanzitutto ringraziare il professore Andrea Casalegno per avermi concesso la possibilità di svolgere il lavoro di tesi nell'ambiente attivo e stimolante del gruppo *MRT Fuel Cell Lab*. I miei piú sinceri ringraziamenti vanno anche a Bise, che con la sua infinita pazienza e ottimismo mi é sempre stato accanto, dall'insegnarmi la differenza tra una chiave inglese e un cacciavite, al sostenermi nei momenti di sconforto durante la scrittura. Senza di lui non ce l'avrei fatta. Ringrazio inoltre i miei compagni di sventure Prep, Mimmo, Ago e Bonaz per aver reso le lunghe giornate in laboratorio piú spensierate e per avermi sempre fatto sentire parte di 'una stessa barca'.

Le parole non saranno mai sufficienti per esprimere la gratitudine, la stima e l'affetto che provo per la mia famiglia, che ha saputo consigliarmi e sostenermi in tutte le difficoltà che ho affrontato in questi anni. Un grazie speciale va a Monica, l'amica piú speciale, l'amica di una vita, che mi ha sempre spronato a fare del mio meglio, che anche a 1100 km di distanza mi é sempre stata vicina. Ti voglio bene. Alle mie bionde Giulia e Sara vanno i miei ringraziamenti, per tutti i magnifici momenti passati insieme, dai banchi del Poli, a una barchetta traballante in mezzo all'Adriatico. Vi vorrei qui in questo giorno. Al capo delle bionde Marc va un grazie speciale, per aver sempre ascoltato i miei sproloqui dispensando abbracci ma mai insulti. Ti avessi conosciuto prima avrei la media del 27 mannaggia a te. Ringrazio tutte le persone conosciute durante questi anni di Poli, sia chi é stato solo di passaggio, sia chi é rimasto piú a lungo nella mia vita: avete tutti contribuito a rendere questa esperienza indimenticabile. Un grazie particolare va agli *Energyci* Luca, Nigo, Sparvi e Tomb, indivisibili compagni di lezione; ai Lolli, Cecio e Zua, compagni di studio e spritz. Grazie ad Anto per tutti i cappucci pre-lab, erano una delle poche gioie della giornata. E a Save per i caffé post-lab. Un grazie speciale va a Giulio, grazie honey per esserci sempre stato, per i sorrisi e le storie. Grazie Mati per le foto e le bevute di supporto, mi hai risollevato piú volte la giornata. Un pensiero va alla per me sempre piccola Carlotta, che non se ne è mai andata completamente dalla mia vita. Ringrazio i miei compagni di liceo Andy, Nella, Eli e Manu, con i quali si é stretto un legame che va ben oltre a una semplice amicizia tra i banchi di scuola. Un ringraziamento particolare va a Prez, con cui, insieme a Cami, viaggi quotidiani verso la tanta amata/odiata piscina diventavano un gioco e la cui preziosa amicizia dura da incontabili anni. Un grazie speciale va alla mia famiglia erasmus, Alicja, Christina, Gianmarco, Guillaume, e tutti gli altri, che anche dagli angoli piú remoti d'Europa mi sostiene sempre. Mi mancate ragazzi. Un grazie di cuore va a Matteo, che ha sempre saputo ricordarmi quanto valgo tutte le volte che l'ho dimenticato, che alla fine tira sempre fuori il meglio di me. E che non si aspetta mai nulla in cambio. Grazie per essere cosí speciale.

A te nonna,
che non hai mai smesso di accompagnarmi in questo viaggio

Extended Abstract

Over the last years, the attention towards power generating technologies with a limited environmental impact coupled with a high efficiency has been substantially increasing. In this context, *Polymeric Electrolyte Membrane Fuel Cells (PEMFCs)* are a promising candidate for applications in the automotive sector, stationary plants and portable devices. The cell assembly produces indeed electric energy by chemically converting suitable reactants.

The advantages coming from the employment of this technology are mainly linked with the absence of combustion processes. On one hand, the thermodynamic cycle is prevented to be subjected to the limitations imposed by the Carnot efficiency, and that significantly enhances the theoretical maximum. On the other hand, the use of hydrogen as reactant allows for an alternative to fossil fuels from the power production process: a renewable source is exploited and greenhouse gases are not emitted. The products of the functioning reaction of the *PEMFC* are essentially liquid water and an electric current flux.

In spite of the aforementioned advantages, issues concerning the performances and the durability of the material, together with the non-competitive production and maintenance costs hinders the commercialization on large scale of *Polymer Electrolyte Membrane Fuel Cells*. The replacement of unsustainable noble metal catalyst with less expensive and earth abundant materials is the main key proposal to fix the challenge of costs. The rapid development of non-precious metal catalysts with high catalytic activity has been directed towards Fe-N-C materials [35]. Despite recent advances, the volumetric activity remains below Platinum electrodes, and this low activity results in thicker electrodes with significant transport losses. The stability of *PGM-Free* catalysts still remains very poorly studied. Degradation mechanisms of these innovative structures are still mostly unclear, being dependent on type of materials and adopted fabrication process: their development results very non-homogeneous and drastic.

The present work concerns the study of the performance stability within *Precious Group Metal Free PEMFC* cathode catalyst layers, aimed at the evaluation of the influence of two key structural parameters. In detail, the morphological features that are the object of the investigation are the cathode catalyst loading and ionomer content.

In particular, the studied *PGM-Free* catalysts have been designed and fabricated by the *University of New Mexico (UNM)*, within a collaboration with *MRT Fuel Cell Lab*. They are Fe-N-C catalysts produced by means of the original *UNM Sacrificial Support Method (SSM)*, that utilizes high temperature pyrolisis in inert atmosphere to shape a material with multiple surface defects across a carbonaceous network.

The current work starts with an introduction to the main peculiarities of a *PGM-Free* catalyst layer, together with a literature insight regarding the identified possible degradation mechanisms within the structure. To date, the greatest sources of losses are identified in iron demetallation, anion binding and protonation, hydrogen peroxide and radical oxygen species formation and micropore flooding [45]. The bibliographical investigation has been completed with an analysis of numerical models in order to understand the state of the art and compare them with the mathematical tools previously developed within the *MRT* research group. The experimental data interpretation has been thus made possible by the use of an appositely developed model.

The little knowledge of the nature of the predominant mechanism characterizing the degradation of cell performances led to an exclusion-type of approach. Different sets of diagnostic techniques are tried in a preliminary analysis, the interpretation of their results gives then the information of which effects have the least impact on the *Membrane Electrode Assembly (MEA)* degradation, bringing to the later exclusion from the procedure of the tests specific to their emphasis.

A one dimensional physical model has been applied to this mainly experimental work in order to be validated by the experimental results through fitting. A sensitivity analysis is carried out in order to understand the relative importance of each amendable parameter in the model. The change of one variable at a time allows to evaluate its contribution to the shape of both polarization and electrochemical impedance spectroscopy curves. Therefore, both steady and dynamic state have been investigated. This preliminary activity is essential to be able to calibrate the model output curves so to fit the experimental ones and interpret the physical behavior within the *Membrane Electrode Assembly (MEA)*.

The definition of a *Beginning of Life (BoL)* procedure common for all the tested *MEAs* is requested to have comparable results so to make a relevant evaluation of performances degradation during the first critical hours of operation. The junction between experimental campaign and model fitting has allowed the identification of the structural parameters and operating variables that mostly affect the performances. The highest catalyst loading ends up having the highest performances in kinetically controlled regions, but undergoes a more drastic worsening at higher currents: the thickest electrode pushes the oxygen reduction reaction towards the

membrane/cathode catalyst layer interface, lowering the reaction efficiency. The utilization factor of the catalyst seems to be strictly linked with the thickness: as it increases, the electrochemical active area tends to decrease, probably due to local transport losses. Materials present a fairly homogeneous ionic conductivity, in opposition to the electronic conductivity, which suggest room for improvement in the fabrication process. Thickness is found to be a delicate parameter to be optimized since, as it increases, the kinetically controlled regime results favored, while the ohmically limited region suffers from a reaction pushed towards the membrane/catalyst layer interface. In addition, high frequency resistance is also much dependent on this parameter: as the electrode thickens, the resistance assumes an ascending trend and a higher value. The samples giving the best outputs are found to have the same thickness rather than common catalyst loading or ionomer content. Finally, due to the significant thicknesses, full activation of the cell is slow.

A longer experimental campaign has been carried out in order to qualitatively evaluate the stability trend as different parameters change. The contribution to degradation of a change in the nature of the inlet cathodic flux has been studied. Operations under air, oxygen and nitrogen have been marked with subsequent characterizations evaluating the ongoing decay. The effect of the imposition of different currents and backpressures have been evaluated in air; while in oxygen the main concern has been the understanding of the importance of the mass transport resistance on the overall performances. The analysis has been completed by subjecting the cell to an inert environment for a period of time long enough to be able to appreciate eventual alterations in the characterization curves once the cell has been put back to be fed with active reactants.

A standardization of the degradation test procedures is pursued by the last campaign of the experimental work. The final objective is the collection of comparable results along the entire lifetime of the cell, in order to be able to better characterize the observed phenomena, by associating them with a certain morphological structure of the cathode catalyst layer rather than with a certain imposed condition. Since the samples go through the same working history, the comparison between beginning and end of life is further interpreted by the mathematical model fitting. The evolution in time of the main operating parameters is hence outlined, in order to understand the deterioration pathway followed by each catalyst layer. A study of the contribution to degradation within the standardized test of a change in either the backpressure or the reactant concentration concludes the experimental work.

Physical degradation mechanisms have been observed not to be directly connected to performance losses. What instead comes out is the drastic, exponential, performance drop of the first operating hours, which strongly depends on the structure, linked to the intrinsic features affecting the internal resistance of the *MEA*. This aspect is found

to be underestimated in literature and hence the standardization of procedures has been thought as the most rigorous way of stability and durability evaluation.

The predominant phenomenon occurring in the catalyst layer appears to be the active sites loss, which, to date, can not still be associated with certainty to any particular physical degradation mechanism among the aforementioned list. The catalyst feature resulting the most affected by the aging is the solid phase conductivity, indicating that the attacks of the oxygen are mainly against the electron-conductive carbonaceous paths. This is confirmed by the behavior observed under operation in pure oxygen, during which high frequency resistance is particularly affected. A partial recovery in performance following a dry-out of the catalyst layer after O_2 feeding, suggests reversible phenomena due to micropore flooding. Operation under inert confirms the oxygen reduction reaction to be the most influencing in the decay process.

In conclusion, despite the work has concerned only Fe-N-C catalyst, the conclusions drawn from the experimental and model interpretation could be extended to any type of *PGM-Free* cathode catalysts.

Sommario Esteso

Negli ultimi anni, l'attenzione verso le tecnologie di generazione di potenza a basso impatto ambientale e ad alta efficienza è aumentata sensibilmente. In questo contesto, le *Pile a Combustibile con Membrana Elettrolitica Polimerica (PEMFCs)* sono un promettente candidato per le applicazioni nel settore automobilistico, impianti stazionari e dispositivi portatili. La cella produce infatti energia elettrica convertendo chimicamente appositi reagenti.

I vantaggi derivanti dall'impiego di questa tecnologia sono principalmente connessi con l'assenza di processi di combustione. Da una parte il ciclo termodinamico non è soggetto alle limitazioni imposte dall'efficienza di Carnot, il che innalza notevolmente il massimo teorico. D'altra parte, l'uso di idrogeno come reagente permette un'alternativa ai combustibili fossili nel processo di produzione di potenza: si sta sfruttando una risorsa rinnovabile senza emettere gas serra. I prodotti derivanti dalle reazioni di funzionamento di una *PEMFC* sono sostanzialmente acqua liquida e un flusso elettronico di corrente.

A dispetto dei vantaggi che presenta questa tecnologia, vi sono ancora alcune limitazioni alla diffusione commerciale su larga scala: le prestazioni e la durabilità dei materiali, insieme alla non competitività dei costi di produzione e manutenzione. La sostituzione di catalizzatori sintetizzati da metalli nobili con materiali facilmente e più economicamente reperibili è la risposta principale alla sfida dei costi. Il rapido sviluppo di catalizzatori da metalli non preziosi con alta attività si è incentrato su materiali Fe-N-C [35]. Nonostante i più recenti avanzamenti, l'attività volumetrica rimane ben sotto a quella ottenuta con elettrodi di platino, e questa scarsa attività risulta in elettrodi più spessi con notevoli perdite di trasporto.

Il presente lavoro si incentra sullo studio della stabilità delle prestazioni all'interno di *catalizzatori catodici privi di platino* per *PEMFC*, volto alla valutazione dell'influenza di due parametri strutturali chiave. Nello specifico, le caratteristiche morfologiche che saranno oggetto di studio sono il carico catalitico e il contenuto di ionomero all'interno del catodo. Nello specifico, i catalizzatori studiati sono stati progettati e fabbricati dalla *University of New Mexico (UNM)*, all'interno di una collaborazione con l'*MRT Fuel Cell Lab*. Questi sono catalizzatori Fe-N-C prodotti tramite la tecnica originale *UNM Sacrificial Support Method (SSM)*, che utilizza pirolisi ad alta temper-

atura in atmosfera inerte per formare un materiale con multipli difetti di superficie lungo una rete carboniosa.

Il presente lavoro si apre con un'introduzione alle principali peculiarità di un *catalizzatore catodico privo di platino* è necessaria, insieme a un approfondimento nella letteratura riguardo i possibili meccanismi di degradazione all'interno della struttura finora identificati. Le maggiori fonti di perdite sono state individuate in: demetallizzazione del ferro, agglomerazione di anioni e protonazione, formazione di perossido di idrogeno e di specie reattive dell'ossigeno, e allagamento dei micropori [45]. Lo studio bibliografico si è completato con un'analisi dei modelli presenti in letteratura, per capire qual è lo stato dell'arte e poter fare un confronto con i modelli precedentemente sviluppati dal nostro gruppo di ricerca, al fine di sviluppare uno strumento modellistico per l'interpretazione dei dati sperimentali.

La scarsa conoscenza sulla natura dei fenomeni dominanti il degrado delle prestazioni della pila ha portato a seguire una strategia di esclusione. Diverse tipologie di test sono stati inizialmente provati, l'interpretazione dei relativi risultati ha portato all'individuazione delle condizioni che hanno il minore impatto sul decadimento, dando poi la possibilità di escludere dalle procedure quei test che le evidenzierebbero.

Un modello fisico a una dimensione è stato affiancato a questo lavoro prettamente sperimentale così da poter interpretare mediante fitting i risultati ottenuti. Un'analisi di sensitività è stata portata a termine in modo da poter soppesare la relativa importanza di ciascun parametro che è possibile cambiare nel modello. Il cambiamento di una variabile alla volta permette la valutazione del suo contributo alla forma delle curve di polarizzazione e di spettroscopia di impedenza. unque, è stato studiato sia il comportamento in stato stazionario che dinamico. Questa attività preliminare è fondamentale per calibrare le curve di output del modello affinchè si possano fittare quelle sperimentali e si possano interpretare i meccanismi fisici all'interno della cella a combustibile.

La definizione di una procedura di inizio vita comune per tutte e celle è necessaria per poter disporre di risultati comparabili e fare valutazioni significative sul decadimento delle prestazioni durante le prime ore critiche di operazione. Grazie alla campagna sperimentale e all'interpretazione combinata col modello fisico si sono potuti valutare i parametri strutturali e variabili operative aventi maggiore influenza sulla prestazione. Il carico catalitico maggiore finisce per avere le più alte prestazioni nel regime controllato dalla cinetica, ma subisce una perdita più drastica a correnti più alte: l'elettrodo più spesso spinge la reazione di riduzione dell'ossigeno verso l'interfaccia tra membrana e catalizzatore, abbassando l'efficienza di reazione. Il fattore di utilizzo del catalizzatore sembrerebbe dipendere dallo spessore, al suo au-

mentare la superficie elettrochimica attiva tende a diminuire, probabilmente a causa delle perdite per trasporto locali. I materiali presentano proprietà di conducibilità elettronica abbastanza omogenea, al contrario della conducibilità ionica che varia tra i vari campioni, suggerendo un buon margine di miglioramento per il processo di fabbricazione del materiale. Lo spessore risulta essere un parametro delicato da ottimizzare poichè, al suo aumentare, il regime controllato cineticamente viene favorito, mentre la regione limitata ohmicamente risente dello sbilanciamento della reazione verso l'interfaccia tra membrana e catalizzatore. Inoltre, anche la resistenza ad alta frequenza è fortemente dipendente da questo parametro: incrementando lo spessore dell'elettrodo, la resistenza assume un andamento crescente e un valore più alto. I campioni relativi ai migliori risultati risultano avere tutti lo stesso valore di spessore piuttosto che uno stesso carico catalitico o contenuto di ionomero. In aggiunta, a causa degli elevati spessori, la piena attivazione del sistema è molto lenta.

Una più lunga campagna sperimentale è stata eseguita al fine di valutare qualitativamente l'andamento della stabilità al variare delle condizioni operative. Il contributo al degrado di un cambiamento nella natura del flusso in ingresso al catodo è stato studiato. Condizioni operative in aria, ossigeno e azoto sono state segnate con continue caratterizzazioni atte alla valutazione del decadimento in corso. L'effetto dell'imposizione di diverse correnti e pressioni è stato analizzato in aria; mentre in ossigeno lo scopo principale è stata la quantificazione della resistenza al trasporto di massa sulle prestazioni globali. L'analisi è stata completata sottomettendo la cella a un ambiente inerte per un periodo di tempo abbastanza lungo per poter apprezzare variazioni nelle curve di caratterizzazioni una volta che le condizioni operative di riferimento fossero ripristinate.

Una standardizzazione delle procedure dei test di degradazione è stata lo scopo dell'ultima campagna sperimentale del lavoro. L'obiettivo finale è stato infatti la raccolta di dati comparabili durante l'intera vita utile dei campioni testati, così da poter meglio caratterizzare i fenomeni osservati, associandoli a una certa struttura morfologica del catodo piuttosto che a una particolare condizione imposta. Essendo tutte le celle sottoposte alle stesse condizioni operative, il confronto tra inizio e fine vita può essere inoltre interpretato dal fitting del modello matematico. L'evoluzione nel tempo dei principali parametri operativi è perciò definita, così da poter delineare il percorso di degradazione seguito da ciascun campione. Il lavoro sperimentale è stato concluso con uno studio del contributo al degrado della pressione e della concentrazione del reagente all'interno del test standardizzato.

I meccanismi fisici di degradazione non sono stati direttamente associabili alla perdita di prestazione. Ciò che invece è stato osservato è stato un drastico, esponenziale, calo delle prestazioni nelle prime ore, che è strettamente collegato alla struttura e alle caratteristiche fisiologiche che determinano la resistenza interna del

sistema. Tale aspetto è troppo sottovalutato in letteratura per cui una procedura di testing standardizzata è stata pensata come metodo più rigoroso per la valutazione di stabilità e durabilità. Il meccanismo principale sembrerebbe la perdita di siti attivi, anche se risulta troppo complicato concludere quale sia il meccanismo fisico di degrado associato. La caratteristica del catalizzatore che si rivela essere la più influenzata dall'invecchiamento è la conduttività della fase solida, ciò indica che l'aggressione dell'ossigeno è perlopiù rivolta contro la struttura carboniosa elettro-conduttiva. Ciò è confermato dal comportamento osservato in ossigeno puro, durante il quale la resistenza ad alta frequenza è particolarmente colpita. Un parziale recupero di prestazioni è stato osservato a seguito di un periodo a bassa umidità relativa successivo alle operazioni in O_2, suggerendo l'esistenza di fenomeni reversibili dovuti all'allagamento dei micropori. Le operazioni in ambiente inerte confermano che la reazione di riduzione dell'ossigeno è la principale responsabile del processo di degradazione.

In conclusione, sebbene il lavoro sia stato svolto per Fe-N-C, la procedura può essere generalizzata a tutti gli elettrodi privi di platino.

Contents

Abstract

The significant degradation of performances together with non-competitive production and maintenance costs hinders the commercialization on large scale of *Polymer Electrolyte Membrane Fuel Cells (PEMFCs)*. The most recent studies have been focusing on alternatives involving *Precious Group Metal (PGM)* free cathode catalyst layers, being the platinum the most expensive component of the system.

The present work concerns the study of the degradation phenomena occurring within Fe-N-C cathode catalyst layers, aimed at the evaluation of the influence of two key structural parameters (i.e. catalyst loading and ionomer content) on the performances and on the resistance to the decay process. An in-depth analysis of the literature has allowed to outline the main features of these materials, e.g. possible catalysis mechanisms, issues linked to transport limitations, and degradation phenomena. A standardization of procedures has been implemented in order to provide for the most comparable results and create a base case for the evaluation of the effects of further parameters alterations. The study of the steady and dynamic state operations by means of experimental data and the one dimensional physical model has allowed to relate particular output trends to the evolution of the intrinsic features of the catalyst structure. The study of the aging process has specifically emphasized a substantial, exponential, performances decay during the first hours of operation, strictly linked with a rapid in operando change of the distribution of the reacting catalytic sites. The inhibition of the active surface has been identified as a strongly limiting phenomenon. Operating conditions have been varied in order to understand the effect of a change in reactant, pressure and relative humidity. Mass transport losses have been found to be negligible. O_2 has resulted to be very aggressive on the structure, especially on the carbonaceous network; while nitrogen emphasizes the importance of reaction and its intermediates on the decay.

Finally, the aforementioned protocol could be adopted by the *PGM-Free* community, to outline the effects of structural parameters of the catalyst layer on the performance stability. It should help developing more stable catalysts for the future commercialization.

Keywords: *PEMFC* testing; *PGM-Free* catalyst; cathode; durability

Sommario

Il significativo degrado delle prestazioni unito alla non competitività dei costi di produzione e manutenzione ostacola la commercializzazione su larga scala delle *Pile a Combustibile con Membrana Elettrolitica Polimerica (PEMFCs)*. Gli studi più recenti si sono incentrati su alternative basate su *catalizzatori catodici privi di platino*, essendo questo il componente più costoso del sistema.

Il presente lavoro è volto allo studio dei fenomeni di degradazione nei catalizzatori Fe-N-C, con lo scopo di valutare l'influenza di due parametri chiave della struttura dell'elettrodo (carico catalitico e contenuto di ionomero) sulle prestazioni e sulla resistenza al processo di degrado. Un'approfondita analisi della letteratura ha permesso di delineare le principali caratteristiche di questi materiali, e.g. i possibili meccanismi di catalisi, le problematiche associate al trasporto ed ai fenomeni di degrado. Una standardizzazione delle procedure è stata adottata per ottenere risultati il più possibile comparabili e creare un caso base per la valutazione degli effetti dell'alterazione di ulteriori parametri. Lo studio delle operazioni in stato stazionario e dinamico tramite i dati sperimentali e il modello fisico a una dimensione ha permesso di trovare relazioni tra particolari andamenti nei risultati sperimentali e l'evoluzione delle caratteristiche intrinseche nella struttura catalitica. Lo studio del processo di invecchiamento ha specificatamente evidenziato un sostanziale ed esponenziale decadimento delle prestazioni nelle prime ore di operazione, strettamente connesso con un rapido cambiamento in operando della distribuzione dei siti catalitici reagenti. L'inibizione della superficie attiva è stata identificata come un fenomeno fortemente limitante. Le condizioni operative sono state fatte variare per comprendere gli effetti di un cambiamento nel reagente, pressione e umidità relativa. Le perdite per trasporto di massa si sono rivelate trascurabili. L'O_2 è risultato essere un agente aggressivo sulla struttura, specialmente sul supporto carbonioso, mentre l'azoto sottolinea l'importanza della reazione e dei suoi intermedi sul degrado.

In conclusione, tale protocollo potrebbe venire adottato dalla comunità scientifica per definire gli effetti dei parametri strutturali sulla stabilità delle prestazioni. Aiuterebbe nello sviluppo di un più stabile catalizzatore per la futura commercializzazione.

Parole chiave: *PEMFC* testing; catalizzatore privo di platino; catodo; durabilità

Introduction

Over the last years, the attention towards power generating technologies with a limited environmental impact coupled with a high efficiency has been substantially increasing. In this context, combustion-free *Polymeric Electrolyte Membrane Fuel Cells (PEMFCs)* are a promising candidate for applications in the automotive sector, stationary plants and portable devices. The cell assembly produces indeed electric energy by chemically converting suitable reactants.

The advantages coming from the employment of this technology are mainly linked with the absence of combustion processes. On one hand, the thermodynamic cycle is prevented to be subjected to the limitations imposed by the Carnot efficiency, and that significantly enhances the theoretical maximum. On the other hand, the use of hydrogen as reactant allows for the elimination of fossil fuels from the power production process: a renewable source is exploited and greenhouse gases are not emitted. The products of the functioning reaction of the *PEMFC* are essentially liquid water and an electronic current flux.

One of the main obstacles for a successful commercialization of the *PEMFC* is its non-competitive *Levelized Cost Of Energy (LCOE)* compared to the other well-established technologies. Researches are thus focusing on the elimination of the platinum used as a catalyst on the cathode side of the membrane, since it represents the most expensive component of the system.

Another factor hindering a large-scale diffusion is identified in the low reliability of the assembly. Particularly for automotive applications, the employed equipment is required to have good stability and durability. However, despite the subsequent and numerous studies, the phenomena behind the malfunctioning and the degradation of the *PEMFCs* are still not completely clear.

The present work concerns the study of the degradation phenomena occurring within *Precious Group Metal (PGM) Free PEMFC* cathode catalyst layers, aimed at the evaluation of the influence of two key structural parameters on the performances and on the resistance to the irreversible aging decay. In detail, the morphological features that are the object of the investigation are the cathode catalyst loading and

ionomer content.

The work is organized as follows:

Chapter 1 Description of the working principle of a *PEMFC*, followed by its state of the art and the main challenges for the diffusion of the technology. Introduction to the main features of a *PGM-Free* catalyst layer. Literature insight regarding the identified possible degradation mechanisms within the structure and the numerical modeling of the cathode operation. Definition of the aim of the work.

Chapter 2 Description of the internal components of the fuel cell assembly, experimental workstation, and investigating methods used for the characterization of the performances and degradation of the *PGM-Free PEMFC*.

Chapter 3 Description of the mathematical model used to fit the experimental results: assumptions, governing equations of both steady and dynamic state operations, and solution technique are presented. Evaluation of the importance of each operating parameter through a sensitivity analysis.

Chapter 4 Definition of the *Beginning of Life (BoL)* procedure common for all the tested cells. Evaluation of performances degradation due to the first critical hours of operation. Fitting of the model variables aimed at outlining the nature of the losses. Comparisons of behaviors of structurally different catalyst layers.

Chapter 5 Study of the contribution to degradation of a change in the nature of the inlet cathodic flux. Evaluation of performances under different galvanostatic regimes.

Chapter 6 Standardization of a long lasting procedure intended to allow for the most comparable output. Fitting of the model variables aimed at linking specific losses with specific catalyst morphology. Evaluation of performances degradation rate by means of quantitative and qualitative diagnostics. Study of the contribution to degradation within the standardized test of a change in either the backpressure or the reactant concentration.

State of the Art of the PEMFC 1

In this initial section, a panoramic view of the area of interest of this work and its development state is provided.

At first, the working principles of a polymer electrolyte membrane fuel cell are described, together with advantages and disadvantages of the technology in the perspective of the future targets established by the *U.S. Department of Energy*. In this context the non-precious metal catalysts are introduced as the topic of the current study. In particular, the focus is represented by the degradation mechanisms characterizing the beginning of life of the cell assembly. An insight in the literature concerning the modeling of the cathodic electrode behavior follows.

The chapter ends with a schematic explanation of the purposes of this experimental thesis.

1.1 Working principle of the PEMFC

A fuel cell is a electrochemical device able to produce electric energy straight from the oxidation of a fuel, without the use of thermodynamic cycles, which are restricted by the limitations imposed by the Carnot efficiency.

The two poles of the system, anode and cathode, are fed continuously by the flows of fuel and oxidant correspondingly. The reactions happening on the catalytic electrodes generate an electric potential difference *Open Circuit Voltage - OCV,* that is exploited by forcing the electrons to go through an external circuit from anode to cathode, so to obtain direct current. The two sides are separated by an electrolytic membrane, designed to be an electrical insulator while allowing the selective passage of protons.

Fuel cells are generally categorized according to the type of electrolyte that has been applied: *PEMFCs* use a polymeric material (*PEM, Polymer Electrolyte Membrane*). The conceptual structure of a low temperature, H_2-fed polymeric fuel cell is represented in *Figure 1.1*.
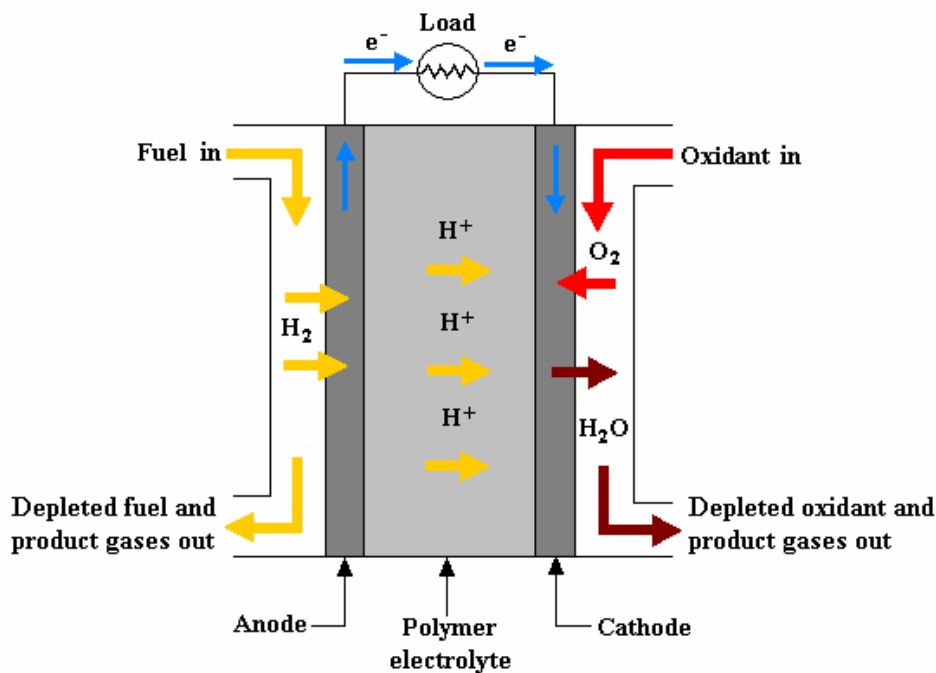
Fig. 1.1.: Operating scheme of a PEMFC

As evinced by the scheme, the anodic feeding reactant is saturated hydrogen, which is oxidized (*Hydrogen Oxidation Reaction - HOR*) to form protons H^+ and electrons e-. The process includes a series of elementary chemical steps, which provide for the formation and the reaction of several intermediate compounds, whose global stoichiometry can be written as follows:

$$2H_2 \rightarrow 4H^+ + 4e^- \tag{1.1}$$

With a reversible potential $E_a^0 = 0$ V vs SHE (Standard Hydrogen Electrode), where the superscript 0 stands for the reference conditions of 1 atm and 298 K that all components have at unit activity.

The reaction must be catalyzed at the low operational temperature of 80°C: platinum particles deposed on a carbon support fulfill this task. The anodic flues consist in the non-converted reactants, as the fuel utilization factor is not unitary.

Generated electrons and protons are consumed at the cathode, which is reached by the first through an external path (making in this way available to an user some effective work) and by the latter through the polymeric membrane. The oxygen delivered to the cathode then undergoes reduction (*Oxygen Reduction Reaction - ORR*) producing water. Globally this is expressed by:

$$O_2 + 4H^+ + 4e^- \rightarrow 2H_2O \tag{1.2}$$

With a reversible potential $E_c^0 = 1.23$ V vs SHE.

The sluggish kinetics of the *ORR* (five order of magnitudes slower than the *HOR* [4]) demands for a strong catalytic action, which, in traditional *PEMFC*, is promoted by platinum. The cathodic flues consist in the non-converted oxygen, the non-reacting inert (if present in the inlet flow) and the produced water.

In conclusion, the redox reaction carried out by the system results from the combined effect of the semi-reactions *1.1* and *1.2*:

$$2H_2 + O_2 \rightarrow 2H_2O \tag{1.3}$$

The voltage drop between the two electrodes of $E^0 = 1.23$ V vs SHE originates from the corresponding difference in chemical potentials. It is thus possible to introduce/extract electric work in/from the system. The potential at equilibrium (E_{eq}) is calculated by means of the Nernst equation:

$$E_{eq} = E^0 - \frac{RT^0}{nF} ln \frac{\prod_i^{red} a_i^{\nu_i}}{\prod_j^{ox} a_j^{\nu_j}} \tag{1.4}$$

Where *a* are the semi-reaction species activities involved in the reduction (*i*) and oxidation (*j*), associated to the corresponding stoichiometric coefficient ν; R is the gas constant, T^0 the reference temperature, F the Faraday constant and n the number of exchanged electrons. On the other hand, during real life operations, the *OCV* appears to be substantially lower, due to the presence of many irreversibilities leading actual conditions away from the theoretical maximum.

In the long term run, *PEMFCs* are expected to be able to replace fossil fuels, especially in automotive applications, by using hydrogen produced from renewable sources and avoiding the emission of greenhouse gases. The low functioning temperatures

and the lower heating value of H_2 (120.1 MJ kg^{-1}) also represent an advantage. Research must therefore focus on increasing the competitiveness of this technology, improving efficiency, lifetime and infrastructure.

1.2 Future targets and challenges

Cost and durability are the major challenges to fuel cell commercialization. In order to displace established technologies in the marketplace, fuel cells must provide advantages over the incumbent technology (such as increased efficiency and lower emissions) at similar cost and durability.
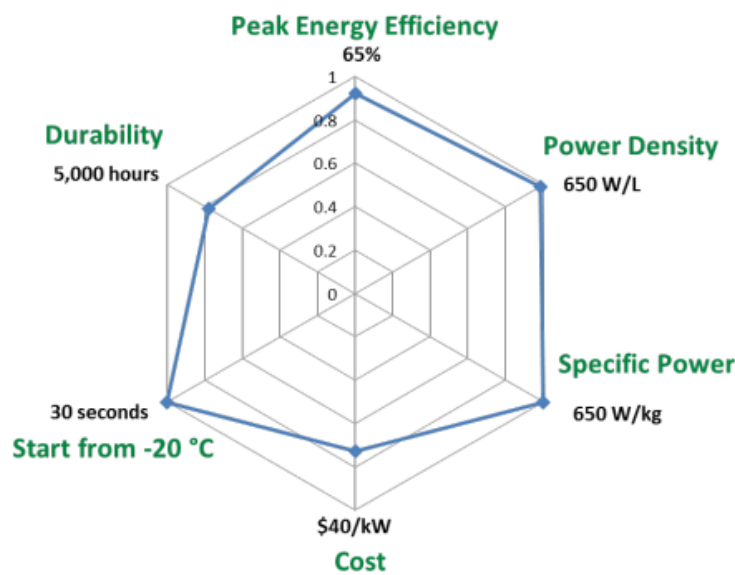

Fig. 1.2.: Fuel cells 2020 targets versus 2015 status (blue). The current status is indicated as a fraction of the targets

Of particular interest is the automotive application, with a focus on light-duty vehicles. 2020 targets of the research and development program of the *U.S. Department of Energy (DoE)* are schematized by *Figure 1.2 [12]*.

The system cost target is 40 $ kW^{-1}, which is believed to be the point where fuel cell vehicles would be competitive on a life-cycle cost basis with incumbent and future competing technologies. Cost status is for a modeled system when manufactured at a volume of 500,000 units per year. A significant fraction of the cost of a *PEM* fuel cell comes from the *Precious Group Metal (PGM)* catalysts that are currently used on the anode and especially on the cathode for the electrochemical reactions. The durability goal of 5,000 hours is equivalent to approximately 150,000 miles of driving. The durability of catalysts can be compromised by platinum sintering and dissolution, especially under conditions of load-cycling and high electrode potentials.

Carbon support corrosion is another challenge at high electrode potentials and can worsen under load cycling. Membrane durability is affected instead by both humidity variations, which cause mechanical stresses from swelling and shrinking, and chemical degradation, which can be accelerated by products coming from the bipolar plates (which are also a good part of the stack cost) and other components. Cost, efficiency, and packaging of components for air, thermal, and water management are also barriers to the commercialization of fuel cells in transportation applications. Air management is an obstacle because today's compressor technologies are not optimized for automotive fuel cell applications. The low working temperatures create a small differential between the operating and ambient temperatures necessitating therefore large heat exchangers and humidifiers. These components increase the cost and complexity of the system and use some of the power that is produced, reducing the overall efficiency. Additional efforts would be needed for the integration of components into a complete automotive system that meets durability requirements in real-world conditions, since the projected cost status is based on an analysis of state-of-the-art components that have been developed and demonstrated only at laboratory scale.

In this context, the efforts of the research community are going towards a reduction of the costs by means of the employment of alternative cathode catalysts free of precious materials.

1.3 State of the art of the *PGM-Free PEMFC*

The state of the art of the *PGM-Free PEMFCs* is constantly being revised, several research groups have reported in the recent years significant progress in synthesis of highly active and durable catalysts. At the heart of improving non-precious electrodes lies the mystery of the atomic scale structure of the active sites. Due to the pyrolysis of precursors in the catalytic materials synthesis, a wide variety of structures are formed and understanding which component is responsible for *ORR* activity is still debated. The following paragraphs are thus intended to offer an updated view of the cathode structure, highlighting the features that has to be met in order to have an activity and a durability that would make the *PGM-Free PEMFCs* competitive with platinum based cells. On the other side, the utilization of Earth-abundant materials triggers degradation mechanisms not yet faced by traditional *PEMFCs*: those have been looked for in literature and consequently summarized.

1.3.1 Catalyst structure

The challenge for an innovative electrode morphology consists in linking the structure to the function: *ORR* activity depends on the active sites density (*SD*) within the

material and the turnover frequency of the sites (*TOF*). This is made explicit by the following relationship [30]:

$$i[A\,g^{-1}] = F[A\,s\,mol^{-1}] \cdot TOF[electrons\,site^{-1}\,s^{-1}] \cdot SD[mol\,g^{-1}] \qquad (1.5)$$

where *i* is the gravimetric current density. Ideally, a material would have a high *SD* of high *TOF* sites, so that many neighboring sites are easily interconnected and reachable by electrons and protons, while keeping a high number of electrochemical conversions per second that the single catalytic site executes. However, exposure to electrochemical environments, which generally present an acidic and oxidative atmosphere, may lead to corrosive attacks or poisonings of active sites leading to a loss of activity. As such, active sites should be resistant to these phenomena, in order to successfully function under the requested operating conditions for long periods. It is thus necessary to relate *ORR* with the morphology of the catalyst, taking into account the probability of a certain variation of the structures to happen and the stability they may have relative to other structures [19].

One rapidly developing class of *PGM-Free CCL* are nanomaterials based on transition Metal-Carbon-Nitrogen (*M-N-C*) network, where nitrogen helps attach the transition metals to the underlying carbon support creating the *ORR* active sites [21]. Transition metals have been preferred to pure ones by observing a much smaller current density of the latter compared to Pt/C catalysts. Transition metal macrocyclic compounds are rather interesting as they provide various pathways for reducing oxygen, as described later in the section.

Carbon support works as a conductive support, which acts as a bridge between catalyst particles and establishes a continuous electronic pathway, while being chemically stable in acidic media. Active sites structures can be broken down into sites containing transition metals (metal bearing) and those that do not (metal free). By means of X-ray Photoelectron Spectroscopy (*XPS*), it has been documented that materials synthesized with metal precursors lead to significantly more active *ORR* catalysts [42] but it is possible that either the metal itself is a central part of the active site or acts to template formation of specific *ORR* active C-N structures. This distinction is made more complicated due to trace amounts of transition metals in many "metal free" materials [39]. The structure of the active sites is elusive for two reasons. First, the non-crystallographic ordering of the metal atoms requires the use of specific spectroscopic techniques; second, the simultaneous presence of *ORR* active sites along with other metal based phases prevents the recording of the spectroscopic fingerprint of active sites [48]. Evaluation of the *Electrochemically Active Surface Area (ECSA)* is hence hardly manageable.

Density-Functional-Theory (*DFT*) based simulations have predicted the thermodynamic stability of TM-N_x (x = 2, 4) sites embedded in monolayer graphene modeled as the carbon support of *PGM-Free* catalysts; and the *ORR* pathway to be dependent on the level of TM-N_x coordination chemistry in the catalyst [47]. The unique

experimental identification of the reaction pathway, especially how many sites are involved in *ORR* is challenging. For example, an observed net 4 e⁻ cathodic reaction (as seen in *Equation 1.2*) does not necessarily require a single site. The peroxide reaction intermediate can desorb from the first site and interact with another site that promotes the reduction of peroxide to the final product as seen in the following equations:

$$O_2 + 2H^+ + 2e^- \rightarrow H_2O_2 \qquad (1.6)$$

$$H_2O_2 + 2H^+ + 2e^- \rightarrow 2H_2O \qquad (1.7)$$
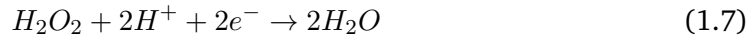
This possibility may especially occur in thicker electrodes where the probability of the desorbed intermediate to encounter a second site is comparatively high and *ORR* would be identified as a 4 e⁻ process rather than a dual site 2 x 2 e⁻ process. It is remarkable that, intrinsically, *PGM-Free CCLs* are on average ten-times thicker than Pt/C based catalysts ($\sim 100\mu m$ vs $\sim 10\mu m$) due to their low activity. Increasing the electrode thickness increases the proton and oxygen transport resistance, as well as making the cathode more susceptible to liquid water flooding. Therefore, understanding the relationship between catalyst architecture and performance is crucial for optimizing this thick component. According to the operating condition of the cell, it is observed that the *ORR* is far from being homogeneously distributed within the catalyst layer: it can be focused either near the membrane or at the interface with the *Gas Diffusion Layer (GDL)*. This depends on the status of the ionic/electronic pathways, which can be affected by several factors, ranging from the age of the *Membrane Electrode Assembly (MEA)*, the compression level and Nafion hydration [2].

The present work focuses on iron-based catalysts due to the nature of the tested samples. It has been proposed that most of the Fe-N-C catalytic sites consist of an iron cation coordinated by four pyridinic functionalities attached to the edges of two graphitic sheets [7]. *DFT* computations [23] show that the formation of graphitic in-plane Fe–N$_4$ sites in a carbon matrix is energetically favorable over the formation of Fe–N$_2$ sites: $\Delta E_{Fe-N_4} = 1.83\,eV$ vs $\Delta E_{Fe-N_2} = 4.39\,eV$, where the lowest formation energy indicates the highest relative stability. O$_2$ is chemisorbed on Fe–N$_4$ and Fe–N$_2$ sites, indicating that both sites initialize *ORR*, but Fe–N$_4$ sites are predicted to be prime candidate sites for ORR due to their higher stability and working electrode potential compared to Fe–N$_2$ sites.

The method involving the preparation of such electrodes includes sputtering and pyrolisis. An optimal heat treatment temperature is required as the ligands become denatured at high temperature, whereas catalyst formation does not take place at low temperatures. Moreover, this process helps in stabilization of transition metal macrocyclic complexes, as they lack of stability in acidic environment. During the pyrolysis at temperatures higher than 800°C, the carbon support is partly gasified, resulting in a mass loss dependent on the duration of the treatment. The disordered

domains of the carbon support are preferentially gasified [7]. As a result, micropores (where the catalytic sites are hosted) are created in the carbon black particles. To a certain mass loss corresponds a certain activity, which has to be seeked through the *CCL* preparation method. The technology underlying the catalysts employed in this experimental work comes from the *University of New Mexico*: the so-called *Sacrificial Support Method (SSM)* synthesis, by means of high temperature pyrolysis in inert atmosphere and following etching of the sacrificial support template, produces material with multiple surface defects within a carbonaceous network and an internal network of connected pores with tunable size distribution [38]. In order to meet automobile specifications, *SSM* has been optimized to: increase the number of defects and hence the dispersion of active sites in graphene nano-sheets, ensure integration of Nafion in the Fe-N-C catalyst, and improve water management in *MEA*. The pore structure is formed by two mechanisms: the removal of the silica support and the decomposition of organic molecules. Porosity and pore size distribution can be controlled by varying the silica to organic precursor ratio and/or by type of silica. The use of the *SSM* for the synthesis of the catalysts requires precursors that are: (1) carbon rich (preferring a disordered carbon content) - the amount of carbon atoms in the molecule of the N-C precursor should be high enough to form a porous, open-frame and microporous matrix as mentioned above, (2) nitrogen rich - as synthesis is performed in an inert atmosphere, all the nitrogen-containing moieties must be formed from nitrogen contained in the precursor itself and (3) thermally stable - volatile N-C precursors cannot be utilized [37] since the formation of active sites starts at temperatures higher than 700°C. The choice is not trivial: NH_3-pyrolized catalysts exhibit a much higher activity than Ar-pyrolized ones, thanks to the formation of nitrogen groups having a higher basicity boosting the intrinsic *ORR* activity of $Fe-N_4-C_{12}$ moieties through chemical or electronic effects; but on the other hands they are much less durable, mostly due to a protonation and anion-binding effect of the same highly-basic surface N-groups [25].

Within the *MEA* there is a complex interplay between catalyst and ionomer affecting its overall performance [27]. The latter is made of the same Nafion as the polymeric membrane and provides for the transportation of ions to active sites and serves as a media to remove water from them. The effect of ionomer-to-catalyst ratio on the performance has to be understood and optimized. While the kinetic performance improves with higher Nafion content, likely due to better ionic transport and conductivity that create a greater number of interfaces with catalyst particles, the mass transport is hindered due to excess ionomer or water blocking the pores. Diffusion of produced water away from the active site is hampered, inducing flooding especially at higher current densities. One of the possible explanations for this loss in the performance is the excess Nafion separating the catalyst particles, breaking the electronic pathway and losing electronic conductivity. Examples of different ionomer content can be observed in *Figure 1.3 [27]*, where the intensity of color

shows the local density of the material.

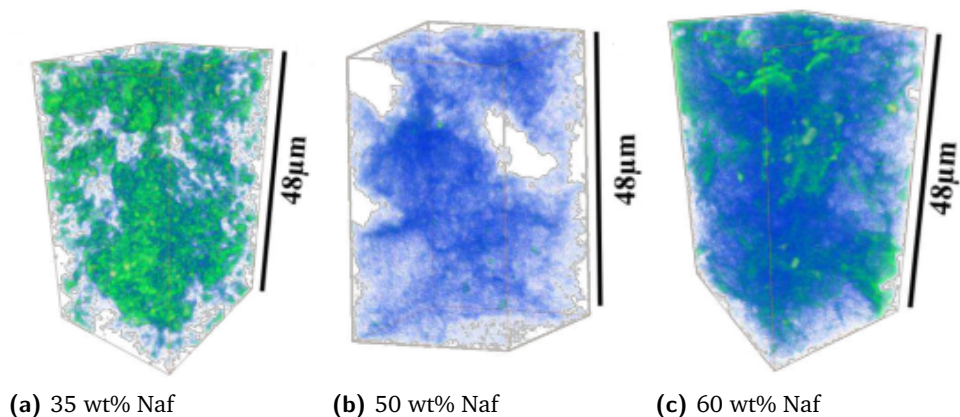One way of compensating performance losses due to excess Nafion is to add conduc-

<div align="center">

(a) 35 wt% Naf   **(b)** 50 wt% Naf   **(c)** 60 wt% Naf

</div>

Fig. 1.3.: 3D volume renderings of *PGM-Free CCLs*

tive material, such as carbon [37]. Ideal carbon additive should improve conductivity and should not change the composition of the electrocatalysts by introducing chemical groups that may compromise its stability. Introduction of amorphous carbon and surface oxides may increase hydrophilicity, cause flooding and increase carbon corrosion hindering activity. Introduction of excess of graphitic carbon may on the other hand enhance hydrophobicity and worsen water transport properties. A trade-off must be thus reached according to each specific case.

1.3.2 Degradation mechanisms

Major advances in the *ORR* activity and power density of *PGM-Free PEMFCs* have been reported, the next scientific steps include an improved understanding of the degradation mechanisms. The necessity to integrate Fe-N_x-C_y moieties at the edge of or within the graphene sheets made the catalyst structure intrinsically more prone to degradation when subjected to high electric potential than Pt/C based cells.

Using the data set available in literature, it becomes clear that there are two distinct time frames involved in stability (where stability is defined as performance loss following constant voltage/constant current experiments [3]) loss during *MEA* testing: a rapid - exponential - loss in the first 15 hours, and a more gradual but persistent loss during testing. Due to the rapid nature and magnitude of the initial worsening, its study is of critical importance.

Concerning durability, defined as performance loss following voltage cycling [3], the catalyst might be severely deteriorated by start-stop cycling (1.0-1.5 V) since the most of the catalyst is carbon: during the procedure surface oxides causing carbon corrosion are formed; they generate a passive film on the catalyst surface lowering the performances. Complete oxidation of carbon is also possible, which results in a

permanent loss of the material from the electrode [17].

Certainly the majority of work in the literature has focused on stability, with only limited studies on voltage cycling durability. This is likely due to the fact that only recently have *PGM-Free PEMFCs* demonstrated sufficient performance to warrant durability/voltage cycling experiments. On the other hand, the stability of the catalyst is inevitably tested during routine performance measurements, and thus significantly more data has been obtained for this mode of degradation. Accordingly, the present work is intended to deepen the nature of the stability degradation mechanisms. Four particular phenomena have been identified as the possible main reasons of this cell behavior: leaching of the non-precious metal catalyst, attack by H_2O_2 (and/or free radicals),protonation of the active site or protonation of a N species neighboring the active site followed by anion adsorption, and micropore flooding. The first two mechanisms are linked to the loss of active sites, coming from their irreversible oxidation; while the other two are associated with deactivation, so change in chemical nature of, or inaccessibility of reactants to, the active sites.

The next paragraphs are dedicated to an attentive description of each one of them.

Iron demetallation   Fe-rich Fe-N-C catalysts comprising a significant amount of inactive Fe particles are often characterized by a highly graphitic structure, since such Fe-based structures catalyze graphitization during pyrolysis [13]. The advantages of highly graphitic catalysts such as high resistance to chemical or electrochemical oxidation, and promotion for the formation or activation of other active species, like specific surface N groups, may not be fully exploited if they concomitantly release massive amounts of inactive Fe in PEMFCs. In recent studies [9], using an operando spectroscopic analysis, it has been demonstrated that demetallation of Fe-N-C catalysts initiates only below 0.7-0.8 V_{RHE} but predominantly originates from the *ORR*-inactive Fe species, as schematized in *Figure 1.4 [9]*, where inactive Fe particles exposed to the electrolyte are leached out during electrochemical operation after operando reduction from ferric to ferrous species.

Even though Fe leaching from *ORR*-inactive Fe species results intrinsically in no significant *ORR* activity decay, the released Fe ions may however still cause serious problems inside the *MEA*, such as the partial exchange of protons in the ionomer or the production of highly reactive radicals upon reactions with H_2O_2, whose consequences are discussed in the next paragraph. Therefore, the complete removal of leachable inactive Fe species before *MEA* fabrication might be pivotal for the successful introduction of Fe-N-C catalysts in commercial *PEMFC* systems.

Generally, an acid-washing step is applied after the synthesis of Fe-N-C catalysts and before electrochemical testing, in order to eliminate the inactive Fe species that are not completely surrounded by a carbon layer. This is a straightforward but fairly effective method, as previously confirmed by reduced bulk Fe contents in the catalysts following the acid washing [10]. Nevertheless, the acid washing has been proved
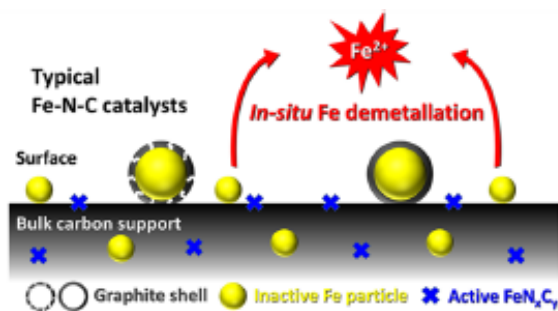
Fig. 1.4.: Polymorphic Fe-N-C catalyst including inactive Fe particles and active Fe moieties

[9] not to be able to fully dissolve the inactive Fe species exposed to the electrolyte. Any Fe particle that survives from the acid washing has therefore been assumed to be acid-stable, a property that has been assigned to the presence of a relatively high surface potential (~ 0.9 V_{RHE}) continuous graphitic layer surrounding such particles. Once the potential decreases, the experimentally observed Fe demetallation below 0.7 V_{RHE} strongly suggests that Fe ions are released in the electrolyte in the form of ferrous ions as a consequence of the reduction of insoluble Fe species with higher oxidation state: i.e. ferric species. To minimize the operando Fe demetallation, a
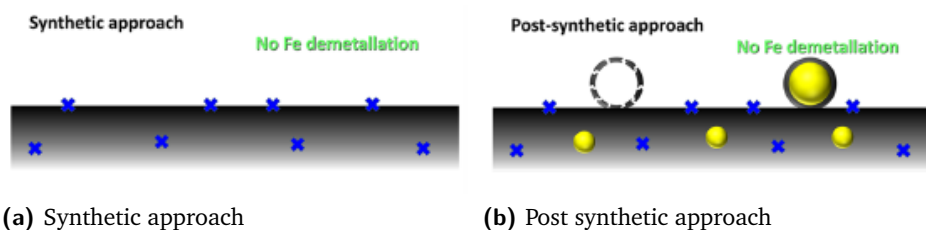

(a) Synthetic approach **(b)** Post synthetic approach

**Fig. 1.5.:** Fe demetallation minimization strategies

synthetic strategy for the preparation of the catalysts free from inactive Fe particles has been successfully applied (*Figure 1.5a [9]*). Alternatively, it has been also demonstrated that ex-situ electrochemical *Cyclic Voltammetry (CV)*, chemical control of *OCV* using SnCl$_2$ in an HCl solution, and their combination are highly effective to remove, after synthesis, inactive Fe species from the surface of the electrode without concurring loss of catalytic activity (*Figure 1.5b [9]*).

In conclusion, while Fe leaching is potentially important for prolonged fuel cell operation, short durability tests have showed that operando Fe demetallation is not a primary degradation mechanism for Fe-N-C catalysts during 5-50 h of operation [9].

Hydrogen peroxide/Radical oxygen species formation The oxygen reduction reaction happening at the fuel cell cathode can develop according to two different pathways. One is a 4 e$^-$ pathway in which O$_2$ is reduced to 2H$_2$O; the other is a 2 e$^-$ reduction of O$_2$ to the intermediate H$_2$O$_2$, which can be further oxidized on the

same site, or on another one, or can proceed in oxidative attacks against the active sites. The 4 e$^-$ *ORR* is thus always the desired pathway.

While the percentage of H_2O_2 produced during *ORR* is often not much higher on

$$O_2 \rightarrow O_{2,ad} \leftrightarrow H_2O_{2,ad} \rightarrow H_2O$$
$$H_2O_2$$
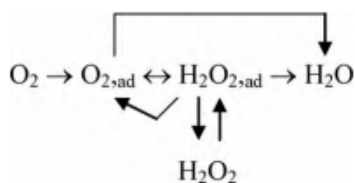
Fe-N-C than on Pt/C catalysts [43] [20], the residence time of H_2O_2 in the electrode may be longer with Fe-N-C catalysts due to their extremely poor activity for the electro-reduction of H_2O_2 to H_2O [8] and poor activity for the chemical disproportionation of H_2O_2. Chemical disproportionation of H_2O_2 is about two orders of magnitude faster at high pH for such catalysts [41], highlighting the possibility to recycle H_2O_2 at high pH but impossibility to do so at low pH. In contrast, platinum is an excellent catalyst for both the 4 e$^-$ reduction and the 2 e$^-$ reduction of H_2O_2 to H_2O [22]. The important difference between the durability of Pt/C and Fe-N-C catalysts in *PEMFC* may thus stem from their different reactivity toward H_2O_2. Moreover, chemical disproportionation of H_2O_2 on Fe-N-C catalysts via Fenton chemistry might produce a significant amount of *Radical Oxygen Species (ROS)* [16].

In order to understand the role of H_2O_2 in the degradation of Fe-N-C based cathodes during *PEMFC* steady state operation, recent studies [15] have synthesized this type of catalyst and contacted it with various amounts of H_2O_2 corresponding to ratios of moles H_2O_2 per mass of catalyst ranging over circa two orders of magnitudes. Electrochemical activity of the catalysts toward the *ORR* has been determined using the *Rotating Disc Electrode (RDE)* technique. From polarization tests, it has been evinced that activity at 0.8 V vs SHE gradually decreases with increasing amounts of H_2O_2 used during the treatment, while the diffusion-limited current density is practically unmodified. This suggests that the *ORR* mechanism is unchanged while the number of Fe-N_x-C_y active sites on the surface gradually decreases. The general trend of worsening activity with increased amount of H_2O_2 used in the treatment is however more complex at low peroxide amounts.

The same tests have been carried out for different transition metal based catalysts such as Co-N-C and Cr-N-C: the Tafel slopes appear to be constant with H_2O_2 treatment, except for pristine Fe-N-C for which the Tafel slope is slightly higher than that for treated samples. It follows that *ORR* activity decay after H_2O_2 treatment strongly depends on the nature of the metal in Me-N-C catalysts, which in turn suggests that the oxidizing species degrading the catalysts is not H_2O_2 but rather the *ROS* generated via a Fenton reaction between transition metal atoms and H_2O_2. This is supported by the lower fluoride concentration and lower degradation measured for Co-N-C than for Fe-N-C after peroxide treatment.

The *Extended X-ray Absorption Fine Structure (EXAFS)* and the corresponding *X-ray*

Absorption Near Edge Structure (XANES) spectra of the Fe-based series show that the coordination chemistry of the Fe atoms remaining in the samples after H_2O_2 treatment is identical to the one before treatment, while the metal content decreases and *ORR* activity super-proportionally worsens. The bulk-averaging nature of the detection leads to maintain the normalized *XANES* and *EXAFS* spectra unchanged even after a complete removal of top surface sites if similar $Fe-N_x-C_y$ moieties are present both on the top surface and in the bulk of pristine Fe-N-C,. Hence, identical spectra before and after H_2O_2 treatment suggest that only a fraction of the $Fe-N_x-C_y$ moieties existing in pristine Fe-N-C are located on the top surface and so contributing to *ORR* activity. Alternatively, if a major fraction of moieties is located on the top surface initially, the results suggest a drastic reduction of the turnover frequency for *ORR* of the remaining $Fe-N_x-C_y$ moieties. In this second hypothesis, the fact that no modification of the spectra is observed, means that the oxidation mostly occurs on the N-doped carbon matrix.

Through *XPS*, a dramatic increase of total oxygen content after H_2O_2 treatment is made explicit. This is correlated with a large decrease in ORR activity. Surface oxidation of carbon thus seems to be the main degradation route during reaction with H_2O_2.

From a comparison between ex situ and operando degradation, the chemical attack of Fe-N-C by H_2O_2 and *ROS* seems to be the main degradation mechanism in steady-state operation. To mitigate this main degradation mechanism, four strategies may be adopted: 1) synthesis of catalysts that minimizes percentage of H_2O_2 during oxygen reduction, 2) synthesis of catalysts that do not form *ROS* in the presence of H_2O_2, 3) addition of radical scavengers.

Protonation and Anion-binding   The activity of Fe-N-C catalysts prepared through pyrolysis in NH_3 is mostly imparted by acid-resistant FeN_4 sites whose turnover frequency for the O_2 reduction can be regulated by fine chemical changes of the catalyst surface.

Specific N-groups on the catalyst surface (and not involved in Fe coordination) protonate in acidic medium and bind anions, resulting in activity decay. The time scale for anion binding, and therefore for activity decay, greatly depends on the anion pervasiveness in the electrolyte: slow in a polymer electrolyte and fast in a liquid electrolyte. This has been demonstrated by investigating the effects of acid-washing on Fe-N-C catalysts [18]. It has been revealed that about half of the activity decay can be recovered ex situ either chemically or thermally at 300°C in argon, a temperature at which no new active sites can be formed. Possibly, an increase in *ORR* turnover frequency of catalytic sites that were already present in the acid-washed catalyst takes place. This recovery coincides with the removal of anions that bound on the surface during the acid washing. Anion binding during acid washing implies the presence of positively charged groups on the catalyst surface.

Direct anion binding onto Fe ions can be discarded since no coordination change of Fe ions is detected by Mössbauer spectroscopy. Hence, the positively charged sites necessary to explain anion retention upon acid washing and rinsing could result from the protonation of surface functionalities having a basic character. Likely, these functionalities on the catalyst surface may be N functionalities. While the experimental results demonstrate that protonation of basic N-groups along with anion binding is marked by a decreased turnover frequency of FeN_4 sites for the *ORR*, the chemical state of the basic N-groups corresponding to the initial high turnover frequency of FeN_4 sites appears to be protonated but not anion bound.

The protonation of basic N-groups on the cathode catalyst surface may also occur as soon as the *PEMFC* generates current. Protons originating from the anode's *HOR* could protonate basic N-groups at the cathode, instead of participating in the *ORR*. In a *PEMFC* cathode, the amount of protons fixed on specific N-groups is significant, especially if these N-groups are located in micropores, and could play an important role as a relay for the protons migrating from the Nafion ionomer toward the FeN_4 centers found in the micropores. Consequently, electrons from the anode would accumulate at the cathode catalyst surface to compensate for the NH^+-groups formed at the catalyst-electrolyte interface. Anion binding is delayed in *PEMFC* due to restricted mobility of the sulfonate groups of the membrane. Two activity enhancement effects related to the protonation of neighboring N-groups and that may be negated by subsequent anion binding are: modified electron density of the catalyst surface surrounding FeN_4 moieties, and increased proton access to FeN_4 centers during the ORR.

In conclusion, combining high activity and durability will require optimizing the catalyst/electrolyte interface to prevent anion binding.

Micropore flooding Catalyst layer flooding is a well-known phenomenon that can occur at high relative humidity/current densities and leads to mass transport losses. In traditional Pt/C *PEMFC*, the flooding is not specific of micropores, but extends to the entire hierarchy of pore sizes and performance can be recovered by changing operating conditions. This is contrary to the proposed mechanism of micropore flooding in *PGM-Free PEMFCs*, where the performance loss is considered irreversible [45].

Recent studies [11] have aimed at quantifying the impact of this phenomenon to cell performance stability. The initial situation of the micropore (d < 2 nm) is schematized by *Figure 1.6 [11],* where micropores are initially partially wet, but then completely filled when current is generated in the *CCL*. Ionomer is assumed not to be able to penetrate into the micropores, since Nafion micelles range in size from 1–5 nm [36]. The effect of micropore flooding can be evaluated by means of in situ polarization and *CV*.

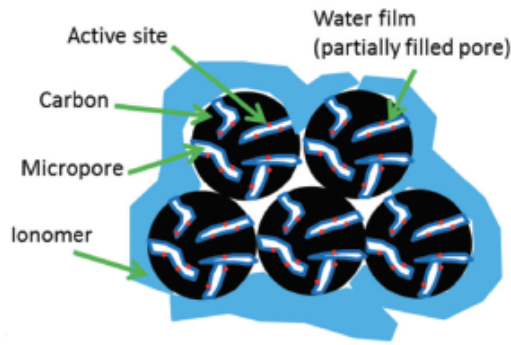Specific of the *CV*, the double layer capacitance of the electrode is directly propor-

Fig. 1.6.: Partially filled micropores

tional to the electrochemically accessible surface area of the conductive catalyst particles. The growth in double layer charging current is expected to happen as these pores are flooded and the active area is increased. However, experimentally [45], only little change in double layer charging current is verified while the tests are executed distanced in time. In order to understand whether this is simply *CCL* wetting in the traditional sense (i.e. wetting of a higher percentage of the total catalyst layer and not just micropores), or whether this is evidence for the irreversible micropore flooding mechanism, polarization curves under both air and O_2 are necessary. Specifically, mass transport limitations appear at much smaller current densities under air than under O_2 due to the $\sim$5 times lower oxygen concentration in air vs pure O_2. Thus, if the active sites remain stable, but become less accessible due to flooding of the micropores, then polarization curves are supposed to present no change in the low current density performance, but significantly higher mass transport losses even for the O_2 polarization curve, as O_2 is forced to transport through the liquid water to the active sites. The experimental result does not show
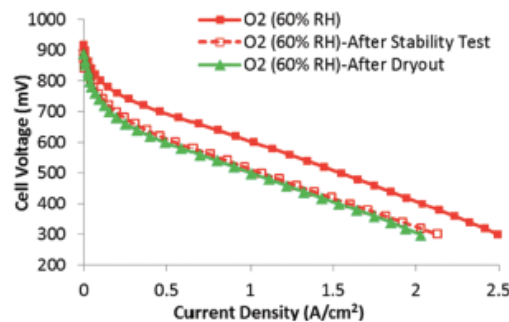

Fig. 1.7.: Polarization curves for 'micropore flooding' testing

higher mass transport losses following the stability test, as would be expected if micropore flooding was indeed responsible for the low performance. This is further confirmed by analyzing the O_2 polarization curves (*Figure 1.7 [11]*), which show a kinetic loss (loss and/or deactivation of active sites, represented by a parallel shift to lower voltages at every current density)) after the stability test. The polarization curve following an extreme dry-out protocol designed to remove any water filling

the macropores of the catalyst layer, confirms the kinetic nature of the degradation. Most likely, micropore flooding has a minor contribution to *PGM-Free PEMFC* stability.

1.4 Modeling of *PGM-Free* cathode operation

PGM-Free PEMFCs represent the potential solution to the cost and availability challenges coming from the employment of precious materials. These catalysts involve however lower volume specific activity than platinum, resulting in thicker electrodes. The use of different materials results moreover in degradation mechanisms following pathways rarely encountered in traditional catalysts, as seen in *Section 1.3.2*. It is thus fundamental to understand quantitatively how this factors impact membrane electrode assembly performance. In this sense, an attentive modeling work is required. It follows here a focus in the most recent advances [26], so to have a clear view of the state of the art being the starting point for the model developed for this current thesis. The efforts of the analyzed model aim at evaluating the effects of the electrode thickness on the *ORR*. Water flooding is studied in terms of its impact on gas-phase transport based on the decrease in effective porosity due to flooding, as well as the dilution of oxygen by water vapor and nitrogen; and on electrochemically accessible surface area (*ECSA*) by incorporating a flooding term in the kinetics model. The model is a two-region, multi-phase, transport model of an electrolyte membrane
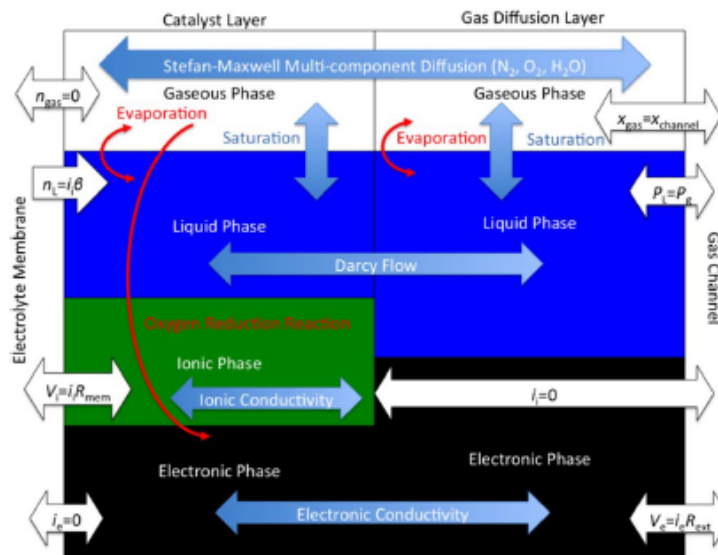

Fig. 1.8.: Cathode representing different phases and regions of the model with boundary conditions (black-outlined, white arrows), transport phenomena (blue arrows), and generation terms (red arrows)

- catalyst layer (*CL*) - gas diffusion layer (*GDL*) assembly. This one-dimensional,

steady-state model consists of two regions (*CL* and *GDL*) with the electrolyte membrane being considered as a boundary condition at the *CL* surface, as seen in *Figure 1.8 [26]*. Each region has different properties, but the governing equations are similar. Within each region there are four phases: an electron-conducting solid phase, an ion-conducting ionic phase, and non-conducting liquid and gas phases. The primary dependent variables in these phases are electronic phase potential, V_e, ionic phase potential, V_i, liquid pressure, P_l; and vapor fractions of oxygen and water vapor, x_o and x_w. Currents and species flux are also dependent variables, but can all be related to gradients of primary dependent variables. The governing equations consider the conservation of electrons, protons, liquid water, and water vapor as follows:

$$0 = -k_e \nabla^2 V_e + nF r_{ORR} \tag{1.8}$$

$$0 = -k_i \nabla^2 V_i + nF r_{ORR} \tag{1.9}$$

$$0 = -\frac{k_L}{\mu} \nabla^2 P_l + 2r_{ORR} - r_{evap} \tag{1.10}$$

$$\nabla N_w = r_{evap} \tag{1.11}$$

Where k_e is electronic conductivity, n is electrons per mole oxygen, r_{ORR} is *ORR* rate, k_i is ionic conductivity, k_L is liquid permeability (function of saturation), μ is viscosity, r_{evap} is the evaporation rate, and N_w is flux of water vapor. Flux of nitrogen in air is set to zero everywhere, since it does not participate in any reaction, and the membrane is considered to be gas-impermeable. Boundary conditions for the governing equations fall into three categories: membrane, *CL-GDL* interface, and channel. The membrane is treated as an electrical insulator with an ohmic drop. At the *CL-GDL* interface, all variables are considered continuous. The channel boundary is treated as an ionic insulator with a solid phase overpotential.

The model assumes a much lower ionic conductivity compared to the electronic conductivity, concluding that at high frequencies capacitors behave like short circuits eliminating the effect of transport and kinetics on the impedance. Consequently the *High Frequency Resistance (HFR)* becomes the ohmic resistance of the system, represented by the parallel of the solid and electrolyte (dominant) resistances. The electronic conductivity and the system resistance can be thus found by correlating *HFR* with *CCL* thickness. This has been the approach exploited in order to validate the experimental data of the current work.

Results show that, as the potential decreases outside the kinetic region, the current distribution becomes increasingly concentrated at the *CCL*/membrane interface due to ionic conductivity limitations. At the same time external ohmic losses also become more significant. Fittings with experimental data lead to the proposal of improving catalyst utilization by means of two strategies. First by decreasing loading: at high potentials increased loading means increased electrochemically active surface area, but at low potentials this increased loading only inhibits oxygen diffusion,

leading to lowered utilization and reduced performance. On the other hand, as catalyst thickness decreases, the relative importance of interfacial effects between *CL-GDL* increases. Second by optimizing sections of the *CL* for different phenomena: enhancement of gas diffusion near the *GDL* and of k_i near the membrane, so to mitigate ohmic losses resulting from poor catalyst utilization at low potentials.

1.5 Aim of the work

The global objective of the present work is a study of the degradation taking place within the cathode catalyst layer of *PGM-Free PEMFCs* with particular attention to the aspects defining the behavior of the assembly during the first hours of operation, within which the most sensitive performance decay is observed. Degradation is intended to be linked to the previously discussed chemical phenomena. While the necessity for alternatives to precious metal based *CCLs* is pressing the commercialization of M-N-C electrodes, their stability, durability and efficiency response still has a long way before actually being competitive. The full understanding of the mechanisms governing this catalyst is thus crucial in order to make meaningful adjustments to the structure.
The literature state of the art deepened in *Section 1.3* represents the starting point for the considerations made later in the dissertation on the basis of the results obtained in the experimental part of the thesis.

Consequently, the specific targets of this work can be identifies as follows:

- Interpretation of the *Beginning of Life (BoL)* of all the samples. In order to fulfill the task, an unique start-up procedure has been applied to each tested cell, so to assure having both repeatability and a mean of comparison. Considerations have been made according to the catalytic load and the Nafion content.

- Evaluation of the impact on *MEA* stability following a change in any controllable working parameter, such as type of reactant, relative humidity or pressure. This has been made possible by employing well-established diagnostic techniques and in situ measurements.

- Sensitivity analysis of operational parameters within a mathematical model developed for this specific work proposal. The effects of parameter variations are observed on polarization and *Electrochemical Impedance Spectroscopy (EIS)* curves, in order to be able to fit the experimental results and understand the importance of each parameter on the evolution of the performances.

Experimental Methodology

<div style="text-align: right; font-size: 2em;">2</div>

The purpose of this chapter is an exhaustive description of the involved experimental methodology. An attentive investigation of the structure of the *PEMFC* used in the present work, of the technical features, the functionalities and the possible problems of each components is made. An analogous approach is adopted for the characterization of the whole experimental apparatus devoted to the analysis of the behavior of the ongoing cell.

Once the material aspects of the station are cleared, the attention is moved to the practical procedures of the work: the operating conditions, the various steps of the processes, the types and the logic of the tests. The little knowledge of the nature of the predominant mechanism characterizing the quick initial degradation of cell performances led to an exclusion-type of approach. Different sets of diagnostic techniques are tried at first, the interpretation of their results gives then the information of which effects have the least impact on the *MEA* degradation, bringing to the later exclusion from the procedure of the tests specific to their emphasis.

The conclusion of the chapter leaves the complete picture of the instrumentation and their usage, allowing the consequent presentation of the experimental analysis of the *PGM-Free PEMFC* degradation phenomena.

2.1 Structure and components of the PEMFC

The internal structure of a *PGM-Free* fuel cell shows a stratified disposition of its component, just like a traditional *PEMFC*, as seen in *Figure 2.1*. The core is the *MEA (Membrane Electrode Assembly)*, which helps producing the electrochemical reaction needed to extract work. On the anode side of the *MEA*, the fuel (hydrogen) undergoes oxidation and the generated protons diffuse through the membrane to the cathode end where the oxidant (oxygen) bonds with them and receives the electrons that were separated from the fuel. *Catalyst layers* on each side enable reactions and the membrane allows protons to pass through while keeping the gases separate. In this way cell potential is maintained and current is drawn from the cell producing electricity. Symmetrically, on both sides, *Gas Diffusion Layers*, sub-gaskets, gaskets, graphite and end plates are placed.
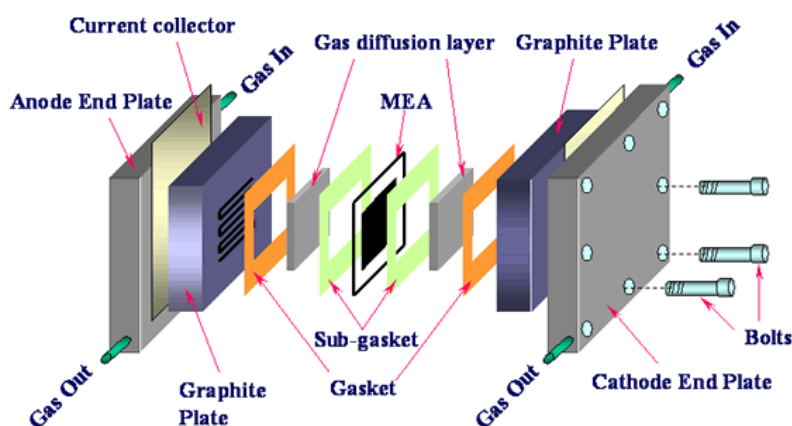

Fig. 2.1.: Internal structure of a PEMFC

The following paragraphs examine in depth the function and the specifications of each part of the whole package, starting from the membrane, moving towards the exterior.
The experimental section of this work has been carried out in collaboration with different partners: the *Department of Chemical and Biological Engineering of the University of New Mexico* who produced and tested the catalyst, and *EWII Fuel Cell* who manufactured the *MEAs*.

2.1.1 Polymeric Electrolytic Membrane

The membrane is located between the anodic and cathodic electrodes. It performs as a separator and solid electrolyte to selectively transport ions across the interfaces. The core material is polymeric, chemically resistant and durable.
Specifically, the commercial polymer *Nafion*® *XL* has been used in this work. Through the high proton conductivity, chemical resistance and durability, it is an extended-

lifetime reinforced membrane based on perfluorosulfonic acid/polytetrafluoroethylene (known as *PTFE* or *Teflon*®) copolymer in the acid (H⁺) form. When the reinforcement is combined with the chemically stabilized polymer, the membrane exhibits substantially lower fluoride ion release which helps in a longer operating durability under fuel cell conditions. In fact, the combination of F⁻ with H⁺, hydrogen fluoride (HF), becomes a corrosive and penetrating acid upon contact with moisture.

Typical thickness: $27.5\,\mu m$

Basis weight: $55/100$

The solid electrolyte plays a key role in the correct functioning of the fuel cell: it must guarantee the proton transport from anode to cathode, while blocking the electrons, electrically isolating the two poles. Acting as a physical barrier, the hindering of reactant crossover is reached.

A *Catalyst Coated Membrane (CCM)* fabrication method has been employed. It means that the Nafion containing catalyst ink is spread on a *Teflon*® support and then transferred to the proton exchange membrane by hot pressing. This support is then peeled away and the *Catalyst Coated Membrane* is sandwiched between porous carbon paper supports. It is reported that the *MEAs* prepared with the *CCM* method provide better power density due to an extended catalyst/ionomer interface and improvement of catalyst utilization.In order to enhance its protonic conductivity, Nafion must be well hydrated: this is made possible by adequately humidifying reactant gases flowing through a humidifier.

2.1.2 Catalytic electrodes

Also known as *Catalyst Layers (CL)*, the catalytic electrodes act as the promoters of the wanted electrochemical reactions. The anode side still contains $0.2\,mg_{Pt}\,cm^{-2}$, so to properly trigger the *HOR*. The resulting thickness of $20\,\mu m$ is the same for each different *MEA*. As discussed in *Section 1.3*, the biggest challenge for *PGM-Free* fuel cells is the *Cathode Catalyst Layer*: performances must be maintained high without using platinum, focusing on the *(ORR)* activity.

For this specific work proposal, *MEAs* characterized by Fe-N-C cathode catalysts synthesized by means of the *Sacrificial Support Method* (whose details can be found in *Section 1.3*) from nicarbazin (NCB)- a charge transfer organic salt - have been used. In *Figure 2.2 [37]*, images from a Transmission Electron Microscope (*TEM*) and a Scanning Electron Microscope (*SEM*) of the same catalyst used in the experimental section are presented, showing several levels of porosity originating from morphological defects formed during the decomposition of nicarbazin at high temperature.
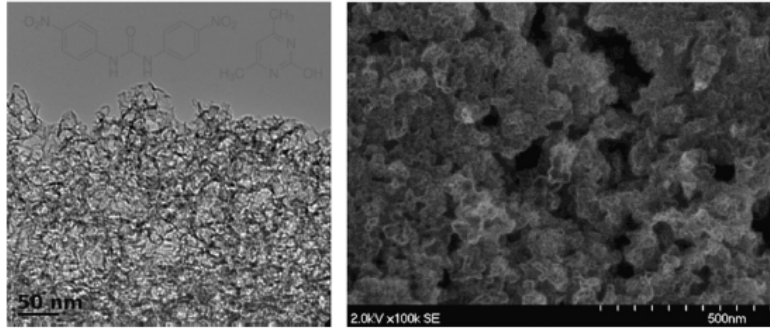
Fig. 2.2.: *TEM* and *SEM* images for the Fe-NCB *CCL*

CL's area amounts to $4.8 \cdot 4.8\,cm$. Cells with different catalyst loading have been tested: 1, 2 and $4\,mg\,cm^{-2}$. More catalyst does not necessarily mean better performances: kinetics as well as O_2 diffusion inhibition, current density and proton distribution are not function only of the number of active sites, but also of their distribution and connection, strictly linked to the thickness of the *catalyst layer*, which noticeably increases with the loading. This brings to slower reaction kinetics, poor electronic and/or protonic conductivity and mass transport limitations.

Another factor influencing layer thickness is the ionomer content. It is the same Nafion of the membrane that, within the electrode, acts to facilitate the transport of ions to active sites and the removal of water from those. A greater quantity may sound attractive thanks to the boost of kinetic performances, but it results also in a poor mass transport [44]. Samples with 35 and $45\,wt_\%$ Nafion content have been analyzed. The detailed list of the tested *MEAs* can be checked in *Appendix A*, where the unique code belonging to each cell, which from now on this work of thesis will refer to, is made explicit. Effects of catalyst loading and ionomer content on *CL* thickness are emphasized in *Table 2.1*

ACL Load	CCL Load	Nafion in CCL	ACL	CCL
$mg_{Pt}\,cm^{-2}$	$mg\,cm^{-2}$	$wt_\%$	μm	μm
0.2	1	35	20	40
0.2	2	35	20	80
0.2	4	35	20	164
0.2	1	45	20	84
0.2	2	45	20	161
0.2	4	45	20	325

Tab. 2.1.: Catalytic electrodes structures

Once the Nafion content is fixed, *CCL* thickness almost doubles going from 1 to 2 to $4\,mg\,cm^{-2}$. The same result is obtained fixing the *CCL* loading and going from 35 to $45\,wt_\%$. These values are the final products of an accurate process, which provides

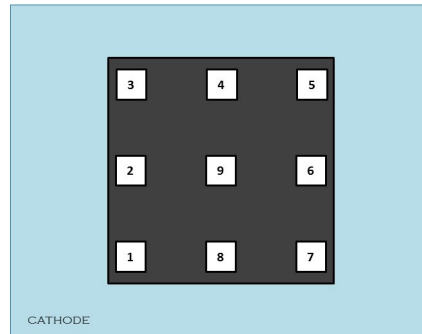for nine measures on the same sample in a systematic way, as shown in *Figure 2.3.*

Fig. 2.3.: Measures on the *MEA*

The detection has been made by means of the digital micrometer *Mitutoyo Digimatic Micrometer MDC-MX,* equipped with a friction thimble, an accuracy of $\pm 2 \, \mu m$ and a range of 0-25 mm. All the items show the same pattern with a greater thickness in the middle compared to the corners, resulting from the surface treatment used to deposit the *Catalyst Layer* on the membrane. This observation is clarified by *Figure 2.4.* The graph has been built up by systematically correlating the measures corresponding to the reference points of *Figure 2.3* acquired from two different samples of the same type of *CCL*. Each color is associated with a certain range of thickness: blue for the thinnest *1 mg 35%,* red for the *2 mg 35%/1 mg 45%,* purple for the *4 mg 35%/2 mg 45%* and green for the thickest *4 mg 45%.* The linear trend is manifest: all the *MEAs* have been gone under treatments causing the same heterogeneities in the thickness of the final structure.
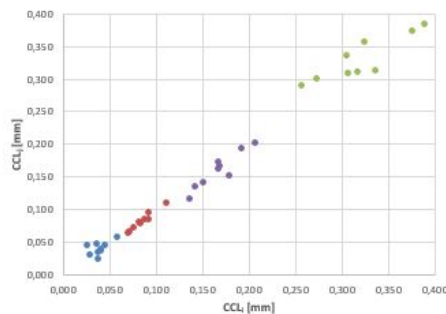

Fig. 2.4.: Correlation between measured *CCL* thicknesses

However, the standard deviation relative to the mean value of the measures is $\sim$ 20%, which, considering the accuracy of the instrument, can be considered low enough to neglect the effect of different compression on the same *MEA*. In order to decide the gasket to apply, the mean value has been taken as the reference.

2.1.3 Gas Diffusion Layers

GDLs are the regulators of the matter exchanges within the *PEMFC*, assuring a constant and uniform flow of fuel and oxidant to the active sites of the electrochemical reactions. They are supporting porous layers placed between the electrode and the reactant distributor. Their job is to The structure of each *Gas Diffusion Layer* has a carbonaceous core, organized in a planar disposition on the top of the *Catalyst Layer*. This is to provide the necessary porosity for an optimal mass transfer with the electrode and an efficient electron conductivity to and from the charge collector. Not less important is their role as mechanical support of the entire setup, thanks to their greater stiffness compared to the membrane-electrode assembly. A hydrophobic treatment enables improved water transport. In *PEM* fuel cells, specifically, water retention can result in lower power generation. Thus, *GDLs* are treated with *Teflon*® in order to make the material hydrophobic and improve water transport. *PTFE* presence is though limited, since an excessive quantity would decrease too much the electric conductivity of the component. The employed *GDLs* are provided of a *Micro Porous Layer (MPL)*, whose properties aim to minimize the contact resistance between the *GDL* and catalyst layer, limit the loss of catalyst to the *GDL* interior and help improving water management as it provides effective water transport. In the present work, the model *Sigracet*® *25BC* has been used and hand cut-out in order to provide the best fit with the *MEA*. Specifications follow.

Material	Non-woven carbon fiber paper
Thickness	$210\,\mu m$
Dimensions	$50 \cdot 50\,mm$
Basis weight	$86\,g\,m^{-2}$
Porosity	80%
PTFE content	5%
MPL presence	Yes, on one side

Tab. 2.2.: *GDL* specifications

2.1.4 Gaskets and sub-gaskets

Gaskets and sub-gaskets are placed to surround the *GDLs*, leaned against the *MEA*, in order to provide the correct compression and act as a barrier for potential fuel leaks; maximizing the highest possible efficiency. They also work as a sealing agent for the fuel cell assembly. The gasket thickness determines how much the flow fields are allowed to pinch into the electrode. In the present work, the fuel cell assembly has employed two types of gasketing material. Gaskets are made of glass fiber covered by *PTFE*, fulfilling both their sealing role and keeping the desired thickness between the graphite plates thanks to their reduced plasticity induced by

the *PTFE* content. This avoids an excessive pressing of the diffusive layer and the membrane, which could cause a partial occlusion of the distribution canals. They cover the pre-heating channels in order to avoid reactant leakages, assuring a correct stoichiometry in the central and active part of the *MEA* . Sub-gaskets, on the other hand, are made of *Mylar® Laminate*, a polyester film. Under normal conditions, in the temperature range of 40-150 °C, it does not become brittle with age because there are no plasticizers,it is dimensionally stable, chemical resistant, color consistent, non-tearing, electrically insulating, and moisture resistant (non-wettable). Consequently, it is used to protect the edges of the *MEA* and to form a better seal within a fuel cell stack. Gaskets and sub-gaskets have all been hand-shaped in order to perfectly adapt to each *GDL*. The more gaskets are applied, the less the resulting compression is. Different *Cathode Catalyst Layer* thicknesses result in a specific combination of gasket-subgasket at the cathode side for each case, setting the compression factor, as defined in *Equation 2.1* to a standard 80% . The same value is applied to the anode side, which, on the contrary, presents the same gasket and sub-gasket for any cell.

$$\beta = \frac{subgasket + gasket}{GDL+CL} \cdot 100 \tag{2.1}$$

Results are illustrated in *Table 2.3*.

(a) Anode

$Load_A$ $mg_{Pt}\,cm^{-2}$	ACL μm	Gasket$_A$ μm	SubGasket$_A$ μm	β_A %
0.2	20	125	50	76

(b) Cathode

$Load_C$ $mg\,cm^{-2}$	Nafion $wt_\%$	CCL μm	Gasket$_C$ μm	SubGasket$_C$ μm	β_C %
1	35	40	75	125	81
2	35	80	125	100	78
4	35	164	225	75	81
1	45	84	125	100	77
2	45	161	225	75	81
4	45	325	300	125	80

Tab. 2.3.: Gaskets and sub-gaskets

While the cut-out area for the cathode gasket and sub-gasket, and the anode gasket is of $5.1 \cdot 5.1\,cm$, for the anode sub-gasket is of $4.6 \cdot 4.6\,cm$, in order to give a controlled active cell area of $21.16\,cm^2$. This is due to the round shaped corner of the *catalyst layers,* as seen in *Figure 2.5*. In fact, in order to avoid a possible *crossover* of reactants by cutting the gaskets of the exact measure of the *Catalyst Layers*, a smaller and safer area has been decided.
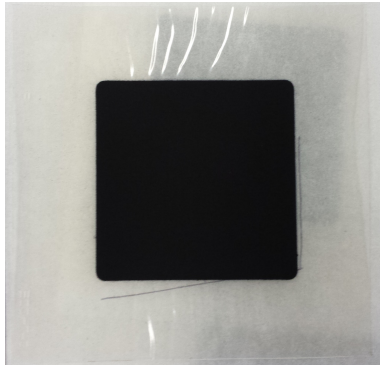
Fig. 2.5.: Example of *MEA*

2.1.5 Distributors and charge collectors

Making sure that the maximum amount of the gasses and moisture comes in contact with the membrane, the exchange of reactant and product species with the *GDL* is assured by the distributors, which are basically graphite blocks, attached to the electrode backings of a fuel cell stack on either side. In order to prevent gasses from leaking out through the normally porous graphite, the plates are constructed using a much longer and more complex process that creates a nonporous component. Another purpose of these plates is to act as a conductor by receiving the electrons from the electrodes. Lastly, they provide the necessary structural stability to support the sealing of the assembly.In the present work, among the different existent technologies, triple-serpentine distributors with a $0.8 \cdot 0.8\,mm$ square section have been used. This configuration assures a longer residence time of the reactants and a better fuel utilization factor. The graphite block is then in contact with the charge collector, which is a metallic plate, externally gilded to favor electrical conductivity. It is connected with the electrical signals coming from the cell and with the power cables going to the electronic load. The collector is isolated on the back, so not to have an electric dispersion through the following plate.

2.1.6 End plates

The last step of the assembling process is completed by means of two stainless ironed plates, clamped by eight bolts by means of a torque meter wrench, closing at $12\,Nm$. These plates serve to put solidly together all the components of the *PEMFC* around the membrane, avoiding air leakages and sustaining the whole.
Each block is also used to monitor the cell operating temperature thanks to an inner electric resistance, managed by an auxiliary thermocouple connected with the heat controller.
The reactant flux goes through the end plate, which is provided with in and out connections to the pipes. In this way, the feeding flow, which is previously heated

up by a humidifier, can keep the necessary temperature to enter the distributor's channels.

2.2 Experimental equipment

The experimental campaign has necessarily requested the realization of an appropriate plant structure, which has been gradually refined in order to face eventual unexpected faults or to investigate phenomena of specific interest. In general the overall configuration has not gone under particular changes: the equipment for long, characterization and *End Of Life - EOL* tests is the same. The workstation has been organized so to allow flexibility of intervention and control of the process variables. *Figure 2.6* shows the complete structure of the experimental equipment. A detailed description of each measure instrument is found in *Appendix B*.

Reactants arrive to the flowmeters from specific tanks by means of 5 bar-pressure pipelines. In the case of air, this is provided by a departmental compressor at 10 bar, expanded by a pressure regulator of the laboratory to 5 bar, and lead into the pipes. The regulated flux is then accurately humidified by a humidifier. The fuel cell assembly is placed on a wedge: the pre-heating pipes providing the reactants result inclined hindering eventual condensed water to enter the distribution channels.
Two pressure transducers measure the inlet pressure of the reactants, while the thermocouples keep under control the temperature along the whole pathway. Downstream the cell, pressure, temperature and relative humidity of the products are detected. This allows to quantify the water present in the anodic and cathodic flues. Once gone through this device, each separated flow enters a backpressure regulator which, by means of the set-point signal given by the manual pressure regulator, pressurizes the entire line to the desired operating condition. The appropriate temperature of each component is assured by a system managed by *PID*, made up of glow plugs and electrical resistances connected to the electric network through relays.
Fuel cell current and voltage are regulated by the electronic load which dissipates the produced energy. In the case of tests involving nitrogen, during which current is absorbed rather than generated, these parameters are managed by the power supply. The workstation is also equipped with a milliohmmeter that, measuring the voltage difference between the electrodes, yields the membrane ohmic resistance, an useful information about the status of the *MEA*.
By means of USB data acquisition boards and specific interfacing softwares, all the relevant magnitudes are sent, plotted and saved in the computer.
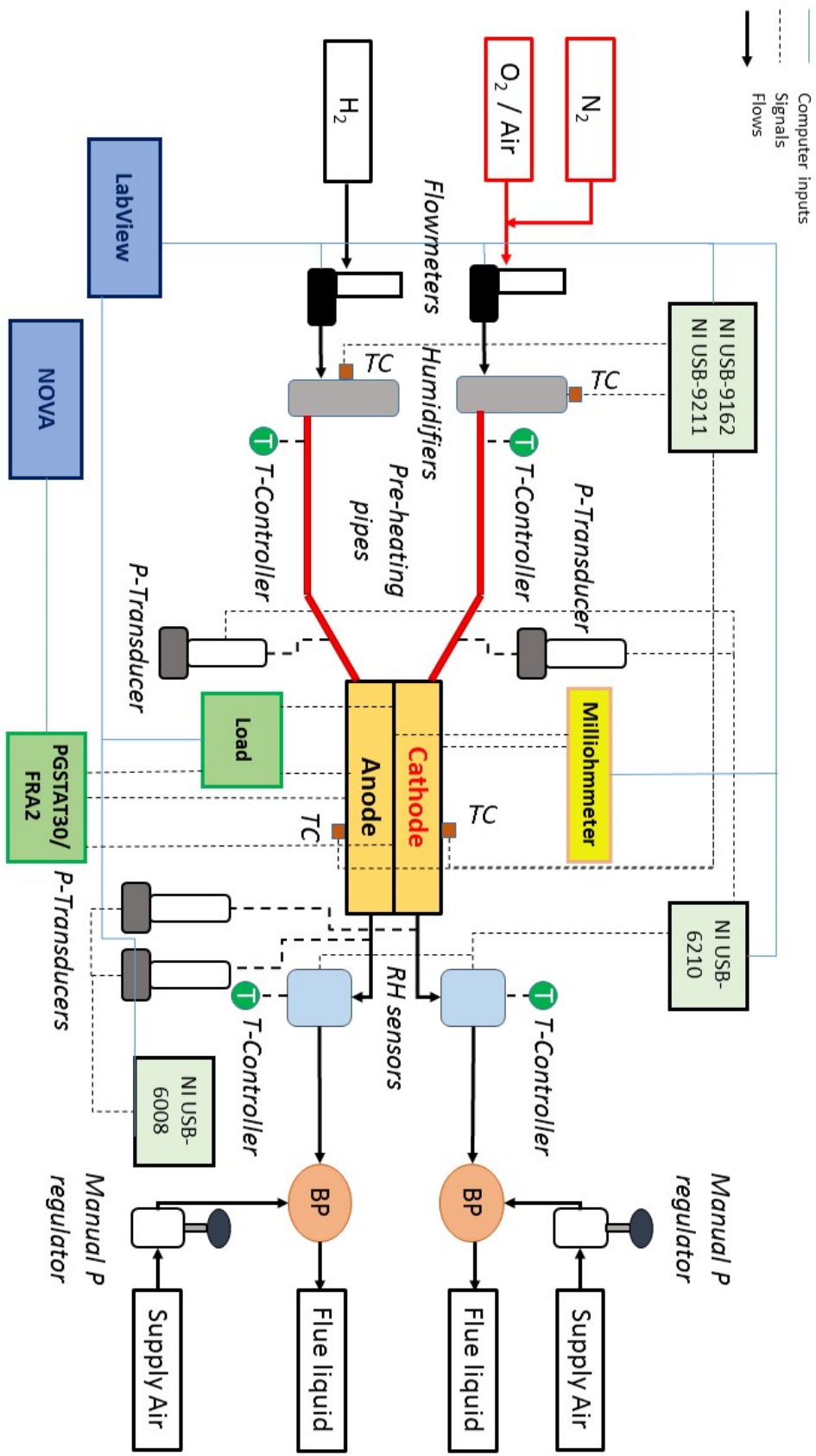
Fig. 2.6.: Workstation

2.3 Data acquisition and interpretation

Now that the complete picture of the structure of the single cell and the workstation is clear, the description of the data acquisition system, the type of tests and the data revision methods follows. This allows a complete comprehension of the experimental work, which is the basis for understanding the investigation carried out in the next chapters.

2.3.1 Set-up procedure

As previously mentioned, *MEAs* and *GDLs* used in this experimental work have been deigned by *Department of Chemical and Biological Engineering of the University of New Mexico* and fabricated by the danish *EWII Fuel Cell*. They have been then assembled in the appropriate structures, manually profiling gaskets and sub-gaskets.

Preparation is a delicate process. Gaskets must be chosen so that the triple serpentine adheres to the *GDL* without breaking through the membrane; they must be cut so to cover the pre-heating channels, be centered with the interested active area, and avoid short-circuits.

The last step prior to the cell placement in the system, provides for the checking of all leak components. For this purpose the nitrogen flowmeter feeds both the anode and cathode humidifiers, which are directly connected to their corresponding *RH* sensors, which are finally linked to the backpressure regulators. On both sides, fluxes are set to be 50 ml min^{-1} and pressure is fixed at 0.5 bar$_g$. If no pressure drop is noticed for 15 minutes, the set-up procedure can move forward, otherwise the failure must be identified with the help of water and repaired.

The structure is then sealed by the previously grease-lubricated eight bolts and the two entrance and the two exit ducts are stoppered to prevent air to get in contact and alter the *MEA*. Finally the cell assembly can be inserted in the system, tightened to the humidifiers and the humidity sensors, connected to the electric network to supply the glow plugs, monitored by two thermocouples, have the four milliohmeter and four electronic load sensing cables fixed on the gilded plates, together with the load sources wires.

Before starting the conditioning, a leakage test on the workstation must be carried out [6]. The assembly has to be organized as in *Figure 2.7*, where the nitrogen supply is connected to the hydrogen side with a flow meter followed by an isolation valve. The anode outlet gases enter then the air/O$_2$ side. The last section presents another isolation valve right after a 0-4 bar pressure gauge. At this point both the hydrogen and air/O$_2$ sides can be pressurized to 0.5, 1, 1.5, 2 bar$_g$ with a N$_2$ minimum flow of 50 ml min^{-1}. Leakages are checked in water, pipes/connections are eventually
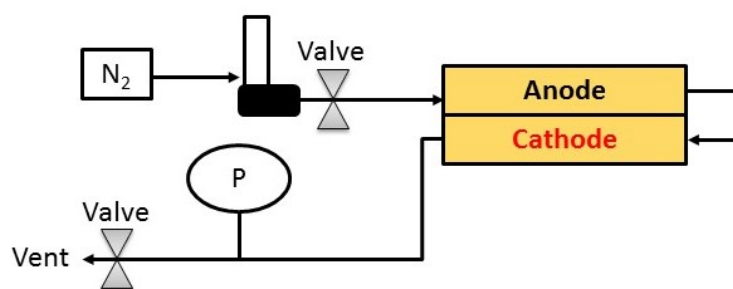
Fig. 2.7.: Leakage test

substituted. When no leaks can be observed, valves are closed and the pressure drop is recorded for five minutes.

2.3.2 Conditioning procedure

UNM researchers have provided the protocol they adopt for the *MEAs* locally fabricated, including the conditioning procedure and a first test. This has been analyzed and modified according to the cell behavior and technological availability.
The conditioning process is fundamental for a correct initialization of a new cell, and influences the lifetime performances. Below, the conditioning method proposed by *UNM* is presented, followed by the modified approach elaborated for this specific work.

UNM Method This procedure provides for a quick warming up of the cell up to $80\,°C$ under constant flows and backpressures:

	Anode	Cathode
Reactant	H_2	Air
Flow	250 ml min^{-1}	200 ml min^{-1}
BP (relative)	30 psi (2.07 bar)	30 psi (2.07 bar)

After reaching the operating conditions, the following protocol is expected:

- 10-minutes holding at 0.3 V
- Multi-range polarization - *VIR (Voltage Current Resistance)* - curve:
    - 1.0-0.6 V at 0.05 V increments with a 60 s hold
    - 0.6-0.2 V at 0.1 V increments with a 60 s hold

MRT Method The first tested cell has been initialized in the same way. However, the workstation takes one hour to warm up, which, under a flow of air and hydrogen is translated into a considerable loss of performance. In fact, the initial 15 hours of a *PGM-free* fuel cell's life present the strongest degradation, so the goal is to minimize

the impact of the warming up. The nature of this phenomenon can be seen in *Figure 2.8a*: the detected experimental data clearly follow an exponential trend, which leads to an incongruity of results already in the first characterization, as highlighted by *Figure 2.8b*. Consequently, the proposed conditioning procedure have had to be adjusted according to the limits of the workstation, in order to assure repeatability for the beginning of life of all the tested cells.

The system has been initially fed with a flow of 50 ml min^{-1} of inert N_2 at ambient pressure to both sides until the requested $80\,°C$ are reached.

(a) Exponential current decay

(b) Comparison between first characterization curves
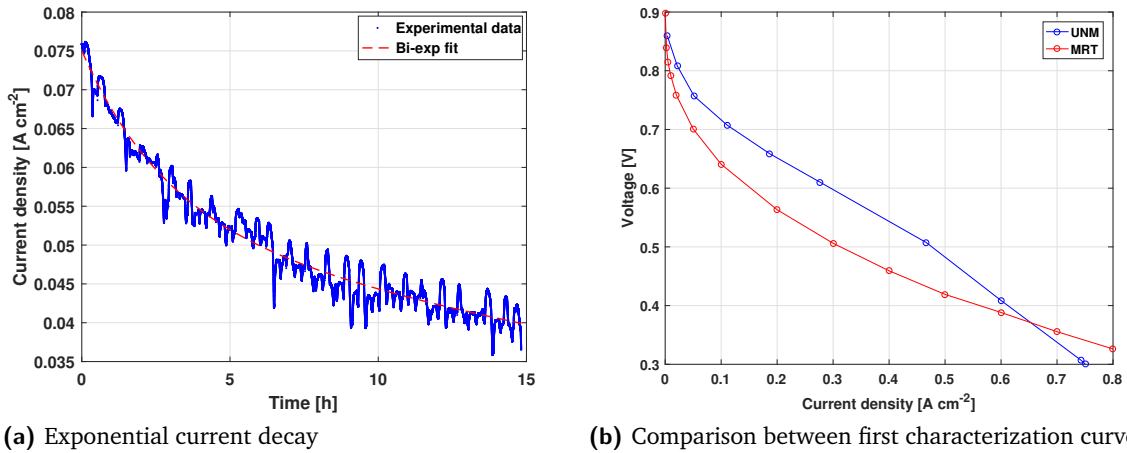
Fig. 2.8.: Example of beginning of life of a *PGM-free PEMFC*

In order to assure a homogeneous and continuous electrochemical conversion of the reactants along the *MEA*, the stoichiometry - defined as $\lambda = \dfrac{\dot{n}_{fed}}{\dot{n}_{consumed}}$ - must be greater than 1 so that a progressive starvation of the gases far from the inlet channel is avoided. A flow rate of 60 ml min^{-1} of H_2 is then enough for operation in controlled conditions during the following potentiostatic holding. Instead of 0.3 V, potential has been set to 0.6 V, the *DoE (U.S. Department of Energy)* standard reference potential. The 0.6 V benchmark depicts the resistive components of the cell and its ability to provide adequate transport of gases, electrons, and protons to the catalyst sites.

The polarization has been run in galvanostatic mode by means of *LabView* interface, so that the current is imposed and the corresponding potential is read. This procedure allows to carry out in the meantime the *Electrochemical Impedence Spectroscopy* measurement for the desired points. The reactants flow rates during the characterization have been boosted to get a stoichiometry over 10. The backpressure has been kept to 0.5 bar$_g$.

In fact the aim of the work is not to pump up the performances, but rather to comprehend the degradation process: since most of the further tests (deepened in *Section 2.3.3*) are executed under this backpressure, this has been carried out

accordingly.

Depending on its own features, each *MEA* shows a different behavior and the curve must be adjusted every time. Summarizing:

(a) Warm up

	Anode	Cathode
Reactant	N_2	N_2
Flow	50 ml min^{-1}	50 ml min^{-1}
BP (relative)	0 bar	0 bar

(b) Potentiostatic holding

	Anode	Cathode
Reactant	H_2	Air
Flow	60 ml min^{-1}	200 ml min^{-1}
BP (relative)	0.5 bar	0.5 bar
Potential	0.6 V	
Duration	10 min	

(c) Polarization test

	Anode	Cathode
Reactant	H_2	Air
Flow	500 ml min^{-1}	1000 ml min^{-1}
BP (relative)	0.5 bar	0.5 bar

Tab. 2.4.: MRT conditioning method

2.3.3 Degradation tests

There are many working parameters whose alteration has a noticeable influence on the fuel cell: temperature, pressure, feeding stoichiometries, reactant concentration. Among the activities previously developed within the laboratory, a detailed characterization of the impact of these variables on the system response in terms of *PEMFC* performance has been carried out. Concerning *PGM-Free PEMFCs*, on the other hand, this is the first work. Hence, the initial tests applied to these particular *MEAs* take the cue from them, in order to be adjusted according to the behavior of the degradation. A consistent study of the mechanisms governing the life of the cell demands for a long sequence of tests. The system is basically run nonstop for a period of time considered sufficient for the observation and comprehension of a specific phenomenon. The different procedures are indicated in the text by means of an unique code, specified in *Appendix C* which also describes all the operational features. Every test is then diagnosed using the methods explained in *Section 2.4*, so to be able to link the worsening of the recorded global performances to the responsible functional parameters. Diagnostic is thus executed at regular intervals: the less invading techniques allow measurements during the continuous operation,

while the ones requesting for an interruption are carried out at the beginning and at the end of the test. Not having adequate indications from the literature about the nature of the events happening in the *Cathode Catalyst Layer* has made the choice of procedures not trivial. The approach of the experimental campaign has been consequently purely phenomenological: each cell, especially at the beginning, has gone during its lifetime under a series of tests presenting different traits and purposes. No pre-existent schedule has been followed, apart of course the essential preliminary repeatability tests. Procedures have been thought in order to circumscribe and isolate as much as possible all the distinct contribution: every time an unexpected result has shown up, the structure of the following procedure has been appropriately shaped. The experimental campaign has consequently adopted a dynamic nature aimed at seizing the causes of the drastic performance evolution of this type of *MEA*. In practice, tests with a wide duration range (from 10 to 160 hours), different reactants (H_2, air, O_2, N_2), different degree of humidification (100, 80 or 60 % RH), different pressures (0.5 or 2 bar$_g$) and of different type (galvanostatic or potentiostatic) have been executed. The shorter procedures include conditions which have been noticed to be more aggressive, but useful for further considerations, for the cell: permanence in pure O_2 at the cathode side, or the imposition of a too high current. The effects of inerts have been studied by feeding the cathode with nitrogen. Reactants concentrations have been changed by using oxygen. The contribution of the membrane properties (mainly proton conductivity) to degradation has been weighted by varying the relative humidity. By fixing the potential, the reaction mechanism is also fixed: the effects on reaction velocity, clarified by the current response, can be observed. This kind of test has been executed at the beginning of life of all the samples, in order to have a common procedure to be compared and to highlight the drastic degradation of performances (defined by the generated current) characterizing the first hours. In order to understand the contribution of reaction velocity and its products (especially H_2O_2) on the degradation process, potentiostatic tests at a higher pressure have been carried out. On the other hand, galvanostatic tests have been useful to characterize the governing mechanisms of the cathode reaction under a determined rate. Among all the collected data, the most immediate information about the status of the system is surely given by the voltage/current response: their plot over time gives an initial overview on the degradation and, by means of the statistical analyses seen in *Section 2.3.5*, specific losses can be calculated.

2.3.4 Data acquisition system

All the tests aim at a systematic study of the phenomena, which is possible only if the relevant operating parameters are measured, memorized and reworked. The magnitudes acquired by the workstation instruments are sent to the computer

by means of USB-connected data acquisition boards. The single module carrier *NI-USB 9162,* coupled with the 24-bit *NI-USB 9211* DAQ receives the signals of the thermocouples of the cell and the humidifiers. *NI-USB 6210* is a 16-bit, 16 analog input board communicating with the upstream pressure transducers and the humidity sensors. *NI-USB 6008* is a 12-bit, 8 analog input board dedicated to the two downstream pressure transducers. *GPIB (General Purpose Interface Bus)* allows the miliohmmeter to communicate with the computer and to have a redundancy check of the data of the electronic load.A pre-existing *LabView*® interface has been refined in order to acquire and record all the information and see its development over time. Data are gathered with a frequency of 0.5 Hz. The same interface act as controller of the variables, so to be able to set humidifiers' and cell's temperature, the mass flow of the reactants, and the current or the voltage of the cell. In this way, a big amount of data is acquired in real time 24/7. Automatically, each hour, a summarizing *Matlab*® file is generated, which, applied to a specific *Matlab*® script, gives the trends in time of current density, voltage, temperature, inlet and outlet pressure, reactant flows, relative humidity, protonic resistance, and temperature of the humidity sensors. They help in understanding the processes happening in the cell during a particular test. The degree of hydration of the membrane, the electronic and protonic conductivity change, the distribution of current density, the evolution of active sites, the water quantity in the products are tried to be deduced from these graphs. The continuous recording also allows to check the stability of the cell conditions during the night and the weekend. The considerable amount of parameters acquired during the tests, together with the periodical diagnostics, is the solid starting point for the further degradation study.

2.3.5 Data analysis

As already discussed in *Section 2.3.3*, one of the obtainable results of particular interest for the degradation analysis, is given by the representation of the current/voltage value over the time abscissa. But this is just a general overview of performances. The development of an analytical method able to quantify the actual loss has become essential; in that sense a statistical method has been implemented in *Matlab*®. The first encountered problem has been represented by the great fluctuations of the acquired signal, outliers (anomalous values within a given population) had to be found and eliminated. In that sense an algorithm has been developed. It starts by calculating the median of the data, defined as the value having cumulative frequency equals to 0.5. Assuming all the measures Y_i of the measurand Y to have normal distribution, the *Mean Absolute Deviation (MAD)* is found:

$$MAD = median\,|Y_i - median(Y_i)| \tag{2.2}$$

In order to consider *MAD* as a consistent estimator for the estimation of the standard deviation σ it has been taken $\sigma = k \cdot MAD$ where k is a constant scale factor, which depends on the distribution. For normally distributed data k assumes the value of 1.4826. The measure is considered outlier if:

$$|Y_i - median(Y_i)| > 3 \cdot 1.4826 \cdot MAD \; with \, MAD > 0 \qquad (2.3)$$

Once the ouliers have been identified and excluded, the interpolation fitting method has to be decided.As noticed in *Section 2.1.2* the decay trend of a *PGM-free PEMFC* at the beginning of life is strongly exponential. For shorter and later tests, on the other hand, it has been possible to apply a more intuitive linear approach. In the below paragraphs both fittings are described in detail.

Bi-exponential interpolation An accurate analysis of the qualitative current trend over time requests necessarily a more complex approximation than a linear regression [46]: non-linear features of the first operating hours are evident. *Figure 2.9* show how a bi-exponential interpolation is a suitable fit for both the first overnight and a longer test. This mathematical model is based on a second order exponential

(a) Example of first overnight

(b) Example of long potentiostatic test
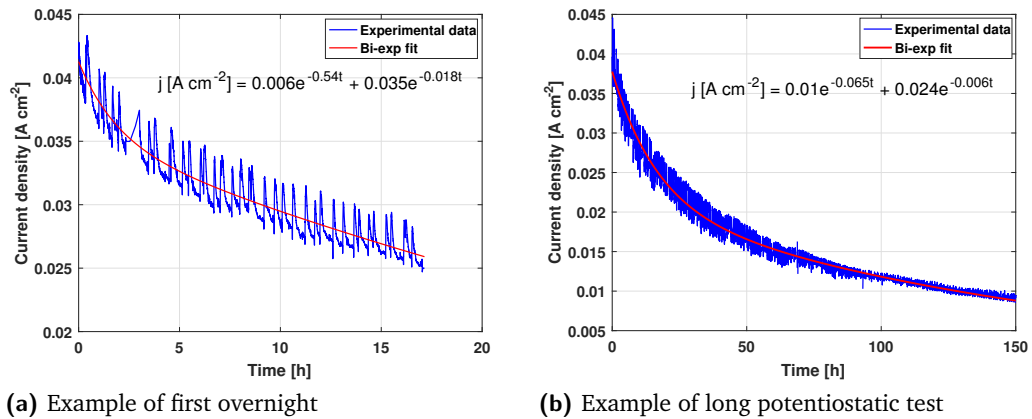
Fig. 2.9.: Applicability of the bi-exponential fitting

equation in the form of:

$$y(t) = \Phi_1 e^{-\gamma_1 t} + \Phi_2 e^{-\gamma_2 t} \qquad (2.4)$$

The four interpolation parameters are established from the cleaned experimental data by means of a specific *Matlab*® fitting function. It is evident how the obtained interpolating parameters are not easy to read. Starting from the fitted curve, though, some comparable values can be extracted, such as the global degradation rate [mA cm^{-2} h^{-1}] and the overall current loss [mA]. The consistent differences in the structure of the experimented cells have resulted in curves having the same shape but different current values. In order to improve the quality of the interpretation,

a normalization procedure has been further made by re-scaling the interested plot according to *Equation 2.5*.

$$\frac{\Delta j_{norm}}{\Delta t}\left[\frac{mA}{cm^2 h}\right] = \frac{\Delta j_{old}}{\Delta t}\cdot\frac{max(j_{ref})}{max(j_{old})} \tag{2.5}$$

This operation is clearer in practice, as seen in the case of the 2 mg samples in *Figure 2.10*. The reference (not changing) curve is the less performing one, in this case
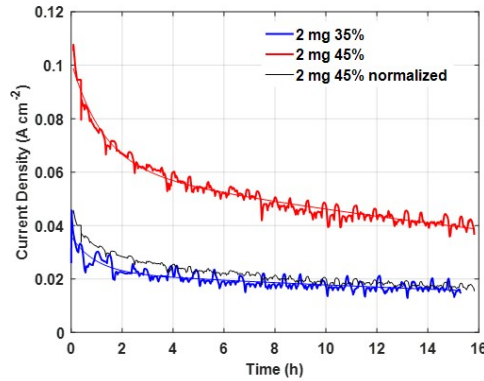

Fig. 2.10.: 2 mg 45% normalization

the 2 mg 35%. The 2 mg 45% curve is normalized on its maximum current density and gives a more sensible output. This model allows to distinguish two different behaviors of the curve: a first stretch where the slope is noticeable and exponentially shaped, causing a fast reduction of performances; and a second stretch where the decreasing rate is more subdued and the trend is quasi linear. The convenience of this approach appears when a qualitative trend of the cell current working in specific conditions has to be extrapolated. It is possible, once a time instant is fixed, to trace back the corresponding value in a more accurate way than with a linear model: a straightforward comparison in relative and especially quantitative terms between different tests can be done.

Linear interpolation   This specific statistical analysis employs the linear regression starting from the x_i and y_i values validated by the previously explained algorithm. The straight line is characterized by the parameters β_0 and β_1 (respectively the intercept and the angular coefficient), which are estimated with the ordinary least square method. Consequently the equation results to be:

$$y = \beta_0 + \beta_1 \cdot x \tag{2.6}$$

The parameter of greater interest is β_1, useful to quantitatively characterize the degradation. This approximation has been exploited to compare tests carried out later in the life of the cell, when the exponential nature of the degradation is extinguished. During the experimental work, only the galvanostatic procedures

have been worthwhile to be analyzed exploiting this approach: they have never been executed at the beginning of life and their reduced duration (10 - 30 h) suggested the slope coefficient in $[\mu V\ h^{-1}]$ to be the most effective first benchmark, as showed in *Figure 2.11*. It becomes herein evident how the linear approach allows
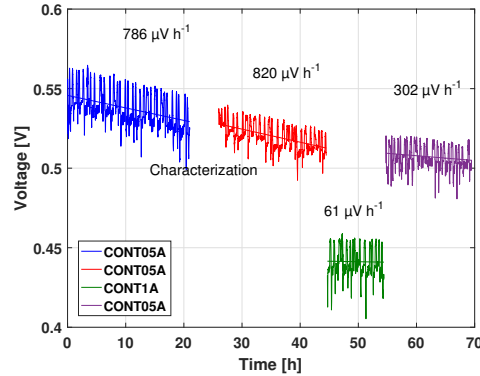

Fig. 2.11.: Example of linear fitting

to immediately evaluate and compare separate sections with a unique parameter. In this example the decay rate helps in understanding the impact of the characterization procedure and of a higher imposed current on the chosen cell reference condition of 0.5 A. It must be clarified that this is not a definitive analysis, the indicator is purely indicative and further considerations are necessary, since the amplitude of the response signal in unequivocally broad, and many and complex are the phenomena beyond a certain degradation rate.

2.4 Diagnostic techniques

The quantitative and qualitative evaluation of the phenomena regarding the degradation of the *PGM-Free PEMFC* has been done through a significant number of diagnostic techniques. These will be singularly presented in the following paragraphs, showing how each one of them allows to deepen a particular aspect of the decay and highlighting the main differences of the resulting data with respect to the traditional *Pt/C PEMFC*. All the adopted strategies find their origin in past experimental theses developed within the *MRT Fuel Cell Laboratory*, which have been adjusted according to the purposes of the present work.

2.4.1 Polarization curve

The polarization curve represents the voltage response at the cell electrodes as a function of the applied current density; it is typically the most used electrochemical technique to characterize the performance. Its trend depends on the different

potential losses, from which the contribution of the main classes of phenomena to the global degradation is deduced. Considerations concerning the shape of the curve can be made starting from *Figure 2.12*. Herein, the differences between a traditional

(a) *Pt/C PEMFC*

(b) *PGM-Free PEMFC*
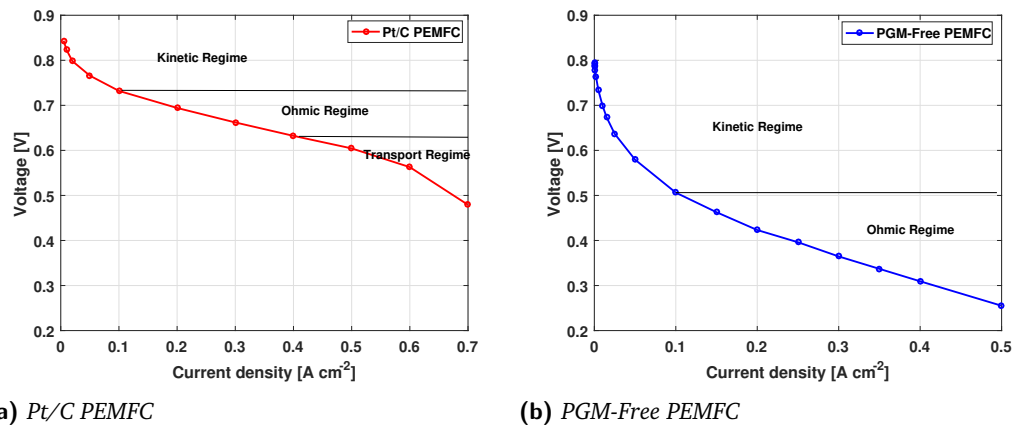
Fig. 2.12.: Examples of polarization curve

and a *PGM-Free* cell are highlighted. As foreseen by the use of non-precious materials, the overall performance is poorer, not comparable with a platinum catalyst right from the beginning of life, with a lower *OCV* and smaller reached current densities. The behavior of the *MEA* seems thus not to be affected by mass transport limitations (e.g. O_2 depletion in the *CCL* section closest to the membrane), since a slope change at the end of the polarization curve is absent, which is instead present in the *Pt/C PEMFC* plot. The effects of kinetic and ohmic losses appear on the other hand more clearly. The nature of the losses will be object of study in the further chapters. In the zone of the littlest current densities, the voltage drops due to kinetics and charge transport, that are classified as activation losses, indicating the reaction efficiency. The kinetically limiting reaction in *PEMFCs* is the cathodic *ORR*. While in *Figure 2.12a* the potential decreases logarithmically with the current density, in *Figure 2.12b* the very initial decay is more drastic, with a steeper slope. A different *CCL* utilization, consequence of its morphology, is thus noticeable: a faster deactivation of catalytic sites or the triggering of not wanted reaction mechanisms are expected to happen. The effect of the substantial thickness of the electrode (in this case $161\,\mu m$, against the $\sim 10\,\mu m$ of the Pt/C catalyst) must be also taken into account: the pathway that the protons and the reacting molecules have to undertake is much longer. An excess of ionomer tends moreover to separate the catalyst particles breaking the electronic track and decreasing electronic conductivity [37]. Those are the identified reasons of this peculiar curve shape. The ohmic regime is dominated by internal resistances: both electrical due to non-ideal electrical conductivity of the components and the corresponding contacts, and protonic due to the deterioration of the conductive Nafion (membrane and *CCL*). The resulting curve can be alternatively plotted as in *Figure 2.13*, where the current density is represented on a logarithmic scale and
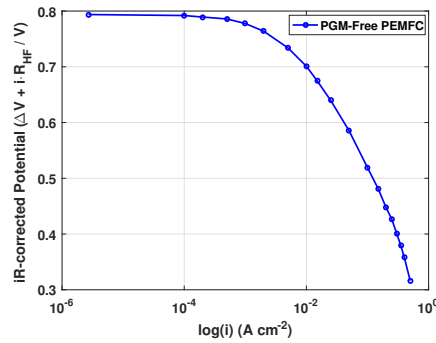
Fig. 2.13.: Example of Tafel curve

along the ordinate the voltage values are corrected for the membrane resistance *(iR-corrected)*, so to allow analysis of the electrode changes. This graph makes more clear the variation of the tafel slope along the performance curve. In this way, a change in either the *ORR* mechanism, or in the active sites density, or in both can be identified. The execution of the polarization test demands for the interruption of the ongoing degradation test, thereby it is carried out when the latest is terminated and at the end of life of the fuel cell. The curve is acquired by imposing the current density value and detecting the corresponding voltage by means of the electronic load (described in *Appendix B*). The number of points is variable according to the state of the sample (phase of life), the applied backpressure (0.5 or 2 bar$_g$), the nature of the inlet cathode flow (air, O_2, O_2 + He/N_2) and its relative humidity (60, 80, 100 % RH). Each step is held for a time period assuring the steady state of the measure, which is either 180 (for higher current densities), 60 (for current densities of 0.025 A cm^{-2} and lower) or 35 (for the *OCV*) seconds. The reference condition imposed at the beginning of the characterization equals to 0.025 A cm^{-2} and is kept for 300 s to ensure steady state conditions. In order to assure the relevance of the acquisition, currents are set in an ascending order (starting from the reference value) so to descend again once the maximum value is reached, just like the first procedure explained in *Section 2.3.2*. The detailed description of this type of test in the various working situations can be found in *Appendix C*, which also defines the codes used in the next chapters. In the present work, the curve acquired during descending current steps has been reported in order to avoid hysteresis effects. The observation of polarization curves allows to establish the loss caused by a certain degradation test, whose quantity of interest is found as the voltage/current change in the reference operating point.

2.4.2 Electrochemical Impedance Spectroscopy

The Electrochemical Impedance Spectroscopy *(EIS)* is a diagnostic technique investigating, by means of impedance detection, the property of the electrochemical

systems to accumulate and dissipate energy, through a wide range of frequencies. Impedence is a quantity defined as the measure of the time-varying resistance, given by a mean subjected to the passage of current. An advantage of the *EIS* is the possibility of measurement in operando, without having to stop it. The technique consists in introducing, thanks to the electronic load (described in *Appendix B*), a sinusoidal perturbation at the current signal applied to the fuel cell. The system produces in response a sinusoidal behavior of the voltage. As long as the amplitude of the imposed signal is small (not more than the 10% of its absolute value), the correlation between current and voltage is permitted to be considered quasi linear, greatly simplifying the analysis. The impedance value at variable frequency is thus obtained by dividing the voltage by the current sinusoidal signals. The procedure to run an *EIS* includes a frequency range going from 20 kHz to 70 mHz, split into 50 steps according to a logarithmic scale; the number of cycles is 5. Two values, one for the real and one for the imaginary part of the impedance, are associated to each frequency. On the *Nyquist* diagram they are respectively plotted along the abscissa and the ordinate. Every part of the resulting curve has a precise physical meaning: an attentive analysis is fundamental to understand which kind of phenomena take place within the cell assembly once the operating conditions change. Analogously to *Section 2.4.1*, examples of resulting curves of a traditional *Pt/C* and of a *PGM-Free PEMFC* are shown in *Figure 2.14*. Focusing on the structure of the curve in *Figure*

(a) *Pt/C PEMFC*

(b) *PGM-Free PEMFC*
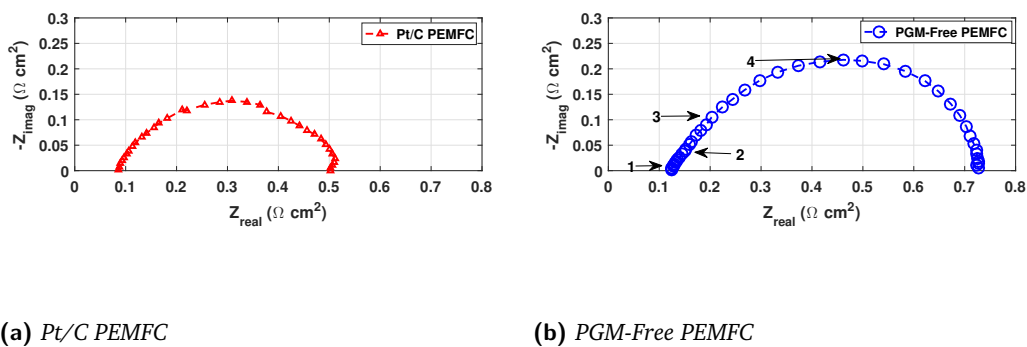
Fig. 2.14.: Examples of *EIS* at 0.2 A cm^{-2}

2.14b, features similar to the *Pt/C PEMFC* can still be observed. Arrow 1 indicates, among the very high frequency range (20 kHz - 1 kHz), the intersection point of the spectrum with the real axis, which represents the ohmic resistance of the membrane. Arrow 2 stands for a capacitive element of reduced dimensions compared to the whole spectrum, appearing at around 1 kHz, ascribed to the *Hydrogen Oxidation Reaction (HOR)* of the anode. Being this reaction more favored than the *ORR,* the detected capacity is small. Arrow 3 spans the high frequency range going from 1 kHz to 100 Hz, denoted by a 45° linear branch. This reflects the ionic resistance of the

Cathode Catalyst Layer: if the proton transport is hindered, the reaction takes place mainly close to the membrane-*CCL* interface, increasing the cathodic overpotential and generating this element. Arrow 4 touches the higher point of the semicircle, representative of the cathodic impedance of the charge transfer, strictly correlated to the activation energy barrier that has to be overcome by the charged species in order to participate in the reaction [31] [1]. Its effect is made explicit by the definition of the charge transfer coefficient that is then inserted in the formulation of the Tafel slope:

$$\alpha \;=\; \frac{RT}{2 * (-Z_{im,4})jF} \tag{2.7}$$

$$b \;=\; \frac{RT}{\alpha F} \tag{2.8}$$

Where b is obtained by the linearized Tafel law according to [33], and the impedance peak is approximated to the charge transfer resistance R_{CT}. The shape of the rest of the curve is still linked to the reaction's chemical kinetics and to the active surface of the catalyst. Finally, the value for which the real axis is intercepted for the second time, theoretically reachable at the frequency of 0 Hz, corresponds to the total resistance of the *PEMFC* and is the slope of the polarization curve in the neighborhood of the point at which the *EIS* is being carried out, assuming linearity between voltage and current values. During the experimental work, *EIS* have been executed both in operando and meanwhile polarizations. Within long potentiostatic tests, *EIS* have been run every day, at the same hour, with a certain logic: the first day of the test, the corresponding current has been read, the galvanostatic mode has been imposed and the procedure executed. This current value has been taken as cell reference value and the evolution of its corresponding *EIS* has been studied over the entire test duration. The following days, other currents have been set: the ongoing value in response to the applied voltage and a reference current common to all the *MEAs* (0.6 A). In summary, but the first day, 3 *EIS* (at least) have been run every day. Simultaneously with the polarization process, on the other hand, *EIS* have taken place always at the same current densities: 0.2, 0.1, 0.05, 0.015 A cm^{-2}. Technical details are in *Appendix C*.

2.4.3 Cyclic Voltammetry

Cyclic Voltammetry *(CV)* is an electrochemical measurement acquiring important information about kinetics and thermodynamics of electrochemical systems. In fuel cell application, it is thought to be able to evaluate the variation of the active surface happening in a degradation test. On the other hand, this procedure cannot be executed during the regular functioning: an interruption is necessary so to modify the cell configuration. Feeding flows become H$_2$/N$_2$ (50/50 ml min^{-1}). The inert

serves as feeding for the working electrode (where the potential is applied), while the anode is the reference. The potential between the electrodes goes under a cyclic variation between 0.05 V and 1 V, with a scan rate of 0.05 V s^{-1}, by means of the potentiostat described in *Appendix B*. The system output is a current density, whose trend as a function of potential is shown in *Figure 2.15b*, significantly different from its correspondent in *Pt/C MEAs*, as highlighted by *Figure 2.15a*. The voltammogram
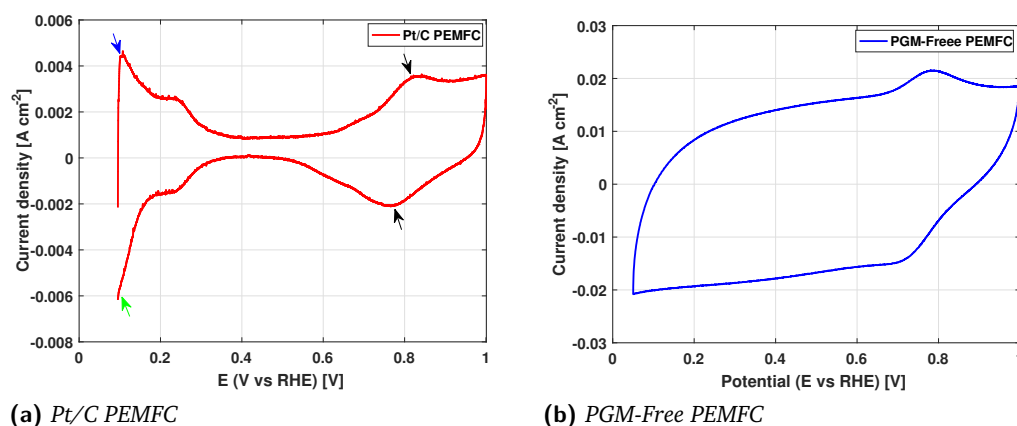

(a) *Pt/C PEMFC*

(b) *PGM-Free PEMFC*

Fig. 2.15.: Examples of *CV*

shape is dependent, in a first approximation, on: electrochemical reaction constant, diffusion coefficients, and scan rate. An initial consideration concerns the peaks of Pt oxidation/reduction in traditional *PEMFC* indicated by the black arrows: obviously they do not have the same meaning in Pt-Free curves. Hydrogen adsorption peak (blue arrow) is neither evident nor as high in *Figure 2.15b*, the same (and specular) holds for hydrogen desorption peak (green arrow). Moreover, the calculation of the *ElectroChemical Surface Area (ECSA)* - the active surface of the electrode - based on the H$_2$ adsorption charge on Pt cannot be exploited: Pt particles are not present and the *CCL* does not present the typical *PEMFC* agglomerate, but rather a carbonaceous network internally branched by interconnected pores and surface-defected material. The impossibility to obtain quantitative results has made the *CV*, during the experimental campaign, just a mean of control: the shape mutation according to different working conditions (0.5 vs 2 bar$_g$, 60 vs 80 vs 100 % RH) has been used to make qualitative observations, including double layer capacitance. Details are found in *Appendix C*.

2.4.4 Linear Sweep Voltammetry

Linear Sweep Voltammetry *(LSV)* is a diagnostic technique utilized to evaluate the integrity of the membrane, by means of the measurement of the hydrogen crossover from anode to cathode. The test consists in the imposition of a regularly increasing potential, while the associated current density is recorded and plotted,

as seen in *Figure 2.16*. Feeding flows are fully saturated at 80°C at a constant

(a) *Pt/C PEMFC*

(b) *PGM-Free PEMFC*
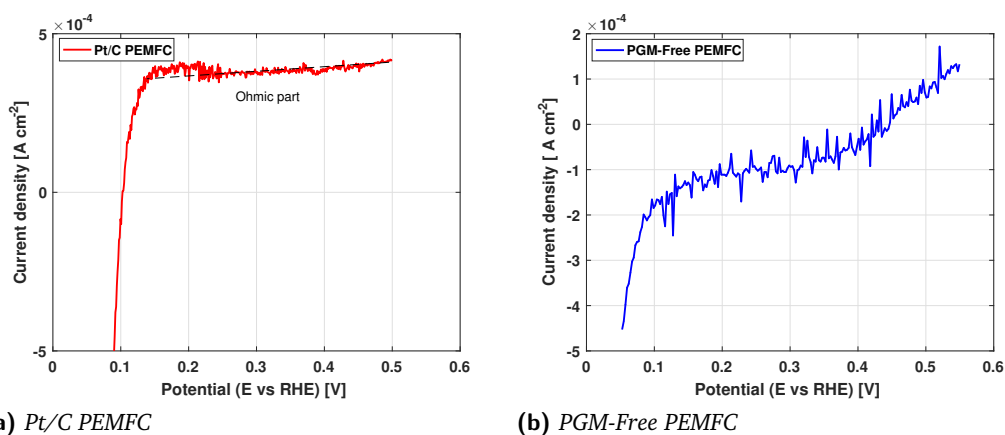
Fig. 2.16.: Examples of *LSV*

pressure of 0.5 bar$_g$ H$_2$/N$_2$ (50/50 ml min^{-1}) at the anode/cathode respectively, where the anode is the reference and the cathode the operating electrode. Potential is applied by the potentiostat (described in *Appendix B*): it starts at 0.05 V and, with a scan rate of 0.001 V s^{-1}, stops at 0.55 V. Due to the requested change of cell configuration, the measurement cannot be made in operando, but only during diagnostic phases. Details of the procedure are found in *Appendix C*. The hydrogen crossing the membrane is then oxidized in protons. The plot shows an ascending trend of the current-potential relation, up to a limiting current value representative of the phenomenon. An upward shift of this current on the graph reflects a more intense crossover and so a decay of the membrane such as a possible Nafion thinning. In *Figure 2.16a* the linearity characterizing the ohmic part of the curve up to 0.55 V is evident. Its slope *(I/V)* corresponds to the inverse of the membrane electrical resistance, whose increase mirrors the presence of inner short-circuits. On the other side, *Figure 2.16b* maintains a certain linear trend only up to a certain voltage and then the slope gets steeper. It is a behavior that has been observed to be more or less pronounced according to which cell has been examined.

2.4.5 Catalyst Layer resistance

Catalyst Layer *(CL)* resistance is a measure of the ionic resistance profile of the ionomer within the *Cathode Catalyst Layer* and of the ohmic resistance of the Nafion membrane by means of an *EIS*. The procedure starts with the application of the desired potential through the potentiostat (described in *Appendix B*) on the working electrode. The potentiostatic procedure operates in a frequency range going from 10 kHz to 1 Hz, with a number of frequencies of 10 per decade. H$_2$/N$_2$ (50/50 ml min^{-1}) feed the reference and the working electrode correspondingly. Under such conditions, during the impedance measurement, the differential current response to

differential oscillatory sinusoidal voltage is associated with the charging/discharging of the double layer at the test electrode. Once again the interruption of degradation tests is indispensable, thus this measure can be undertaken only during diagnostic phases. At very high frequencies, the impedance response consists mainly of the ohmic membrane resistance, considering the hydrogen electrode impedance to be negligible. As the frequency is decreased, both the real and imaginary components
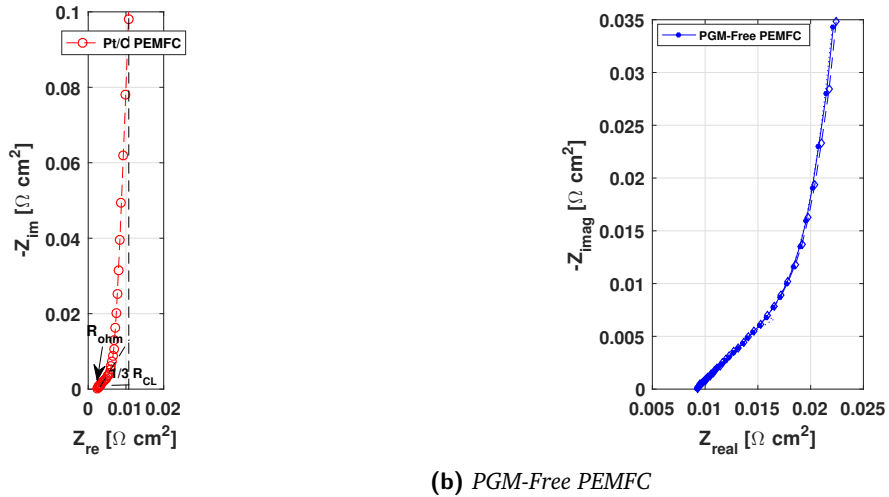
(a) *Pt/C PEMFC*

(b) *PGM-Free PEMFC*

Fig. 2.17.: Examples of *CL* Resistance

increase, exhibiting a characteristic 45° trend (see black dashed line). Once instead the frequency tends to zero, the real part becomes independent from it, while the imaginary part acquires very high values resulting in a vertical line on the *Nyquist* plot. These findings form the basis of the graphical method for the determination of the *CL* resistance wherein the intersection of the high-frequency 45° line with the lower-frequency vertical line, allows the estimation of one third of the searched total *CL* resistance [29]. As evident from the experimental data plotted in *Figure 2.17b*, the actual cell output for *PGM-Free PEMFC* deviates from the ideal 45° and vertical trends. This is probably due to a contingency of factors including RH, *CCL* preparation method and level of ionomer impregnation in the electrode [29]. This type of test has been therefore carried out under different working conditions (specified in *Appendix C*), in order to qualitatively understand their effect.

One-Dimensional Model of PEMFC

3

This chapter is intended to provide for a schematic description of the mathematical model developed in *Matlab*® for the present thesis proposal, including the corresponding assumptions and governing equations. Following, a sensitivity analysis is carried out, in order to understand the relative importance of each amendable parameter. The change of one variable at a time allows to evaluate its contribution to the shape of both polarization and electrochemical impedance spectroscopy curves. This preliminary activity is essential to be able to calibrate the model output curves so to fit the experimental ones and interpret the physical behavior within the *MEA*. The application of a physical model to this mainly experimental work has therefore the purpose of providing for a relevant means of interpretation of the experimental results through fitting.

5

3.1 Model description

The single-phase model used in the current work has been adapted from a 1D physical based *PEMFC* [24] and the previously mentioned (*Section 1.4*) *PGM-Free PEMFC* literature models, together with a derived PhD model [5].

Assumptions   The following assumptions are considered:

1) *CLs*, membrane, *GDLs* are modeled as 1D in the through *MEA* coordinate (*x*).
2) Gas channels are not modeled.
3) Gases and mixtures are considered ideal.
4) The domain is isothermal and pressure drops are neglected.
5) Anode polarization is neglected.
6) Electrolyte membrane is treated as a resistive (ohmic) component.
7) *ORR* obeys Tafel Law and it is first order with oxygen partial pressure [28].
8) Molecular diffusion in the *GDL* is simulated with Stefan-Maxwell's equation.
9) O_2 transport in *CCL* is simulated with Fick's Law.
10) Water transport across the membrane is considered purely diffusive.
11) Inlet flux at the cathode is air.

Steady state operation   The simulation of the polarization curve is carried out under steady state operating conditions, where the local current density is given by the balance of fuel cell losses:

$$V = E_c^0 - E_a^0 - \eta_{OHM} - \eta_{ORR} \tag{3.1}$$

where the activation, ohmic and mass transport losses reduce the maximum reachable generated current.

The Ohm loss in the membrane depends on electrolyte conductivity, thickness and local current density according to:

$$\eta_{OHM} = \frac{\delta_m}{\sigma_m^m} j_0 \tag{3.2}$$

where σ_m is an empirical parameter calibrated on experimental data.

The *GDL* is considered as a pseudo-homogeneous medium where reactants partial pressure profile is to be solved. Reactants conservation in the porous layer in 1D postulates constant fluxes:

$$\frac{\mathrm{d}\phi_i}{\mathrm{d}x} = 0 \Leftrightarrow \phi_i = const \tag{3.3}$$

Molecular diffusion is supposed to be the dominant diffusion mechanism in the *GDL* (*Equation 3.6*), while in the *CL* (*Equation 3.7*) it coexists with Knudsen diffusion.

Binary diffusivity characterizing molecular diffusion is calculated by means of Fuller correlation [14](*Equation 3.4*). Accordingly:

$$D_{ij} = \frac{10^{-3} T^{1.75} \left(\frac{1}{M_i} + \frac{1}{M_j} \right)^{1/2}}{P \left[(\Sigma V_i)^{1/3} + (\Sigma V_j)^{1/3} \right]^2} \tag{3.4}$$

$$D_{kn,i} = \frac{2}{3} r_{kn} \left(\frac{8}{\pi} \frac{RT}{M_i} \right)^{1/2} \cdot \varphi/\tau \tag{3.5}$$

Where M are the molar masses of the diffusing species, T the species temperature, V the diffusion volume (see the values in [14]), the exponents are empirical values derived from experimental data [14], φ/τ the diffusibility parameter accounting for porous and tortuous diffusion paths, and r_{kn} the average radius of the catalytic pore (in the model 50e-9 m).
According to hypothesis 8):

$$\frac{p}{RT} \frac{\mathrm{d}y_i}{\mathrm{d}x} = \sum_{j \neq i} \frac{y_i \phi_j - y_j \phi_i}{D_{ij}(\varphi/\tau)_{GDL}} \tag{3.6}$$

$$\frac{p}{RT} \frac{\mathrm{d}y_i}{\mathrm{d}x} = \sum_{j \neq i} \left(\frac{y_i \phi_j - y_j \phi_i}{D_{ij}(\varphi/\tau)_{CL}} \right) - \frac{\phi_i}{D_{kn,i}} \tag{3.7}$$

where y_i is the molar fraction of the i-th component, related to partial pressure by Dalton's Law: $y_i = p_i/p$. Binary diffusivity D_{ij} is corrected with φ/τ.
Considering the cathode overpotential to have the greatest impact on the local current density, the focus is on their mathematical relationship. Therefore, the *ORR* rate is defined:

$$RR_c = -i_0 \left(\frac{p_{O_2}}{p_{ref}} \right) \exp \left(-\frac{\eta_c}{b} \right) \tag{3.8}$$

where i_0 is the exchange current density, b the tafel slope and η_c the cathode overpotential obtained with the subtraction of the cathode reversible potential from the difference between potentials of the *CCL* solid and ionic phase: $\eta_c = (\varphi_s^c - \varphi_m^c) - E_c^0$. It follows that proton and oxygen conservation across the *CCL* are:

$$\frac{\partial j}{\partial x} = RR_c \tag{3.9}$$

$$\frac{\partial \phi_{O_2}}{\partial x} = \frac{RR_c}{4F} \tag{3.10}$$

To close the cathode catalyst layer system of equations, Ohm's Law is employed to describe both the electronic transport in solid phase (*Equation 3.11*), and the proton transport in ionic phase (*Equation 3.12*):

$$\frac{\partial \varphi_s^c}{\partial x} = -\frac{j}{\sigma_s^c} \tag{3.11}$$

$$\frac{\partial \varphi_m^c}{\partial x} = +\frac{j}{\sigma_m^c} \tag{3.12}$$

The boundary conditions for the cathode catalyst layer problem are expressed as:

$$j = 0 \quad \Leftrightarrow \quad x = \delta_{CL} \tag{3.13}$$

$$p_i = p_{i,GDL} \quad \Leftrightarrow \quad x = \delta_{CL} \tag{3.14}$$

$$\phi_i = 0 \quad \Leftrightarrow \quad x = 0 \tag{3.15}$$

$$j = j_0 \quad \Leftrightarrow \quad x = 0 \tag{3.16}$$

At the *GDL/CL* interface, zero proton current (*Equation 3.13*), and continuity in species concentrations and flows (*Equation 3.14*) are imposed. At the membrane/*CL* interface no fluxes are allowed to cross the membrane (*Equation 3.15*) and the proton current is imposed (*Equation 3.16*), while the electron current is set to zero. A symmetric logic can be applied to the anode, in order to extrapolate the corresponding governing equations and boundary conditions.

Dynamic state operation   *EIS* is a frequency dependent impedance response measurement following the application of a small sinusoidal perturbation. Under the assumption of stabilized periodic regime, each system variable is forced to oscillate around steady state. From the mathematical point of view, the system variables are decomposed in the steady state or *DC* part and the perturbed or *AC* one:

$$X = X^0 + X^1 \exp(i\omega t) \tag{3.17}$$

where the 0 superscript indicates the *DC* property, while the 1 is for the related *AC*. The resulting impedance is a function of current density and operating conditions, due to the non-linearity of the polarization curve. It follows:

$$Z = \frac{V^1}{-j^1} = \frac{-\eta^1_{OHM} - \eta^1_{ORR}}{-j^1} = R_{OHM} + Z_C + Z_A \tag{3.18}$$

The *AC* model requires additional hypotheses:

12) Conservation equations include the unsteady term mathematically described by the time derivative.
13) The non-linear *RR* is linearized around steady state.
14) Result is a linear partial differential equation where the time variable has been eliminated.

The diffusion law is linearized around steady state, and the oscillating oxygen reaction rate, is obtained by linearization of the Tafel Law, and it is first order with respect to oxygen partial pressure [40]:

$$RR^1_c = RR^0_c \left(\frac{y^1_{O_2}}{y^0_{O_2}} + \frac{\eta^1_c}{b} \right) \tag{3.19}$$

CCL problem therefore presents a set of equations in analogy with the *DC* ones:

$$\frac{p}{RT}\frac{\mathrm{d}y_i^1}{\mathrm{d}x} = \sum_{j\neq i}\left(\frac{p_i^1\phi_j^0 + p_i^0\phi_j^1 - p_j^1\phi_i^0 - p_j^0\phi_i^1}{D_{ij}(\varphi/\tau)_{CL}}\right) - \frac{\phi_i^1}{D_{kn,i}} \tag{3.20}$$

$$\frac{\partial j^1}{\partial x} = RR_c^1 - i\omega C_{DL}\eta_c^1 \tag{3.21}$$

$$\frac{\partial \phi_{O_2}^1}{\partial x} = \frac{RR_c^1}{4F} - i\omega\varphi_c\frac{p_c^1}{RT} \tag{3.22}$$

$$\frac{\partial \varphi_s^{c,1}}{\partial x} = -\frac{j}{\sigma_s^c} \tag{3.23}$$

$$\frac{\partial \varphi_m^{c,1}}{\partial x} = +\frac{j}{\sigma_m^c} \tag{3.24}$$

The boundary conditions for the *CCL* problem are expressed as:

$$j^1 = 0 \quad \Leftrightarrow \quad x = \delta_{CL} \tag{3.25}$$

$$p_i^1 = p_{i,GDL}^1 \quad \Leftrightarrow \quad x = \delta_{CL} \tag{3.26}$$

$$\phi_i^1 = 0 \quad \Leftrightarrow \quad x = 0 \tag{3.27}$$

$$\eta_c^1 = 1 \quad \Leftrightarrow \quad x = 0 \tag{3.28}$$

Where the only difference from the *DC* case is represented by *Equation 3.28*: *AC* over-potential at the *GDL/CCL* interface is fixed to 1, because the simulated impedance is independent from the arbitrary reference [24].

To conclude the model description, parameters and property values are reported for completeness in *Table 3.1*.

(a) Physical constants

Name	Unit	Value
F	$C\,mol^{-1}$	96485
R	$J\,mol^{-1}K^{-1}$	8.314
M_{O_2}	$g\,mol^{-1}$	31.999
M_{H_2O}	$g\,mol^{-1}$	18.016
M_{H_2}	$g\,mol^{-1}$	2.016
M_{N_2}	$g\,mol^{-1}$	28.013
V_{O_2}	–	16.3
V_{H_2O}	–	13.1
V_{H_2}	–	6.12
V_{N_2}	–	18.5

(b) Porous media properties

Name	Unit	Value
φ/τ_{CL}	–	0.132
φ/τ_{GDL}	–	0.331

Tab. 3.1.: Fixed parameters of the model

Solution technique   The numerical solution of the model is implemented in *Matlab*®. The script solves the steady state problem and sequentially the transient prob-

lem. The solution is set up as a system of differential equations in the form of $y' = f(x, y)$, and the boundary conditions are expressed on the space interval $[a, b]$ as $g(y(a), y(b)) = 0$, indicating the the phenomena occurring at the various interfaces defined as the the extremes (a and b) of two bordering regions. The integration of the system is performed by `bvp5c` solver.

3.2 Sensitivity analysis of operating parameters

The operating parameters of this physical one-dimensional model have been initialized according to a base case calibrated on the *BoL* experimental data collected for a *1 mg 45%* sample tested before this experimental campaign. These define the restricted set of variable on which the fitting job has been done. In particular, the efforts have focused on the modification of the cathode features, being them the most affecting the *ORR* and, consequently, the overall performance.
In order to proceed in the most efficient way, a preliminary sensitivity analysis of the effect that any variation of a specific value has on both the steady and dynamic state curves has been conducted. This systematic procedure has allowed to understand on which functioning regime a certain parameter impacts, and to quantify the order of magnitude of its change necessary to appreciate a substantial curve alteration.
Below the starting parameters of the base case are summarized:

Parameter	Unit	Value	Definition
i_0	$A\,m^{-3}$	1920	Exchange current density: number of charges produced in unit volume.
σ_s^c	$S\,m^{-1}$	10	Conductivity of the cathodic solid phase: capacity of the carbon phase to transport electrons.
σ_m^c	$S\,m^{-1}$	0.25	Conductivity of the cathodic ionic phase: capacity of ionomer to transport protons.
δ_{CCL}	m	72e-6	*CCL* thickness after being compressed to the 80% of the original value.
C_{DL}	$F\,m^{-3}$	30e6	Double layer capacitance: directly proportional to the electrochemical surface area [11].
σ_m^m	$S\,m^{-1}$	4	Conductivity of the membrane ionic phase: capacity of the membrane to transport protons.

The following plots show both the simulation output (continuous line) and the experimental data of a *1 mg 45% MEA* examined during the current work (dots):
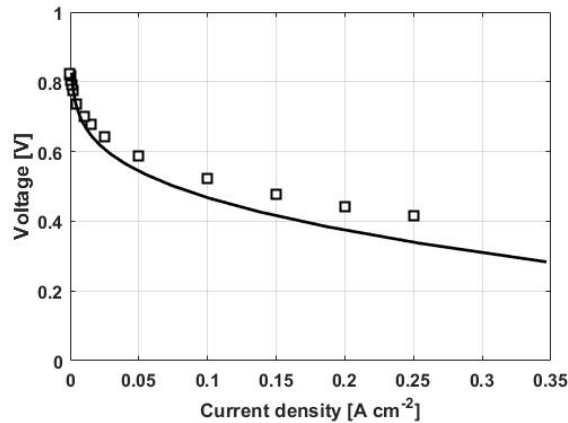
(a) Polarization
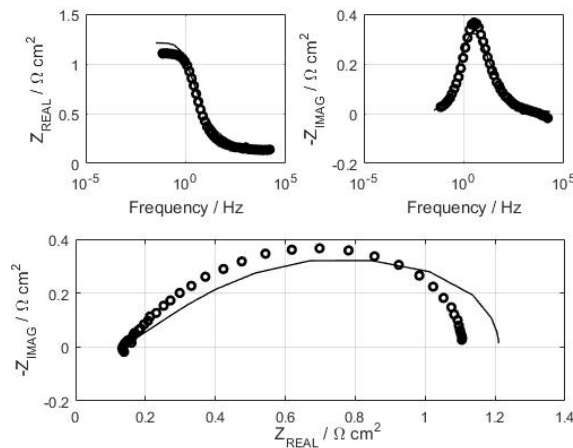
(b) *Bode* (top) and *Nyquist* (bottom) at 0.1 A cm^{-2}

Fig. 3.1.: Model base case

A current density of 0.1 A cm^{-2} has been chosen as reference since it approaches values corresponding to typical operating conditions for a *PEMFC*.

Starting from the base case, the variables have been manipulated by alternatively increasing and decreasing of one order of magnitude each one of them at a time. Results, divided in two different images in order to make them more readable, are presented. The first set of parameters includes the properties that have an influence on only a certain type of operating condition (steady or dynamic state) and the only variable taking into account the effects of the non ideality of the system outside the *CCL*. The second set of parameters include the more sensitive variables governing transport phenomena.

(a) Polarization

(b) *Nyquist* and *Bode* diagrams

1st set of parameters - considerations:

- $i_0 \rightarrow$ Its change causes a parallel shift in the polarization curve upwards or downwards according to the activity regime of the catalyst active sites: high for higher values of i_*. This is thus an indicator of the overall *ORR* efficiency, which is expected to decay over the lifetime. In fact, this parameter takes into account an assigned value of *ECSA* of $100\,m_{Cat}^2 m^{-3}$, and represents the i_0 determining the reaction rate (*Equation 3.8*). A symmetric parameter variation is noticeably reflected in a fairly symmetric curve shift. The parallelism between analyzed

curves means that the local derivatives (Tafel slopes) remain the same, and hence this variable does not give any indication about the *ORR* mechanism. Given the strict relationship between the *EIS* responses and the derivative of the current density around which the oscillations are imposed, i_0 is found not to be affecting the shape of the latter curves.

- $C_{DL} \rightarrow$ This capacitive element is associated with the charge transfer happening during *ORR* at the *CCL*/membrane interface, it models the effect of accumulation of ionic and electronic charges. Due to its intrinsic dynamic nature, the influence on steady state measurements is null. *Bode* plots, on the other hand, show a change in the frequency at which certain phenomena occur: curves are shifted upwards/downwards in the real, and right/left in the imaginary plots. C_{DL} seems generally to act on the characteristic timings at which the different phenomena take place. These effects end up balancing out, resulting in identical *Nyquist*.

- $\sigma_m^m \rightarrow$ Membrane efficiency to proton transfer appears to be already optimized by the base case observing that an increase in conductivity results in a negligible improvement and its decrease produces a drastic loss especially at higher currents, where the regime is ohmically limited. Accordingly, *EIS* curve moves to the right without changing shape, with the ohmic resistance indicated by the intersection with the real axis increasing. This is reflected in a proportional change in the real, and no impact on the imaginary *Bode* plots.

Fig. 3.3.: Sensitivity analysis - 2$^{\text{nd}}$ set of parameters
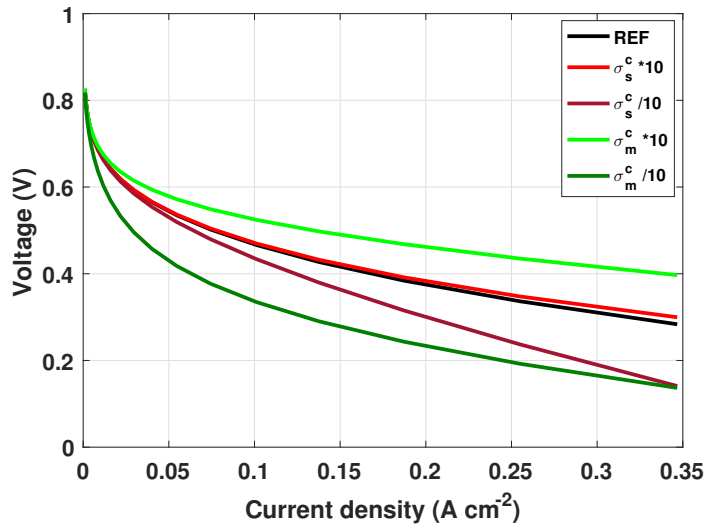
(a) Polarization
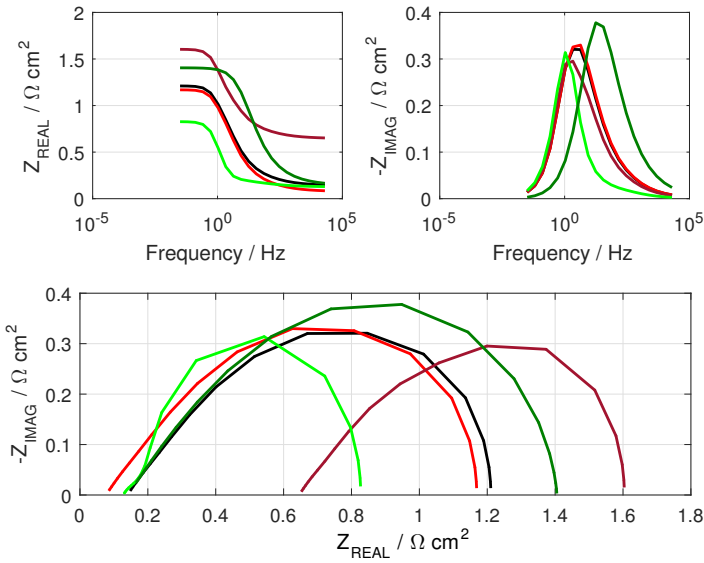
(b) *Nyquist* and *Bode* diagrams

2nd set of parameters - considerations:

- $\sigma_s^c \rightarrow$ The behavior of the polarization curves resembles the same trend as the ones affected by the variation of σ_m^m. The marked performance drop at higher currents is generated by the greater importance that a lower conductivity has on the total overpotential as the number of electrons that are restricted by charge transport limitations in the electrode increases. Reaction is shifted towards the *GDL*. Little influence on the kinetic region results in a *Nyquist* curve having about the same shape and peak value as the reference test, while it is decisively shifted to the right showing the relevance of the electronic conductivity in the high frequency resistance value. This is evident also from the initial values assigned to the electronic and ionic conductivities (10 vs 0.25 S m^{-1} respectively), which stem from the much higher velocity that can be reached by the electrons (much lighter than the protons). Correspondingly, the imaginary *Bode* is negligibly altered, whereas the real diagram mirrors the aforementioned shift.

- $\sigma_m^c \rightarrow$ The greater influence on performances of ionomer conductivity within the *CCL* compared to the same feature within the membrane is evinced by the plots. Asymmetry in the steady state responses to parameter variation is clear: while the improvement is subdued, and more appreciable only at higher currents; the worsening implies a change in the *ORR* mechanism (protons cannot reach the active sites much further from the membrane/*CCL* interface) resulting in a steeper slope in the kinetic region and in a noticeable loss in the rest of the curve. The negligible effect of σ_m^c on the high frequency resistance is highlighted by the *Nyquist* plot, which remains unaltered in the highest frequency area, while the peak moves right and higher or left and

lower according to the considered kinetic conditions. The shape of the curve undergoes a more drastic variation at higher conductivity: it deviates from the initial linear branch denoting a lower ionic resistance across the electrode allowing a more homogeneous *ORR* spatial distribution; and its total cell impedance is substantially lower. This is reflected in a downwards shift of the real, and a narrower imaginary *Bode* diagrams. At lower conductivity instead, the initial part follows the 45° linearity, but finishes with a greater circle height and total impedance.

The sensitivity analysis has been continued by considering the effect that any parameter variation has on the current density profile, in particular on the imposed current of 0.1 A cm^{-2}, the same value analyzed in the *EIS* simulation. The results are plotted in a non dimensional plane, to allow an easier comparison.

The resulting figures show identical ionic current profiles along the anode and the membrane for all the cases, the sensitivity analysis in fact concerns only cathode features.

Fig. 3.3.: Non dimensional current density profile across the *MEA* - 1st set of parameters
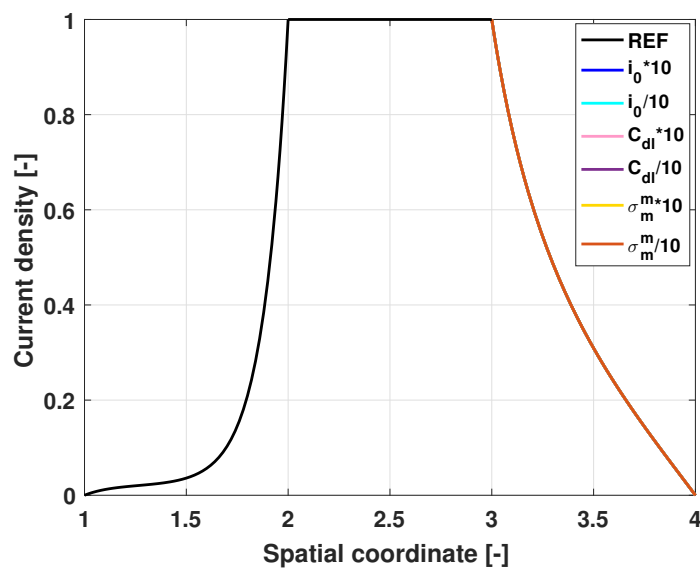
Figure 3.3 clarifies how none of the first set of parameters has an influence on the current profile. i_0 gives thus a quantification of the active area, but not the location of the happening reaction. The membrane conductivity has an effect only on the rate of protons reaching the *CCL*. C_{dl} affects only the transient state, consequently in this steady state simulation no variation is observed.

More significant differences are appreciable by amending the second set of parameters. Ionic phase conductivity appears to be the most affecting. As it decreases,

Fig. 3.4.: Non dimensional current density profile across the *MEA* - 2nd set of parameters
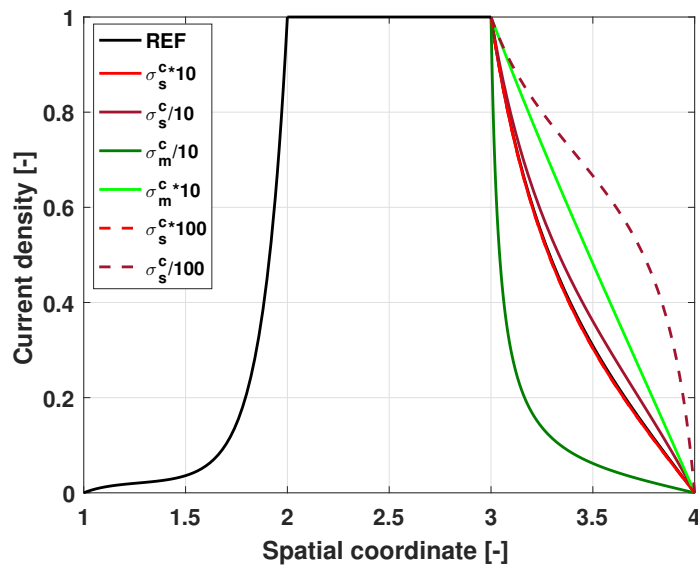
the profile is squeezed towards the membrane/*CCL* interface: *ORR* occurs just in a restricted number of active sites, reducing the overall efficiency. Its increase leads the profile to become linear and to better exploit the whole thickness. Concerning the solid phase conductivity, it has been decided to plot two additional curves showing that, in order to observe a significant variation in the current profile, this parameter has to be changed of one order of magnitude more. As evident, this is valid only for the worsening of the conductivity, where the *ORR* tends to be shifted to the *CCL/GDL* interface, that, as thicknesses grow, is less reachable by the protons. On the other hand, the same rate of variation in the opposite direction, does not distance the curve from the reference case.

Beginning of Life Analysis

<div style="text-align: right; font-size: 3em;">4</div>

The obtained experimental results characterizing the first and most critical operating hours of the fuel cell are intended to be presented and analyzed in this chapter.

An initial description of the adopted procedures, from the set-up of the assembly within the workstation, to the diagnostic ending the test, is made. Repeatability is checked. The effects of different catalyst loading and ionomer quantity is studied starting from the performances reported for the case with the lowest load and Nafion content (*1 mg 35%* series) on the basis of polarizations and electrochemical impedance spectoscopy spectra. Data are fitted by using the aforementioned model, by means of which the influence of each operating variables on a particular change in the shape of the curves has been weighed up. The degradation occurring in the first overnight of operation is evaluated by analyzing the most sensitive magnitudes, such as the current response and the high frequency resistance. The effect of the decay is then established by a subsequent characterization, evincing the nature of the losses.

The chapter terminates with a summary of the observed phenomena, in order to associate the morphology of the cathode to a certain behavior of the overall performances.

4.1 Experimental procedure

A systematic and repeatable set-up/conditioning procedure is essential to yield to comparable results. The same test typology for the first ~20 hours of operation has been adopted for all the samples, in order to assure equal starting conditions for further and longer tests. The timing factor is fundamental for this kind of catalyst layer, in the early life even one hour can make the difference, therefore every step has to be planned adequately to appreciate repeatability.

As seen in *Table 4.1,* the fuel cell has been assembled, warmed up and characterized

Procedure	Duration
Warm up	1 h
0.6 V Holding	10 min
Characterization	1 h
0.6 V Holding	1 h
EIS	20 min
Overnight at 0.6 V	15 h
Characterization	1 h

Tab. 4.1.: *BoL procedure*

by polarization and *EIS* diagnostics as previously explained in *Section 2.3.2.* This has been followed by a period under potentiostatic conditions, fed with fully saturated air at 0.5 bar$_g$, after which the *MEA* has been again subjected to two *EIS* measurements: one carried out at the current of the moment and one at a reference current (generally 0.6 A). Once these preliminary detections have been accomplished, the assembly has been left for the night at 0.6 V and the performance loss has been later quantified by means of a complete characterization (polarization plus *EIS*). From here on, the degradation process of each cell has followed a different pathway according to the specific purpose of investigation of the case.

Hysteresis effect   The evidence upon the rapidity of the decay characterizing *PGM-Free PEMFCs* can be better appreciated by means of the polarizations plotted in *Figure 4.1*, where both the ascending and descending current ramps recorded during the earliest life characterization are shown. The curves are not perfectly overlaid, which indicates that, within the hour needed to carry out the diagnostic, the activity of the *MEA* has been changing. The effect is more conspicuous at the lowest catalyst loading, tending to be absent for the 4 mg samples. However, the relative error results to be negligible even for the worst case (circa 3%), which justifies the choice to represent the final results only with the points acquired in the returning steps (as previously discussed in *Section 2.4.1*).
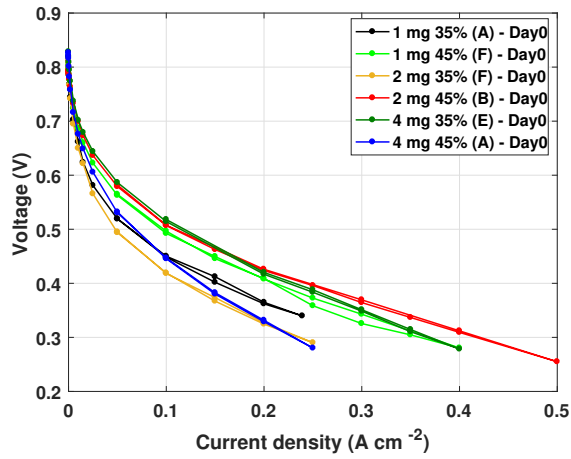
Fig. 4.1.: Hysteresis effect

Repeatability test   The purpose of the current work is an analysis of the factors triggering degradation. Considerations and conclusions can be drawn, on the other hand, only if the samples are comparable. Repeatability tests are thus required to validate the experimental work: in *Figure 4.2* the obtained results are presented.
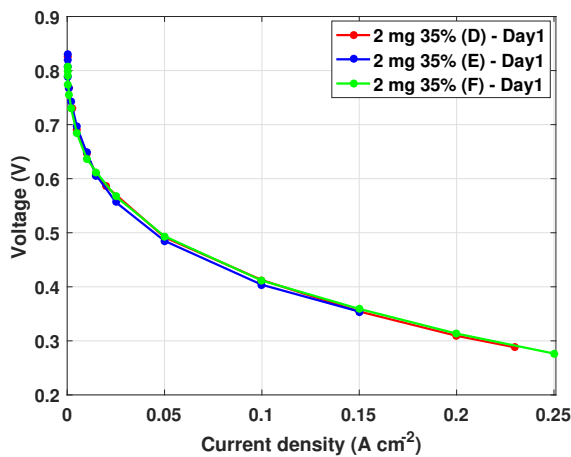
(a) Polarization
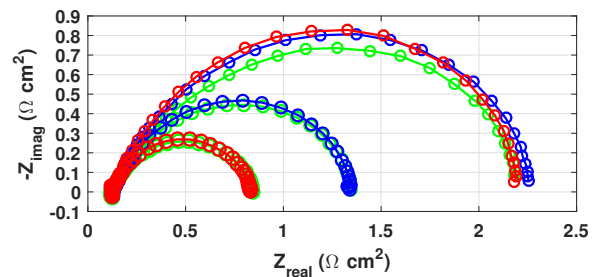
(b) *EIS*

Fig. 4.2.: Repeatability tests

It has been chosen to show the plots of the *2 mg 35%* series since the *2 mg 35% (D)* has been the first tested: outputs have been hence proven to be independent from the workstation. It has to be further noticed that the analyzed data come from the last characterization of the *BoL* procedure, in order to assure the same starting point for the later degradation tests for all the cells.

While the polarizations perfectly overlap, the deviation becomes more tangible in the *EIS* measurements (0.2, 0.1 and 0.05 A cm^{-2}) as the imposed current decreases. The semi-circle happens to have a lower peak for the *2 mg 35% (F)* sample, whereas

both the *HFR* and the total impedance coincide with the other values. This could be attributed to a slightly different humidification, more evident at low currents when less water is produced. Relative difference can be hence considered negligible, and the repeatbility test passed.

4.2 Model calibration

Polarization is the most immediate index of performance and thus it has been presented as first result. Analysis has been completed by studying the impedance spectra. It has been chosen to present only two plots among the four detections (0.2, 0.1, 0.05, 0.015 A cm^{-2}) acquired during the characterization, the two intermediate values: 0.05 A cm^{-2} and 0.1 A cm^{-2}. 0.015 A cm^{-2} has been excluded for the reasons that will later explain in the section, while 0.2 A cm^{-2} is a current density that has not always been reached during the diagnostic at the *End of Life (EoL)*. In fact, the model has been used to characterize the performances recorded during *Day 0* and *Day 7*, in order to give an interpretation about the degradation phenomena on the basis of the variation of the operating (fitted) parameters.

Once the experimental data have been gathered, they have been fitted by the model. The latter action presupposes some preliminary considerations. The determination of the σ_m^m and σ_s^c parameters has been accomplished starting from the definition of *HFR*. High Frequency Resistance is a function of the conductive features and of the thickness of the electrode, while also considering a comprehensive system resistance (membrane plus contact resistances occuring at the interface of the different cell components) [15]:

$$HFR \propto \frac{\delta_{CCL}}{\sigma_s^c + \sigma_m^c} + R_{sys} \tag{4.1}$$

According to [26], by assuming a much higher electronic conductivity in the *CCL*(compared to the corresponding ionic conductivity), a linear relationship between *HFR* and *CCL* thickness can be established. This approach has been followed by the current model, as underlined by the sensitivity analysis of *Section 3.2*: variation in the intercept with the real axis of the *Nyquist* curve is mainly caused by an alteration of σ_s^c and σ_m^m. From the linear correlation, these two operating parameters can be found. This implies that, in the adopted model, all the contributions to cell resistance apart from the catalyst layer are channeled into σ_m^m. Interpolations are plotted in the shape of $y = mx + q$. The linear coefficients allow to extrapolate:

$$\sigma_s^c = \left(m \left[\frac{\Omega cm^2}{\mu m} \right] \cdot \frac{m^2}{10^4 cm^2} \cdot \frac{10^6 \mu m}{m} \right)^{-1} = \left[\frac{S}{m} \right] \tag{4.2}$$

$$\sigma_m^m = \left(q[\Omega cm^2] \cdot \frac{m^2}{10^4 cm^2} \cdot \frac{10^6 \mu m}{m} \cdot \frac{1}{\delta_m[\mu m]} \right)^{-1} = \left[\frac{S}{m} \right] \tag{4.3}$$

The above calculations have been made separately for the 35% and the 45% Nafion content sets of cells, in order to be able to take into account the proton transport limitations affecting the total cell impedance (as made explicit by the variation of the second intercept with the real axis of the *Nyquist* diagrams - *Section 3.2*) by means of a further fitting of the parameter σ_m^c, even though its contribution to the *HFR* has previously been neglected.

Being the membrane the same for all the samples, the value of σ_m^m is common to all the tests, whereas σ_s^c of the 35% *MEAs* does not match the 45% ones. The obtained values of σ_s^c and σ_m^m are schematized together with the other parameters in *Table 4.3*.

Imperfections in the fitting of the *EIS* curves are caused by the simplifying assumption of constant charge transfer coefficient α set to 0.5, which implies constant Tafel slope b of 0.0609. Effects of changes in the *ORR* mechanism are thus not included in the model outputs, in contrast to practical working conditions. While the shape of the polarization curve can be well approximated by adjusting all the other factors, the height of the peaks in the *Nyquist* and *Bode* plots is limited by the α value, as already mentioned in *Section 2.4.2*. The deviation from experimental data becomes more marked as current decreases, since α is inversely proportional to its value, as emphasized by *Figure 4.3*.

(a) 35%   **(b)** 45%
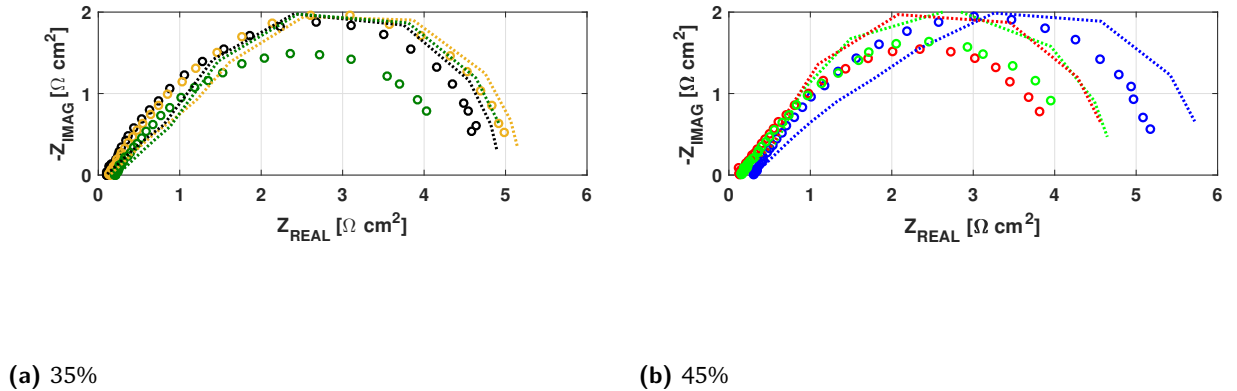
Fig. 4.3.: Day 0 - Modeled (continuous line) and experimental (dots) results at 0.015 A cm^{-2}

The latter observation leads to consider the deviation between modeled and experimental data to be also partially influenced by the eventual presence of a short-circuit current across the membrane: its value would sum up with the current actually imposed by the load and consequently the measured spectra would reflect the response of a higher current, showing hence a lower peak of the semicircle, according to the relation $R_{CT}^{exp} \propto \dfrac{1}{j_{EIS} + j_{SC}}$. On the other hand, the model does not take

into account this phenomenon and considers $R_{CT}^{mod} \propto \dfrac{1}{j_{EIS}}$. The difference between the two relations clearly grows as the imposed current lowers, as confirmed by the behavior of the plots.

Once the meaningfulness of the derived parameters has been checked on the *EIS* curves by verifying a correct intersection with the real axis on the *Nyquist* diagram, polarization curves have been calibrated by amending the values of i_* and σ_s^c. Finally the peaks of the *Bode* plots have been centered with the experimental data through the adjustment of the double layer capacitance.

4.3 Characterization - Day 0

The analysis of the first characterization in *PGM-Free PEMFCs* life has been started with the cell featuring the lowest catalyst loading and the lowest Nafion content, and consequently the lowest thickness - the *1 mg 35% (A)* sample. This choice has allowed to understand the effect that an increase in one morphological feature or another has singularly on the *MEA* performance. The study of the *MEAs*' behavior has been carried on by examining samples with the same Nafion weight percentage (35%), but more catalyst loading (1, 2, 4 mg). Results are shown in *Figure 4.4*.

Going from 1 mg to 2 mg of catalyst loading should theoretically be reflected in a doubling of the catalytic sites and performances. On the other hand, the polarization curve shows that the improvement only belongs to the kinetically controlled regime and is minor (*Figure 4.4a* - yellow dots), while the divergence is made clear as the ohmic region is entered. This behavior has been attributed to the impossibility for the reacting molecules to access the active sites: as previously noticed, humidification takes time to be homogeneous and promote an effective conductive functioning of the Nafion material. The *CCL* then results not to be activated for its entire thickness. Polarization after one hour may thus not take into account the full potentialities of the ionic phase, but at the same time a later test would not be relevant for the *BoL* characterization due to the ongoing compelling degradation.
A mild increase in the *HFR* (the exact values are in *Table 4.2*) can be identified by checking the first intersection of the *EIS* curve with the real axis. Considering the order of magnitude of the fitting values in *Table 4.3*, it is evident how the ionic conductivity in the catalyst layer has a negliglible contribution to the *HFR* compared to the electronic correspondence, in agreement with the aforementioned model [26] and the sensitivity analysis carried out in *Section 3.2*.
σ_s^c and σ_m^m values have been kept fixed along the model calibration (they are thus independent from catalyst loading at identical ionomer content), showing a good fit for the experimental data. This behavior reveals a much greater importance of the
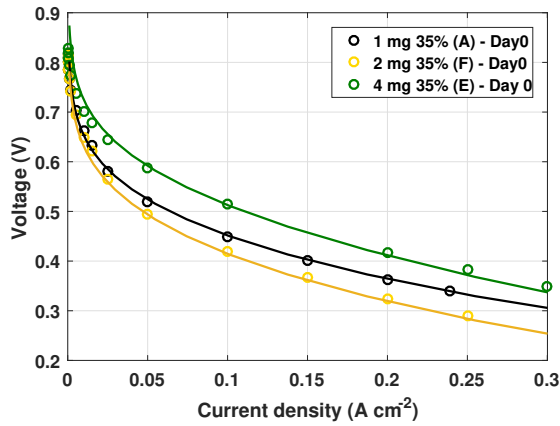
(a) Polarization
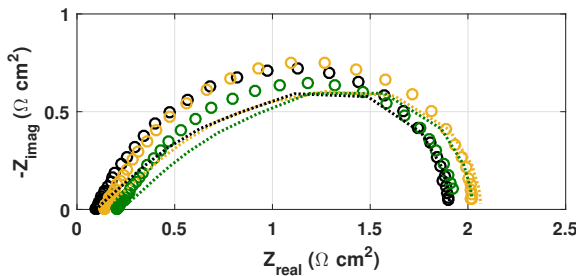
(b) *EIS* at 0.05 A cm^{-2}
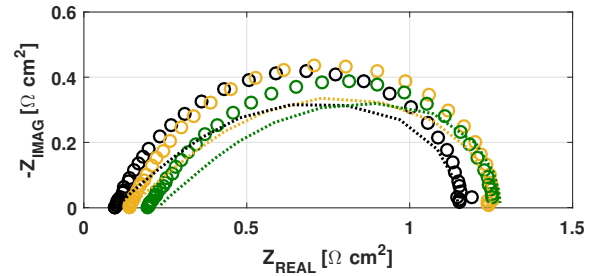
(c) *EIS* at 0.1 A cm^{-2}

Fig. 4.4.: Day 0 - Effect on performances of different catalyst loading (35% Nafion content). Dots are the experimental data, continuous line is the fitted model.

cathode catalyst layer thickness on the definition of the *HFR* magnitude compared to the aforementioned conductivities. The *Nyquist* plot reflects the polarization shape by showing circa overlaid curves in the linear branch, that separate after the peak. The 4 mg curve instead is globally better performing, especially at lower currents, where its important number of active sites is predominant for a successful *ORR*. As current increases, the margin attenuates, which may be due to a transport effect blocking the access to the micropores or hindering the proton and mass transport across the wide thickness of the membrane. In fact the thinnest *MEA* curve appears to have the less steep slope in the considered region. This is reflected in a *Nyquist* circle that progressively broaden as current increases, while the peak remains the lowest showing the most effective kinetic behavior. As already discussed, it is herein made explicit that the main influencing factor of the high frequency resistance is the thickness of the *CCL*, since, keeping fixed both the membrane and catalytic solid phase conductivities, the beginning of the curves has been well fitted only

by updating the δ_{CCL} for each examined sample. Another observation concerns the height of the semi-circle: as previously foreseen, all the model outputs present circa the same value of imaginary impedance: the change in σ_m^c, keeping the other parameters fixed, is not strong enough to alter the circle radius like the sensitivity analysis has shown in *Figure 3.3* while fitting the total impedance. Its value, as shown by *Table 4.2* has a non-intuitive trend, as the highest value corresponds to the 4 mg cell, which tends to have the highest total impedance. This can be attributed to both the simplifying assumptions of the model and to the probable non-homogeneity of the thinner *CCL*, hampering an effective proton transport.

Once the effect of more catalyst at identical Nafion content has been evaluated, the interest has moved to the samples with 45% of ionomer within the *CCL*. Experimental and model results are presented in *Figure 4.5*, and in *Tables 4.2* and *4.3*.

	35%			45%		
	1 mg	2 mg	4 mg	1 mg	2 mg	4 mg
$HFR\,[\Omega\,cm^2]$	0.096	0.145	0.205	0.155	0.135	0.31

Tab. 4.2.: *HFR* values - Day 0

	35%			45%		
	1 mg	2 mg	4 mg	1 mg	2 mg	4 mg
$\delta_{CCL}\,[\mu\,m]$	32	70	132	72	132	261
$i_0\,[A\,m^{-3}]$	2880	960	2304	2304	1536	768
$\sigma_m^m\,[S\,m^{-1}]$	3.54	3.54	3.54	3.54	3.54	3.54
$\sigma_m^c\,[S\,m^{-1}]$	0.125	0.2	0.5	0.31	0.88	0.44
$\sigma_s^c\,[S\,m^{-1}]$	8.33	8.33	8.33	11.16	22	11.16
$C_{DL}\,[F\,m^{-3}]$	40e6	15e6	15e6	20e6	15e6	8e6

Tab. 4.3.: Optimized parameters applied to the model - Day 0

By increasing the ionomer content, the performances gradually improves until the thickness reaches a value that is a probable cause of isolation of significant cathode zones. In fact, more ionomer content leads to a better proton transport and so kinetic activity, but at the same time flooding may be be playing a key role in the losses as the currents increase, since the diffusion of water away from the sites is made difficult. This effect may be quicker for the highest catalyst loading given the higher number of active sites simultaneously producing water. As discussed in *Section 1.3,* too much Nafion could break the electronic pathway: the wider carbon nanotubes further
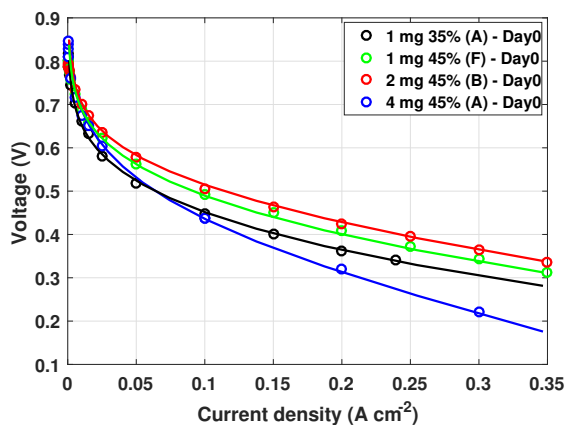
(a) Polarization
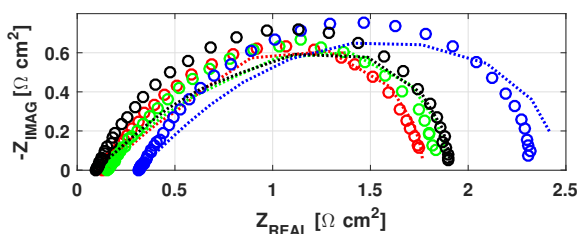
(b) *EIS* at 0.05 A cm^{-2}
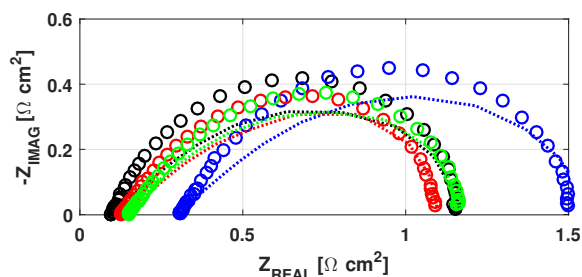
(c) *EIS* at 0.1 A cm^{-2}

Fig. 4.5.: Day 0: Effect on performances at different ionomer content (45% Nafion content - 1, 2, 4 mg$_{Cat}$

branching within the network may be damaged, thus affecting the transport in the thicker electrode more. These behaviors are particularly evident for the 4 mg *MEA*, which starts with the highest *OCV*, but soon presents a steeper slope diverging from the 1 and 2 mg samples, and, from 0.1 A cm^{-2}, also from the *1 mg 35%*. By being the thickest, its *HFR* is averagely the double of the other samples, and the major quantity of ionomer associated with the higher loading ends up in being so counterproductive that the ionic conductivity (supposedly better for the 45%) results lower than the conductivity of the *4 mg 35%* (0.44 versus 0.5 S m^{-1}). In the kinetic regime however, the loss is subdued and hence the experimental height of the semicircle does not differ evidently as the total impedance does. The parameter i_0, linked to the active surface area, shows for both the Nafion contents, a better exploitation of the catalyst surface for the 1 mg *CCL*: active sites are thought to be more spatially concentrated and fully functioning. What is not clear is the performance of the *2 mg 45%*, that, in opposition with the other samples that follow the previous model calibration, show

a much higher fitting value for σ_s^c in order to approximate the curves, especially the *Nyquist* plot, where its higher contribution on the *HFR* value compared to the thickness is emphasized. This is in fact the only case for which a greater thickness does not mean a larger resistance (0.155 $\Omega\,\mathrm{cm}^2$ for the *1 mg 45%* against 0.135 $\Omega\,\mathrm{cm}^2$ for the *2 mg 45%*). It can be attributed to a different level of homogeneity in the electrode structure due to particular preparation treatments. The plots of the current density profiles obtained with the model are presented in *Figures 4.6 and 4.7* in order to complete the interpretation of the elaborated data.
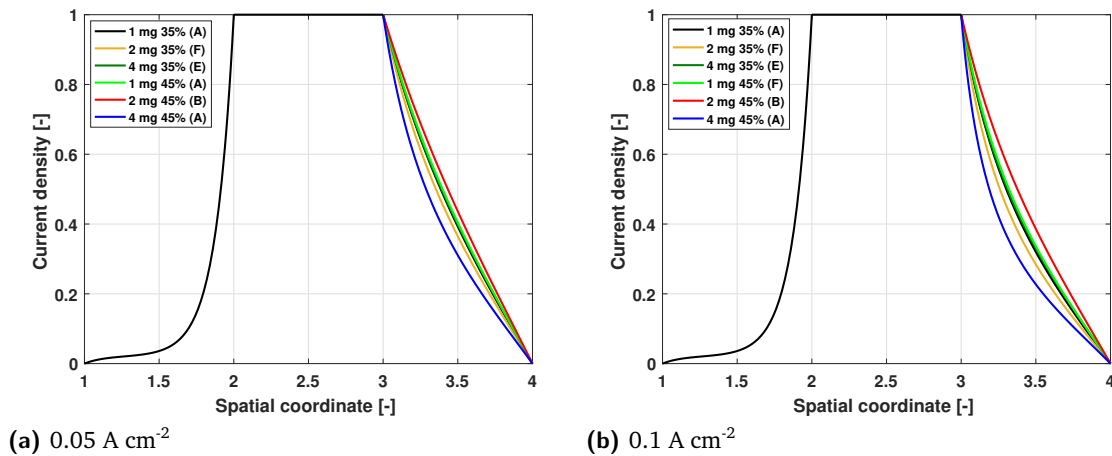
(a) 0.05 A cm^{-2}

(b) 0.1 A cm^{-2}

Fig. 4.6.: Current density profile along the *MEA* at fixed current density

(a) 35%

(b) 45%
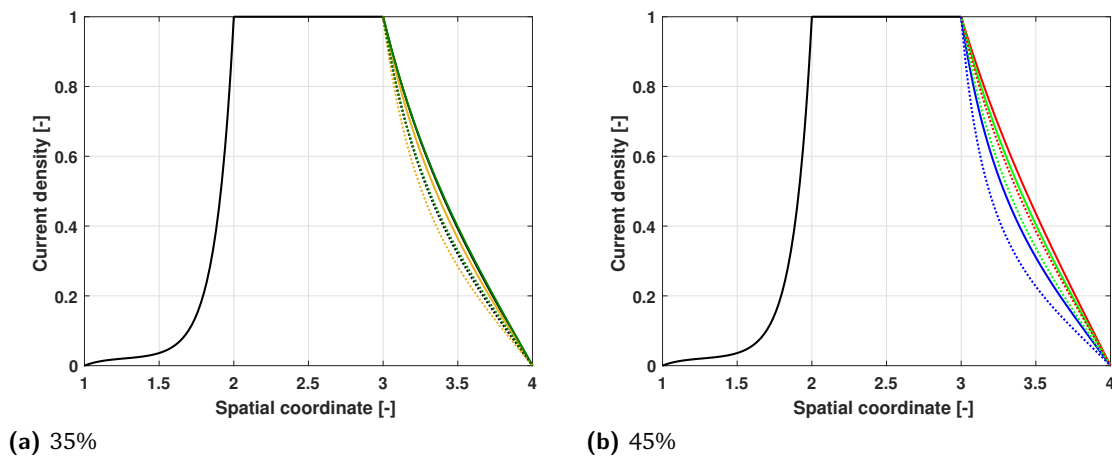
Fig. 4.7.: Current density profile along the *MEA* - dotted line 0.1 a cm^{-2}, continuous line 0.05 a cm^{-2}

The results show that, for each *MEA*, as the imposed current increases, the local current density profile tends to be shifted towards the membrane/*CCL* interface. This is due to the fact that the effect of the most influencing parameter of the current profile σ_m^c (as seen in *Section 3.2*) becomes more important only when ohmically

limited regimes are entered. It is most evident for the *4 mg 45%*, where charge transfer resistance is particularly affected by limitations in ion transport, as seen in the high value of the total impedance in the *Nyquist* curves in *Figure 4.5*. This is confirmed by comparing the *2 and 4 mg 45%* curves and σ_m^c values (0.88 and 0.44 $\mathrm{S\,m^{-1}}$ correspondingly): like expected by the sensitivity analysis, the lowest σ_m^c greatly affects the active domain of the catalyst layer, especially in the ohmic limited region, as evinced by the polarization in *Figure 4.5a*. *1 and 4 mg 35%* present overlaid curves even though the latter *MEA* has a fitted conductivity four times higher. The compensation happens due to its four times thicker electrode, intrinsically hindering the proton transport across the whole *CCL*.

Now that all the types of cathode morphology have been analyzed, a final consideration can be drawn. It results that the best performances have been obtained with the *4 mg 35%* and *2 mg 45%* cells (*Figure 4.8*). They present different catalyst loading and Nafion content, whereas the thickness remains the same. The influence of the thickness is one more time highlighted. *HFR* is determined by the solid phase conductivity, better for the *2 mg 45%*, and the total impedance is penalized by an excess loading inhibiting mass diffusion. More ionomer at medium loading promotes a better ionic conductivity, which allows a better distribution of the *ORR* as seen in *Figure 4.6*. Kinetics is instead more promoted by the *4 mg 35%*, as expected by the higher number of active sites.
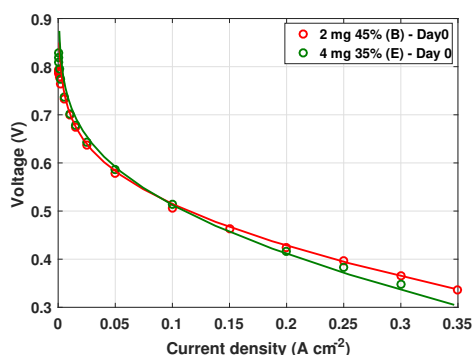
(a) Polarization
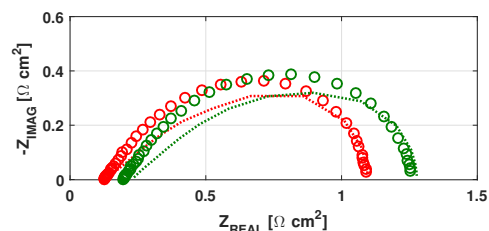
(b) *EIS* at 0.1 A cm^{-2}

Fig. 4.8.: Day 0 - Best results

4.4 Potentiostatic holding

The analysis of the degradation happening in the first overnight starts right after the *EIS* diagnostic done after one hour of holding at 0.6 V and finishes with the characterization of the next day. Below the current and the high frequency resistance

trends are presented (*Figure 4.9 - 4.10*), together with the quantification of the decay rate in [mA h^{-1}] (*Table 4.4*).

(a) 35%   **(b)** 45%
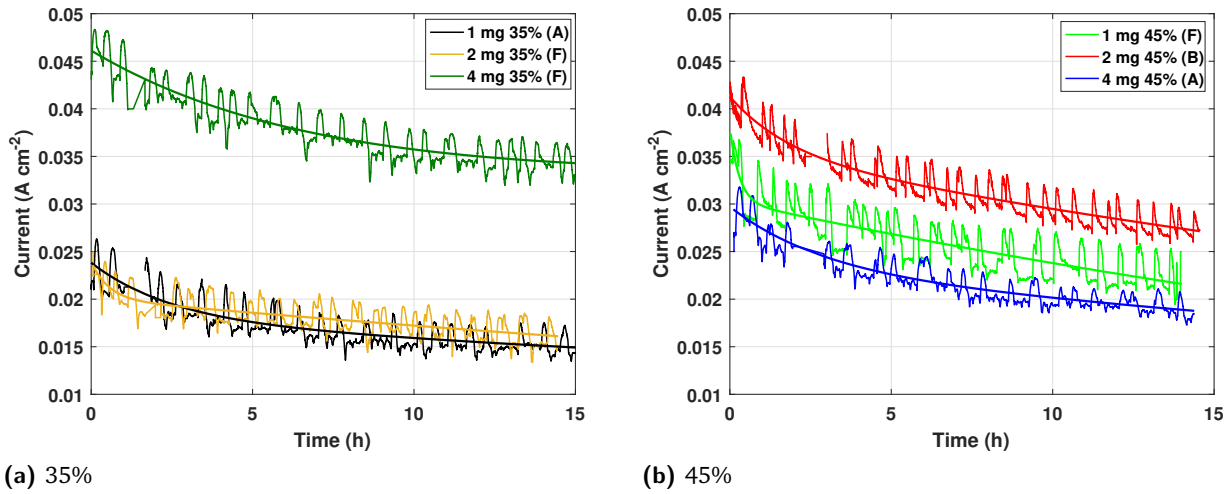
Fig. 4.9.: Overnight at 0.6 V - Current density trend

(a) 35%   **(b)** 45%
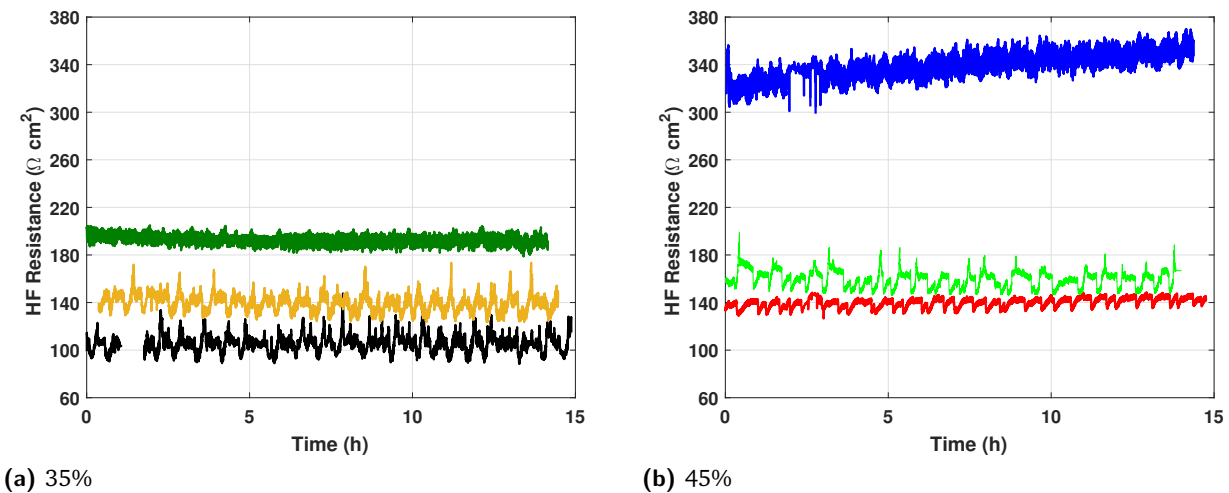
Fig. 4.10.: Overnight at 0.6 V - 1 kHz resistance

Current trends have been fitted using a bi-exponential interpolation in *Matlab*® environment, and have been plotted over the experimental data with a continuous line. These have been later used for the calculation of the degradation rate and the net current loss. The values of the plotted resistance are instead a little different from the values of *HFR* specified in the tables due to the fact that the first are obtained imposing a frequency of 1 kHz, while the latter result from the actual intersection of the impedance spectra with the real axis of the *Nyquist* plot. All the *MEAs* show, as expected, a drastic loss in performances. At the end of the first night the lowest performing is the *1 mg 35%*, despite of the results obtained on *Day 0*. This may be

(a) 35%

	mA h^{-1}	mA
1 mg 35% (A)	12.1	191
2 mg 35% (F)	10.9	158
4 mg 35% (F)	16.1	251

(b) 45%

	mA h^{-1}	mA
1 mg 45% (A)	22.3	334
2 mg 45% (F)	19.6	313
4 mg 45% (F)	15.6	227

Tab. 4.4.: Degradation rate - 1st overnight

$HFR\,[\Omega\,cm^2]$	35%			45%		
	1 mg	2 mg	4 mg	1 mg	2 mg	4 mg
Day 0	0.096	0.145	0.205	0.155	0.135	0.31
Day 1	0.096	0.13	0.18	0.135	0.135	0.34

Tab. 4.5.: *HFR* values (intersection with the real axis in *Nyquist* plot) - Overnight effect

an effect of the smallest ionic conductivity of the *CCL* (0.125 $\mathrm{S\,m^{-1}}$ against the 0.2 $\mathrm{S\,m^{-1}}$ of the *2 mg 35%*) that is made more explicit as the time goes by. In fact the thinnest sample starts from a higher current response, but to be soon decreased to values below the 2 mg, which presents the smallest degradation rate, accordingly to the assumption of initial poor hydration for this *CCL*. The *1 mg 35%* performs even less than the *4 mg 45%*, that has presented a poorer characterization. The thickest *MEA* performs also better than the *2 mg 35%* during the potentiostatic test. This is due to the fact that the operating condition of 0.6 V still belongs to a region where the current output is mainly determined by the kinetics. The same behavior is observed for the *4 mg 35%* against the *2 mg 45%*.

The general trend sees the cells with the most ionomer content to have the highest degradation rate, which may be due to the counterproductive effects of excess Nafion breaking hindering the electron transport. Exception is the *4 mg 45%*, that presents a flatter curve. This can be attributed to the fact that, right from *Day 0*, its operating parameters show both a weak utilization of the active area (lowest value of i_0) and a low σ_m^c in the *CCL* that pushes the reaction to be carried out only close to the membrane. The conclusion is that the initial low performance does not have a wide margin of worsening. This sample represents the exception for the *HFR* trend: while all the other values tend to remain constant or diminish on *Day 1*, supporting the hypothesis of a non-complete hydration of the whole fuel cell assembly, its value grows. The reason for its low current output is thus not a matter of hydration, but rather an intrinsic structural problem. The importance of σ_m^c is well evinced by the trends of current decay for the 1 mg with respect to the 2 mg (symmetry between 35% and 45%): the higher σ_m^c, the wider the catalyst area is exploitable and so the higher the possibility for the *ORR* to take place and generate power. A more noticeable gap between *1 mg and 2 mg 45%* curves may be the result of a better electronic conductivity σ_s^c for the latter (22 versus 11.16 $\mathrm{S\,m^{-1}}$).

4.5 Overnight effect

In this section, the impact that 15 hours holding at 0.6 V have on the performances of the fuel cell is studied by means of the same diagnostic techniques used during *Day 0*. In this case, the model fitting has not been integrated to the experimental data, since its main purpose is to emphasize the change in operating parameters between the beginning and the end of life of the *MEA*. In this analysis, the *EIS* plots that have been chosen to be presented are of the lowest (0.015 A cm^{-2}) and the medium/high (0.1 A cm^{-2}) current density.

In the next characterization the elements of focus are:

- Region resulting more affected by degradation.
- Interception with the real axis in *Nyquist* diagram, supposedly constant for all the *MEAs* but the *4 mg 45%*.
- Evolution in performances of the initial best (*2 mg 45% and 4 mg 35%*).
- Initial low hydration for the *2 mg 35%* cell as cause of its low performances.

(a) 35%   **(b)** 45%
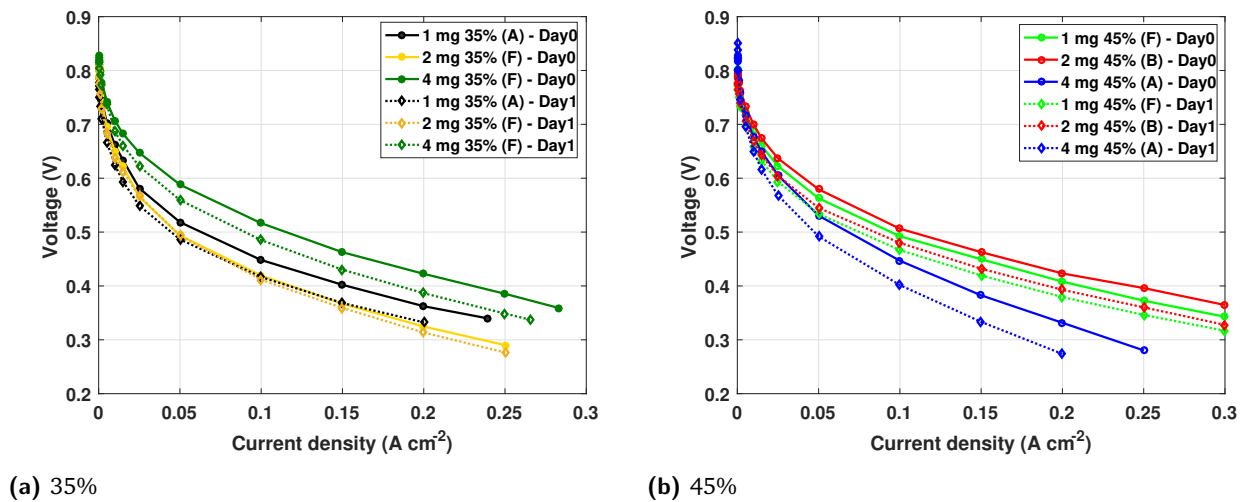
Fig. 4.11.: Day 1 - Polarization

The greatest effect of the period spent in air is suffered by the *4 mg 45%*: it has registered the globally worst performance, increasing losses with increasing current densities, whereas the other *MEAs* show the same degradation rate from the lowest to the highest values (*Table 4.6*), as if they have undergone a downwards parallel shift. This would be the result of a reduction of active domain but no (or minor) change in catalyst properties, as confirmed by the overlapping of the *EIS* curves at 0.1 A cm^{-2} (ohmically limited region), and the widening at 0.015 A cm^{-2} (kinetically limited region).

Despite this decay, the thickest electrode still has the highest open circuit voltage, which is then rapidly extinguished, as shown by the almost vertical line in *Figure*

(a) OCV

(b) Best performing *MEAs*
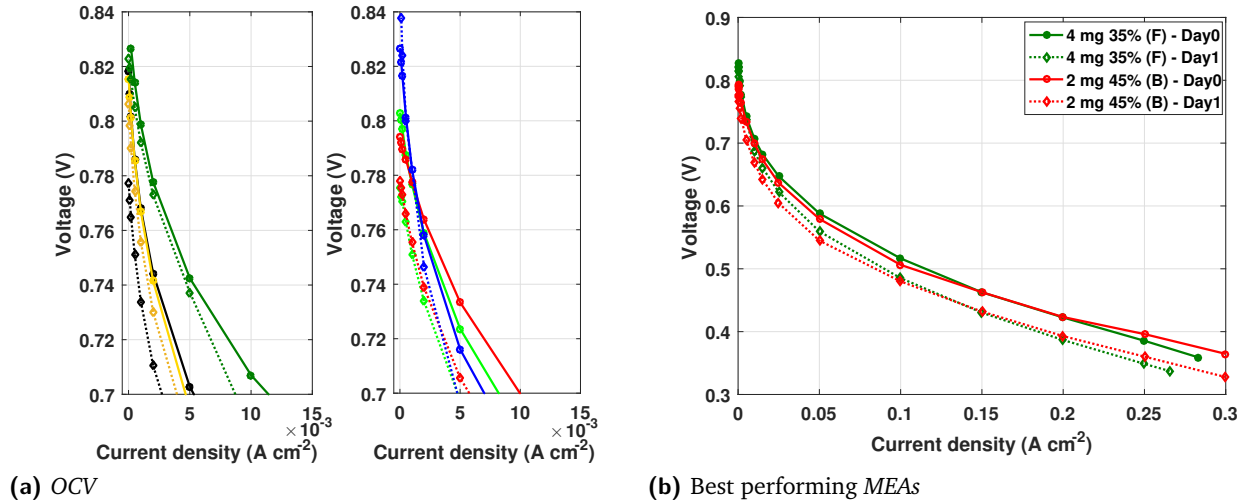
Fig. 4.12.: Day 1 - Polarization

(a) 35%

$[V]$	Day 0		Day 1	
	0.015 A cm^{-2}	0.2 A cm^{-2}	0.015 A cm^{-2}	0.2 A cm^{-2}
1 mg	0.62	0.36	0.59	0.33
2 mg	0.62	0.32	0.61	0.31
4 mg	0.68	0.39	0.66	0.39

(b) 45%

$[V]$	Day 0		Day 1	
	0.015 A cm^{-2}	0.2 A cm^{-2}	0.015 A cm^{-2}	0.2 A cm^{-2}
1 mg	0.66	0.41	0.63	0.38
2 mg	0.67	0.42	0.64	0.39
4 mg	0.65	0.33	0.61	0.27

Tab. 4.6.: Corresponding voltage at low and high currents - overnight effect

4.12a: in this circumscribed region, more catalyst loading still offers advantages, also confirmed by the *OCV* value of the *4 mg 35%*. It is noticeable that, as catalyst loading decreases, the difference in *OCV* between *Day 0* and *Day 1* widens. The *1 mg 35%* is the most affected with 41 mV loss (against the 28 mV of the *1 mg 45%*): both suffer from a little number of active sites, but the thinnest sample, having less ionomer, is probably also subjected to obstructed ionic pathways leading the protons to the micropores. From this zoom, it becomes evident the key role played by the ionic phase within the *CCL* in the kinetic region, by arranging for more interfaces with the active sites: 45% samples all perform better than the corresponding 35%, but the *4 mg 35%* that compensates the less ionomer with the highest loading.

Figure 4.12b reveals the same performance decay for the best performing *MEAs* of *Day 0*, even if the degradation rate of the *2 mg 45%* has resulted slightly more consistent (19.6 versus 16.1 mA h^{-1}) and less efficient at the imposed voltage of 0.6
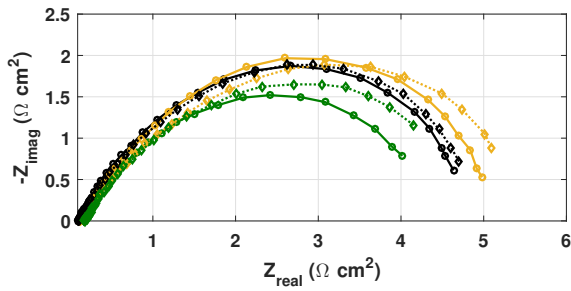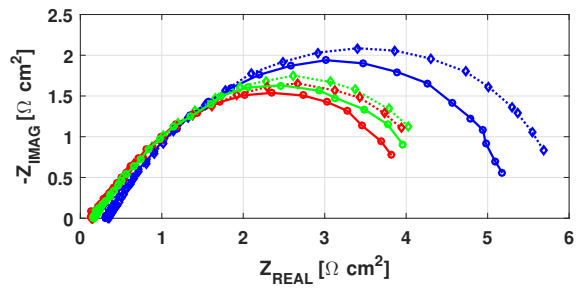
(a) 35%   **(b)** 45%

Fig. 4.13.: Day 1 - *EIS* at 0.015 A cm^{-2}
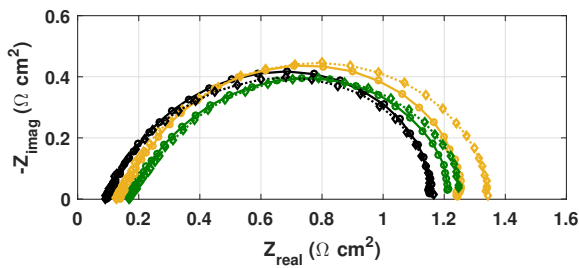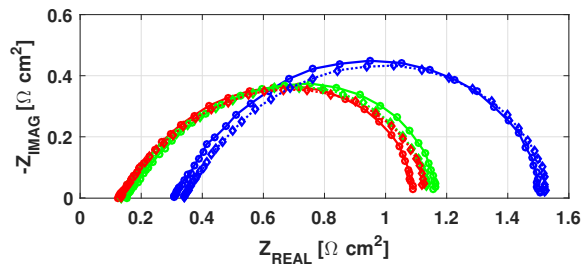
(a) 35%   **(b)** 45%

Fig. 4.14.: Day 1 - *EIS* at 0.1 A cm^{-2}

V (*Figure 4.9*), together with a lower open circuit voltage value (*Figure 4.12a*). On the other hand, a better ionic and electronic conductivity balance out these aspects. As predicted, the *HFR* value presents a change only for the *4 mg 45%* sample. Its substantial losses in the ohmically limited region are reflected in the *Nyquist* plot of *Figure 4.14b*, where the linear branch, as well as the charge transfer resistance, are increased. The worsening in *HFR* may have been caused by a more substantial decrease of electronic conductivity within the thickest electrode. Ohmic losses are evident also for the other 4 mg, that presents a total impedance greater than the less performing *1 mg 35%*. In the 0.015 A cm^{-2} *Nyquist*, both the 4 mg *MEAs* show the most noticeable worsening: the electrochemically active surface area may have been deactivated by poisoning species or may have been impossible to be reached for the protons. Even if these phenomena are thought to be present in any *PGM-Free*

catalyst (*Section 1.3*), transport losses affect more the kinetics of the higher loaded, since they have a more substantial number of sites that can be attacked, causing a change in the current profile and generated power.

The performance of the *2 mg 35%* after the period spent potentiostatically in air confirms the initial hypothesis of slow activation for this particular *CCL*. In fact its polarization curves along time are basically overlaid, ending up, on *Day 1,* in the same operation points of the *1 mg 35%*.

By comparing *Figure 4.13* with *Figure 4.14,* it becomes evident that the functioning regime most affected by the potentiostatic test is the kinetic limited: reduction of the active domain has occurred as some of the phenomena described in *Section 1.3* may have been triggered. This is reflected in a substantial change of the *Nyquist* curves at the lowest current, and no appreciable variation in the 0.1 A cm^{-2} ones. The only exception is the *2 mg 35%*, whose semi-circle has enlarged, that may be due to the previously assumed difference in the activation state of the electrode at the very beginning of life. The *1 mg 35%* instead, has a minor variation even at 0.015 A cm^{-2}, which mirrors the structure of a catalyst layer with a starting number of active sites that can not be reduced significantly.

The similarity between 1 mg and 2 mg curves is common to both the ionomer contents: it is thus necessary to understand if and when differences unveil in order to define the consequences of using 1 mg rather than 2 mg of catalyst loading. Longer test have been accordingly carried out and presented in the next chapters.

(a) 35%   **(b)** 45%
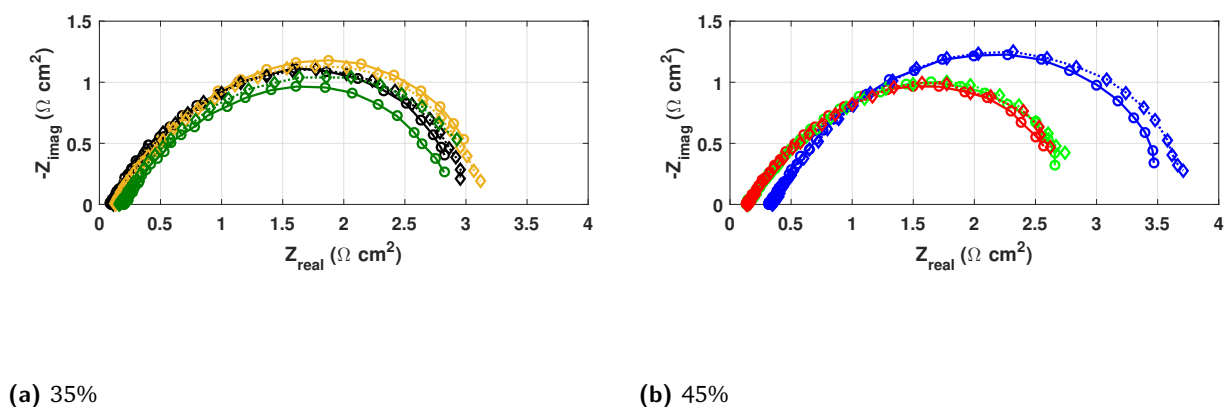
Fig. 4.15.: *EIS* measurement at 0.6 A - Comparison *Day 0* vs *Day 1*

EIS measures at 0.6 A (0.0284 A cm^{-2}) (*Figure 4.15*) in-between tests carried out on *Day 0,* and on *Day 1* confirm that degradation has affected only the lowest currents in the kinetically controlled regime: curves remain basically the same.

Small enlargement of the semi-circle can be observed for the highest catalyst loading cells: as deactivation of active sites is followed by a reduction in their density,

this may contribute in a lowering of protonic conductivity, that is more noticeable in thicker electrodes, where more sites are attacked and isolated, and the ionic pathways are intrinsically longer.

4.6 Conclusion

The beginning of life analysis has allowed to present a panoramic view on the behavior that any type of *MEA* has during its earliest life. Performance trends have been associated to features belonging to specific cathode catalyst layers. A linkage between cell output, catalyst loading and ionomer content has been tried to be established. This represents the basis on which further tests have been carried out. The main conclusions deduced along the analysis are below listed.

* The highest catalyst loading presents the highest *OCV* and best results in kinetically controlled regions, but undergoes a more drastic worsening at higher currents.
* 45% kinetic performances are always better, thanks to more site/proton interfaces.
* An increase in the ionomer content leads to a boost in performances comparable to the results obtained by employing a higher catalyst loading.
* 1 mg of catalyst loading means less active area, as evident by the fitted i_0 value.
* *4 mg 45%* has the most significant ohmic losses (globally poorer performances).
* The thickest electrode pushes the *ORR* towards the membrane/*CCL* interface, lowering the reaction efficiency, as seen in the current profile plots.
* *HFR* is generally function of the thickness of the electrode, as it is the only parameter that has been amended in the model to fit the experimental data (exception *2 mg 45%*).
* The best performing *MEAs* (*2 mg 45%* and *4 mg 35%*) have the same thickness. **Thickness is thus fundamental for the performance, and the corresponding value of these *MEAs* is found to be the optimum in the studied range**.
* Exponential current decay in the first 15 hours is typical of any *CCL*.
* Full activation of the cell is slow due to the significant thicknesses.
* Holding at 0.6 V belongs to the kinetically controlled regime: *4 mg 45%* does not have the lowest current output. Its increase in *HFR* may be due to a lowering in σ_s^c.
* *BoL* degradation may be due to a reduction of active domain, reflected by a parallel downwards shift of the polarization curve and no relevant changes in the *Nyquist* plot at high current. Further investigation is requested.

Parametric Analysis on Stability Tests

<div style="text-align: right">5</div>

Data gathered during the galvanostatic tests characterizing the initial part of the experimental campaign of this work are presented and analyzed in this chapter. Here, voltage decay is identified as a proxy of degradation.

The experimental procedures are at first defined, the functioning conditions have been differentiated among the cells in order to study the effects following the variation of a specific parameter. In particular, the contribution to degradation of a change in the nature of the inlet cathodic flux has been studied.

Operations under air, oxygen and nitrogen have been marked with subsequent characterizations evaluating the ongoing decay.

The effect of the imposition of different currents and backpressures have been evaluated in air; while in oxygen the main concern has been the understanding of the importance of the mass transport resistance on the overall performances. The analysis has been completed by subjecting the cell to an inert environment for a period of time long enough to be able to appreciate eventual alterations in the characterization curves once the cell has been put back to be fed with active reactants.

The experimental results obtained in this preliminary analysis have not been fitted by the physical model, since each *MEA* has been run under non comparable working regimes.

The chapter terminates with a summary of the observed behaviors, in order to associate a certain working condition to a certain degradation phenomena, that may be more or less appreciable on different catalyst layers.

5.1 Experimental procedure

The preliminary analysis carried out in this chapter has started with a *BoL* procedure much similar to the pathway followed previously. The only substantial difference consists in the absence of the *Day 0* characterization, so to study its impact on performances. The interested *MEAs* are the *2 mg 35% (E)* and the *2 mg 45% (F)*: different ionomer contents are compared among the same catalyst loading (intermediate value). The first 15 hours of operation of the *2 mg 35% (E)* and the *2 mg 45% (F)* are then followed by a 55-hours-potentiostatic test in air at 0.6 V, preceded and terminated by a characterization procedure (*Day 1* and *Day 3*), while suspended with a period in nitrogen, as plotted by *Figure 5.1*. A bi-exponential interpolation of the data has been used for the first 15 hours of operation, while the degradation rate of the further segments have been evaluated by means of a linear fit, as described in *Section 2.3.5*.
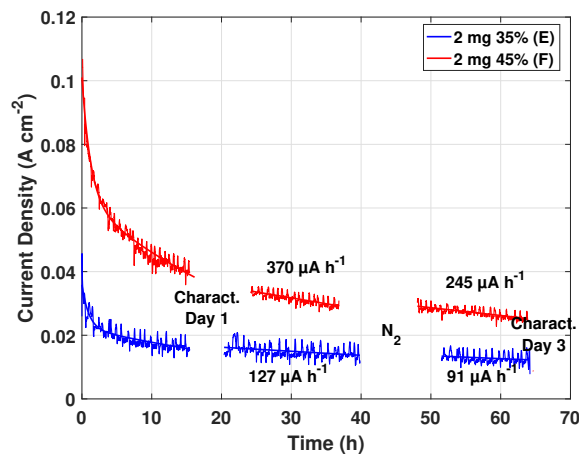
Fig. 5.1.: *BoL* procedure: 70 h potentiostatic holding - *2 mg 35%* vs *2 mg 45%*

The end of the 70 hours period marks the beginning of the galvanostatic procedure. The two *MEAs* has been subjected to the same type of treatments, but in different order and duration.
In *Table 5.1*, the list of the tests that have been carried out is schematized by means of the code defined in *Appendix C*, together with a short indication of their main features.

Polarization and *EIS* (at 0.015, 0.05, 0.1 and 0.2 A cm^{-2} - the latter point possibly not reachable at *EoL*) measurements have been used systematically across the long tests, in order to monitor the performances, understand where the degradation phenomena impact more, and establish a linkage between them and the *CCL* physical properties. The characterization process includes three polarization with the corresponding *EIS*: *CF, CF2, O2* in this order. *CF* is the acronym for constant flow: diagnostics in air

CONT03A	0.3 A - Air
CONT05A	0.5 A - Air
CONT1A	1 A - Air
O205A	0.5 A - O_2
N206V	0.6 V - N_2

(b) Diagnostics

CF	Air
CF2	Air - 2 bar$_g$
O2	O_2 - λ 2
O2N2	O_2+N_2 - CF
O2He	O_2+He - CF

Tab. 5.1.: Preliminary analysis

are carried out with a stoichiometry factor greater than 10 so to assure a negligible variation of reactant concentration along the serpentine. Measures in O_2 are instead executed at a constant stoichiometry, since the reacting molecules are not diluted by nitrogen.

All of the presented experimental procedures do not involve a change in the relative humidity of the inlet flows, which remain fully saturated for the whole test duration. Those have been executed on *Day 1, Day 3* and *Day 7* for both cells. The operations of the *2 mg 35% (E)* have been elongated so to obtain measurements also for *Day 13* and *Day 16*, during which two additional characterizations have been executed in order to evaluate the effect on performances of molecular diffusivity.

The registered data have been considered enough to study the cell behavior; hence, in operando *EIS* measurements have been avoided. The approximate duration for each characterization is 45 minutes, but tends to be shortened as time passes and lower current densities can be reached. Considering the necessity to change the backpressure or the reactant, the total time finally amounts to about three hours. Especially in the first days, where the decay rate is still significant and less stable, a long diagnostic may affect the relevance of the test: a certain degradation behavior may therefore be the result of stresses due to the diagnostic rather than to the test itself. This aspect will be thus investigated later in the chapter.

Figure 5.2 and *Figure 5.3* represent a complete summary of the entire lifetime of the examined cells by plotting the most indicative magnitudes to define their behavior across time. It is worth mentioning that, as seen in *Section 4.4*, *HF Resistance* over time plot does not represent the actual *HFR* identified by the intersection of the impedance spectra with the *Nyquist* real axis, since it is measured at 1 kHz. Its value thus results slightly higher. The elements of interest are later zoomed in further in the chapter, so to provide for a clear view of a particular phenomenon.
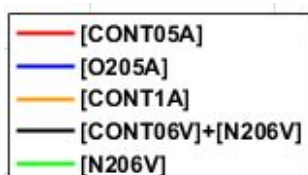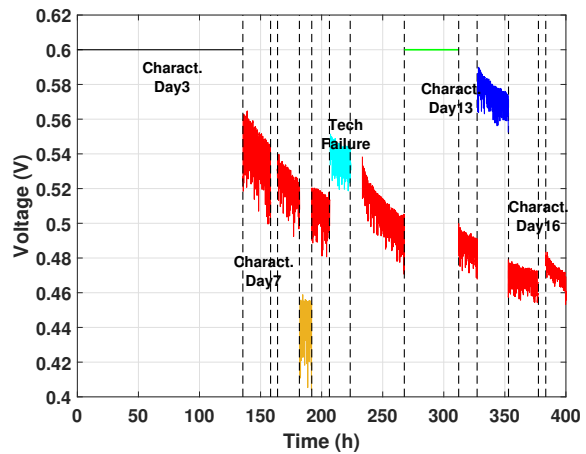
(a) Tests *2 mg 45% (F)*
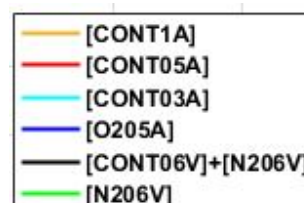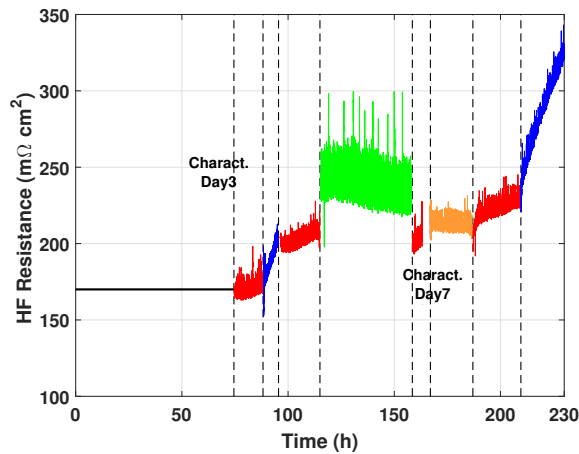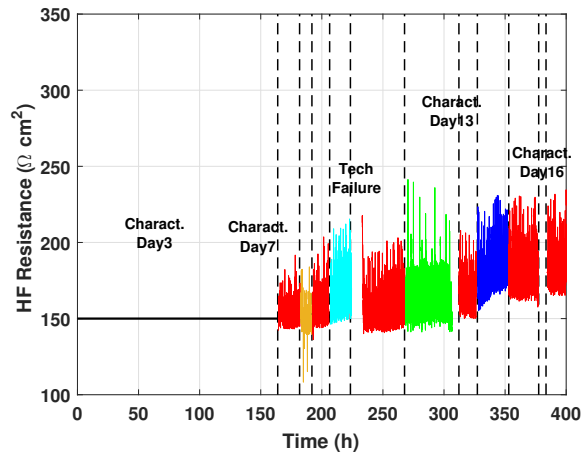
(b) Tests *2 mg 35% (E)*
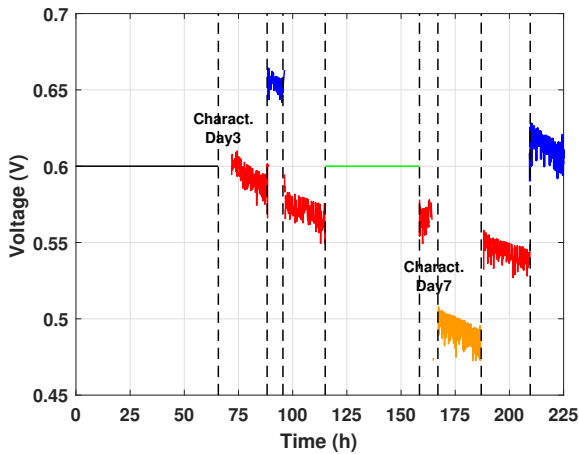
(a) *2 mg 45% (F)*

(b) *2 mg 35% (E)*

Fig. 5.2.: Complete galvanostatic tests - Voltage response

(a) *2 mg 45% (F)*

(b) *2 mg 35% (E)*

Fig. 5.3.: Complete galvanostatic tests - 1 kHz resistance

Table 5.2 schematizes the procedures that each cell has faced after the initial poten-
tiostatic period, specifying, in a chronological order, the type of test, the degradation
rate calculated by means of linear interpolation (according to *Section 2.3.5*), and the
duration.

The results obtained with the first tested cell, the *2 mg 45% (F)*, have turned out to
have an unclear current signal response. The linearly-fitted degradation rate has thus
observed to be better comparable when the holding duration is longer. This is the
reason why the test under a certain current are generally longer for the *2 mg 35% (E)*.

The following sections have been organized in order to analyze the cell response
to different type of tests (potentiostatic or galvanostatic) according to the nature

(a) *2 mg 45% (F)*

Test	μV h^{-1}	Duration
CONT05A	967	11 h
O205A	1117	4 h
CONT05A	648	18 h
N206V	-	50 h
CONT05A	392	4 h
CF+CF2+O2 - Day 7		
CONT1A	756	18 h
CONT05A	567	21 h
O205A	894	24 h

(b) *2 mg 35% (E)*

Test	μV h^{-1}	Duration
CONT05A	786	21 h
CF+CF2+O2 - Day 7		
CONT05A	820	8 h
CONT1A	61	9 h
CONT05A	302	16 h
CONT03A	500	19 h
CONT05A	943	37 h
N206V	-	50 h
CF+CF2+O2 - Day 13		
CONT05A	504	15 h
O205A	597	25 h
CONT05A	259	22 h
CF+CF2+O2 - Day 16		
CONT05A	652	15 h

Tab. 5.2.: Long test details

of the cathodic inlet flow. The study does not concern only the magnitude of the generated power, but also the impact on the aging of the system. The ensemble of the diagnostic results gathered along the samples' lifetime is presented in the last section, so to be able to draw relevant conclusions according to the previous considerations.

5.2 Operation under air

Air is the most viable reactant on a commercial scale, most of the degradation studies have to be thus addressed to the best understanding of the cell response operating with this reactant. In the current analysis, both potentiostatic and galvanostatic procedures have been carried out.

5.2.1 Potentiostatic test

The preliminary analysis has started by evaluating the effect of the characterization carried out on *Day 0* on the cell behavior. Current density and *HFR* responses of the first overnight are shown in *Figure 5.4*, where the *2 mg 35% (F)* and the *2 mg 45% (B)* are the samples previously analyzed in *Chapter 4*. The new *MEAs* have their performances recorded straight after the warming up procedure, having therefore an advantage of about three hours and a half. It is here made clear how even few hours produce a substantial change in the working regime at the *BoL* of this type of *PEMFC*. The cells subjected to the characterization on *Day 0*, that have been previously
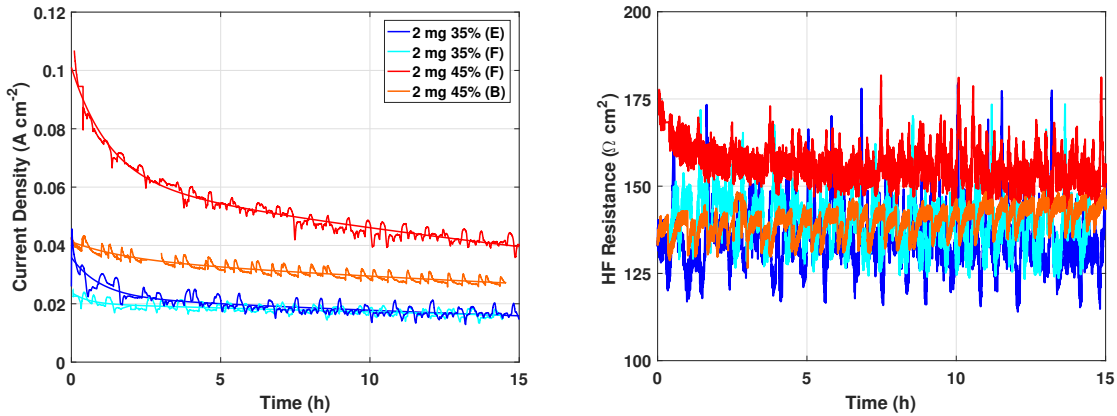
(a) Current density

(b) 1 kHz resistance

Fig. 5.4.: 1st overnight - *Day 0* characterization effect

observed to have an exponential current density decay, appear in turn to have a much flatter curve than the new ones. The distinction is particularly evident for the *2 mg 45%*, that is sill confirmed to be the best performing. On the other hand, the shape difference cancels out once the four hours gap is neglected. In the case of the *2 mg 35%*, an overlapping is verified both for the current density and the resistance responses. The *2 mg 45% (F)* instead, continues to have the faster degradation rate, while generating the highest current (0.04 A cm^{-2} after 15 hours, which is the *2 mg 45% (B)* output of at time 0). *HFR* presents opposite trends for the 45%: whereas one tends to decrease (sample (F)), the other (sample (B)) increases, so to have the same value at the end of the period. As seen in *Figure 5.5*, polarization and *EIS*
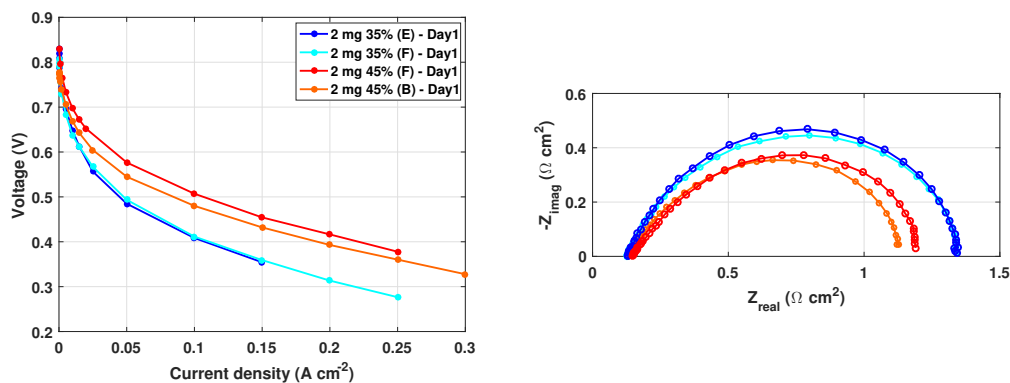
(a) Polarization

(b) *Nyquist* at 0.1 A cm^{-2}

Fig. 5.5.: *Day 1*: *CF* characterization - *Day 0* characterization effect

results mirror this trend: curves of the *2 mg 35%* overlap, while the *2 mg 45% (F)* has instead a better performance, but presenting a slightly higher total impedance. It can be concluded that the deactivation and/or isolation of the *CCL* catalytic sites caused by *Day 0* characterization may be faster than the same phenomena

happening under potentiostatic holding. The current profile of the first case starts in fact from a lower value but continues much flatter, as if the main electronic and ionic pathways have already been hindered by the initial diagnostic. The consequences would be then more appreciable in a catalyst layer with more Nafion content, since intrinsically provided with more ionomer/sites interfaces promoting *ORR* to be damaged. Whereas the 35% curves reunite after few hours, presenting then the same performances on *Day 1*, the *2 mg 45% (B)* still has a poorer utilization reflected in a downwards shift of the polarization plot. The current density trend of the first overnight is characterized, as already discussed, by means of a bi-exponential interpolation. The numerical coefficients of the expression are, on the other hand, hardly comparable. The here considered curves show moreover a much significant activity of the *2 mg 45%* with respect to the *2 mg 35%*. The first has been thus re-scaled on the maximum value of the *2 mg 35%*, according to *Equation 2.5* of *Section 2.3.5*, and plotted in *Figure 5.6*, in order to allow for an easier interpretation. The result indicates a fairly parallel degradation for the first four hours, that then
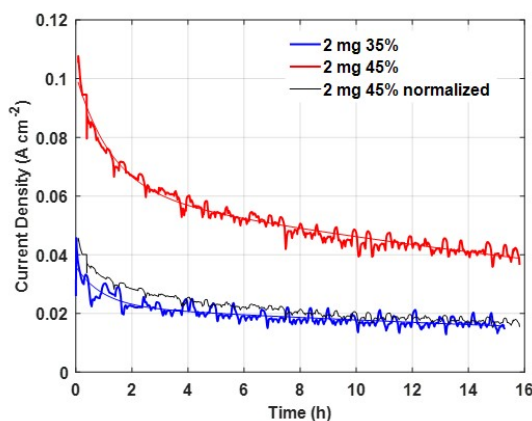
Fig. 5.6.: *2 mg 45%* current density normalization

becomes steeper for the 45%, confirming its higher rate for sites isolation. *Table 5.3* expresses the decay rate on the basis of the extreme points of the fitting (*Figure 5.1*). The potentiostatic test has been decided to be carried out for other ~45 hours,

<div style="display:flex">

(a) 1st overnight

	mA h^{-1}
2 mg 35% (E)	27.5
2 mg 45% (F)	80.4
2 mg 45% (F) norm	29.6

(b) $Day1 \div Day3$

	μA h^{-1}
2 mg 35% (E)	127 - 91
2 mg 45% (F)	370 - 245

</div>

Tab. 5.3.: Degradation rate - Potentiostatic holding at 0.6 V

in order to quantify the attenuation of the exponential trend after the first critical hours. The remaining period under air at 0.6 V results in current responses that can be approximated with linear interpolations (*Figure 5.1*), whose angular coefficients

are indicated in *Table 5.3*. Both the samples have decreasing coefficients in time: degradation has slowed down but not stopped. The *2 mg 45% MEA* continues to go under the most substantial worsening.

5.2.2 Galvanostatic test

This type of test fixes the *ORR* rate by fixing the cell current. The produced water is thus also imposed. Different potentials activate different mechanisms, that may trigger the formation of unwanted species (H_2O_2, *ROS*), that may act on the magnitude of the degradation rate. The purpose of this series of tests is therefore the study and possible interpretation of a particular cell output following a particular imposed current. *Figure 5.7* presents a focus over the cells lifetime during which the current has been changed from the reference value of 0.5 A (red trait): higher (1.058 A, 0.05 A cm^{-2} - yellow line) and lower (0.3174 A - 0.015 A cm^{-2}) values have been imposed. Degradation rates have been calculated by means of a linear fitting (plotted with a black line). Periods under the reference current have been used to

(a) *2 mg 45% (F)*   **(b)** *2 mg 35% (E)*
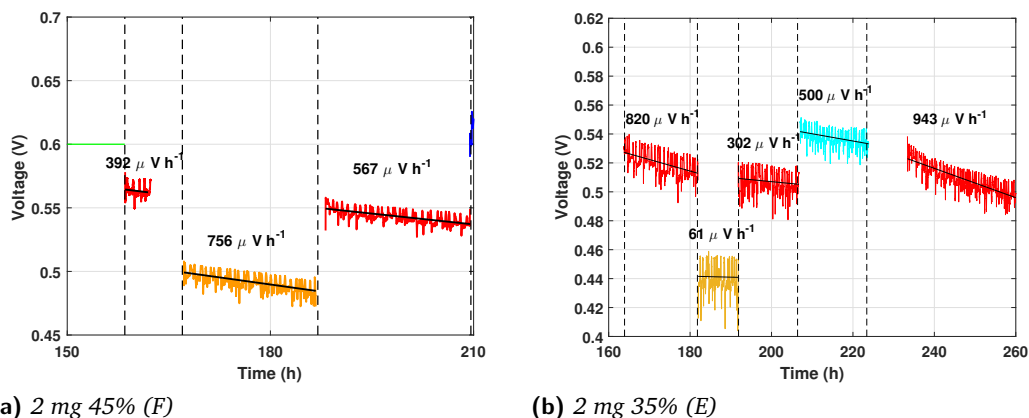
Fig. 5.7.: Galvanostatic tests at different currents - Voltage

give indications about the impact that any change in the working conditions has on the decay rate: a stretch at 0.5 A always precedes and comes after any different test. Length and operating conditions history do not make the tests properly comparable between the *2 mg 35%* and the *2 mg 45%*. On the other hand, the high current test has been carried out circa at the same time, showing a much greater negative impact on the *2 mg 45%*: 756 against 61 $\mu V\ h^{-1}$ - 18 against 9 hours; followed by a steeper degradation of the reference condition compared to the same segment preceding this test. Higher Nafion contents intrinsically exhibit difficulties in diffusing water away from active sites, at high currents the phenomenon may be worsened by additional induced flooding, leading to a higher degradation rate for the *2 mg 45%*. On the other hand, lower Nafion contents appear to be affected more drastically by low currents: ionic phase may suffer from non-optimal hydration and conductivity,

(a) *2 mg 45% (F)*				**(b)** *2 mg 35% (E)*		
Test	μV h^{-1}	**Duration**		**Test**	μV h^{-1}	**Duration**
CONT05A	392	4 h		CONT05A	820	8 h
CONT1A	756	18 h		CONT1A	61	9 h
CONT05A	567	21 h		CONT05A	302	16 h

leading to a greater degradation rate in the following reference section (302 versus 943 μV h^{-1}). It is then noticeable how the periods after the characterization are marked with a much higher decay than the same test before the diagnostic (*Figure 5.2*). Related stresses are thus not negligible. Galvanostatic operations in air have a much different impact on high frequency resistance of the *2 mg 45% MEA* compared to the *2 mg 35%*. As evinced by *Figure 5.8b*, the 35% sample presents fundamentally
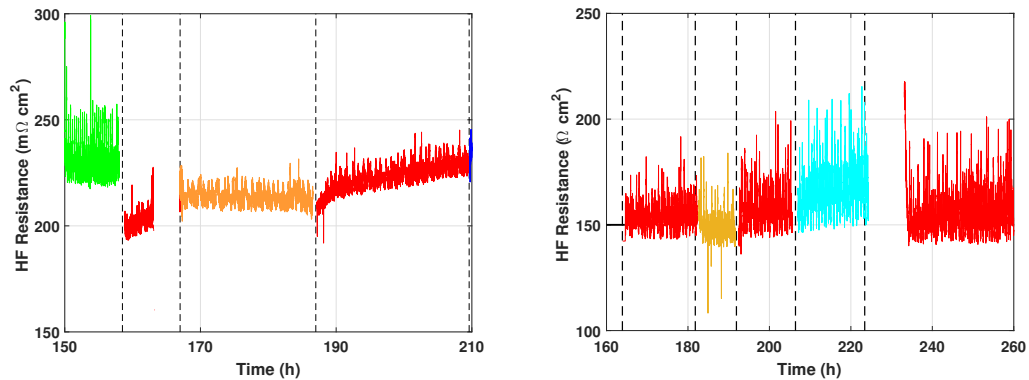
(a) *2 mg 45% (F)*   **(b)** *2 mg 35% (E)*

Fig. 5.8.: Galvanostatic tests at different currents - 1 kHz resistance

constant values for the resistance, particularly for the reference periods, while at varying currents the profile slightly changes (decreasing at 1.058 A and increasing at 0.3174 A). The 45% *MEA* has instead growing values of *HFR* for all the periods, but for the high current stretch where it remains constant (*Figure 5.8a*). It seems then that high current regimes are actually beneficial for the electronic conductivity (defined as the main operating parameter influencing the *HFR* by *Chapter 4*), in contrast to the lower current regimes. The complete picture given by *Figure 5.3* shows a final resistance of the *2 mg 45%* circa doubling the corresponding of the *2 mg 35%*. The latter *MEA* has even undergone a total galvanostatic test of almost double duration.

In conclusion, current effect is still ambiguous: degradation under high current shows opposite trends, the voltage signal presents critical stability, leading to uncertainties about the relevance of a linear fitting; and the impossibility to operate local measurements of the current density within the *CCL* makes the evolution of the active area unknown. In fact, the humidification due to water production strongly

affects the re-distribution of the current in the catalyst layer and this effect could explain the complex behavior observed in different *CCLs*.

5.3 Operation under oxygen

Air accounts for only 20.9% of oxygen, the inlet cathodic flow results thus highly diluted with inerts: the effect of a change in reacting molecules concentration has been here analyzed. Air has been hence substituted with pure O_2 for limited periods of time along the long galvanostatic test. Since the main focus was the investigation of the cell behavior according to the reactant nature, the short tests have been all carried out at the constant reference current of 0.5 A. Pure oxygen turns out to be more aggressive compared to air for both the *MEAs*: voltage decay is faster compared to the preceding and subsequent period in reference air (*Table 5.4*), and the detrimental effect on *HFR* is substantial (*Figure 5.9*).
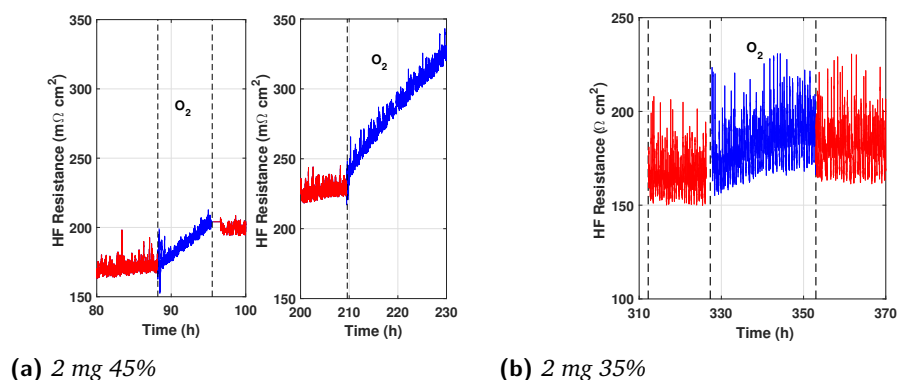
(a) *2 mg 45%*   **(b)** *2 mg 35%*

Fig. 5.9.: O_2 effect on 1 kHz resistance

(a) *2 mg 45% (F)*

Test	$\mu V\,h^{-1}$	Duration
CONT05A	967	11 h
O205A	1117	4 h
CONT05A	648	18 h
CONT05A	567	21 h
O205A	894	24 h

(b) *2 mg 35% (E)*

Test	$\mu V\,h^{-1}$	Duration
CONT05A	504	15 h
O205A	597	25 h
CONT05A	259	22 h

Tab. 5.4.: Degradation rates (linear fitting) - O_2 test

As proposed by the literature [22], this behavior may be the result of a relevant chemical attack from *ROS* originating from Fenton reaction between iron and H_2O_2. On one hand, pure O_2 generates a more effective exploitation of the *CCL* (blue traits in *Figure 5.2*): the reactant has an improved access to the triple phase boundaries that allows a wider utilization of the active surface area, and the different partial pressure of O_2 induces a substantial alteration in the kinetics mechanisms. On the

other, more H_2O_2 intermediate may be produced, and the probability that it would then react with the transition metal to form *ROS* rather than to be further oxidized to water would be higher. *HFR* presents a non recoverable increase. This effect is more noticeable on the *2 mg 45%*, consistently with the previous observations. However, a limited period in oxygen does not influence negatively the degradation of the following period in air at 0.5 A in none of the tested *MEAs*. Indeed its rates (*Table 5.4*) tend to decrease, and the extension of the interpolating line of the first reference segment to the next one shows the voltage trend to continue as if the oxygen interval has not happened, as emphasized by *Figure 5.10*.

(a) *2 mg 45%* **(b)** *2 mg 35%*
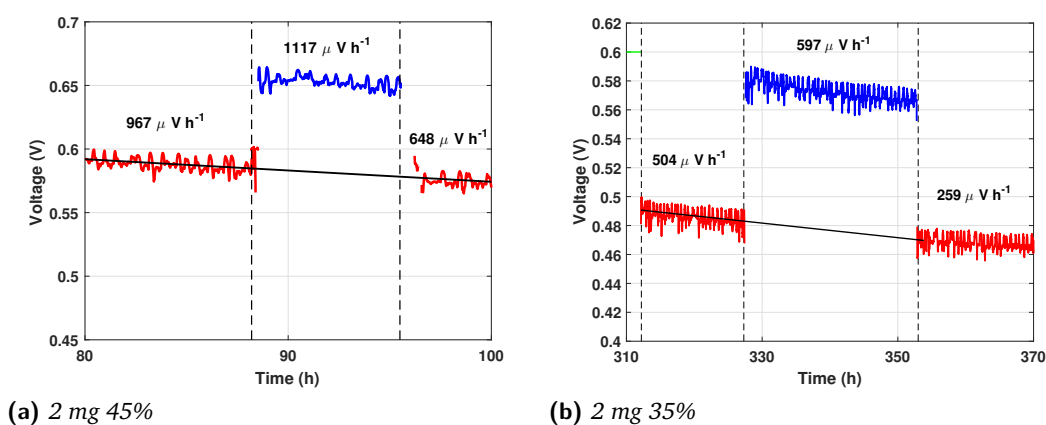
Fig. 5.10.: O_2 effect on voltage response

The apparently non-recoverable effect on the *HFR*, coupled with a negligible impact on performances, leads to conclude that the most impacted by O_2 is σ_s^c, which has a moderate effect on performances and the opposite on *HFR*. The most affected are hence the intrinsic features of the cell, rather than the physical mechanisms. Nevertheless, it is necessary to understand the phenomena taking place under pure O_2 in order to understand if recovery is possible.

5.3.1 O_2 transport resistance

All along the previous chapters, it has been assumed the overpotential due to mass transfer limitations to be negligible. This has been the conclusion coming from the observation of the shape of the polarization and *Nyquist* curves (the latter never presents the second semicircle, characteristic of transport limited regions in traditional Pt/C *PEMFC*), and of the reached currents during the characterization (very low compared to traditional Pt/C *PEMFC*). Oxygen transport resistances inside the *CCL*, remain mostly unclear and include Knudsen diffusion in the gas phase, permeation through the ionomer film, and diffusion to the micropore. One last contribution to this class of resistances is given by the molecular diffusion, which

can be more easily studied by switching balance gas, e.g., nitrogen to helium.

The purpose of this paragraph is thus the evaluation of the relative importance on the total cell impedance of the molecular diffusion resistance.

The test has been carried out only for the *2 mg 35%* on *Day 16*: in addition to the three standard measures, two more procedures have been carried out. Nitrogen and helium have been chosen as switching reactants. The inlet mixture of the two extra characterizations provide for the same O_2 quantity (20.9% - as in air) and the remaining 79.1% either N_2 or He. Given the different molecular diffusivity of N_2 and He in O_2 ($\frac{D_{N_2:O_2}}{D_{He:O_2}} = 2.19$ [32], where D_{ij} is defined in *Equation 3.4*), it is expected a different shape in the curves in the case that the molecular diffusion resistance plays a key role in the total cell impedance. Results are plotted in *Figure 5.11*.

(a) Polarization

(b) *Nyquist* at 0.015, 0.05 and 0.1 A cm^{-2}
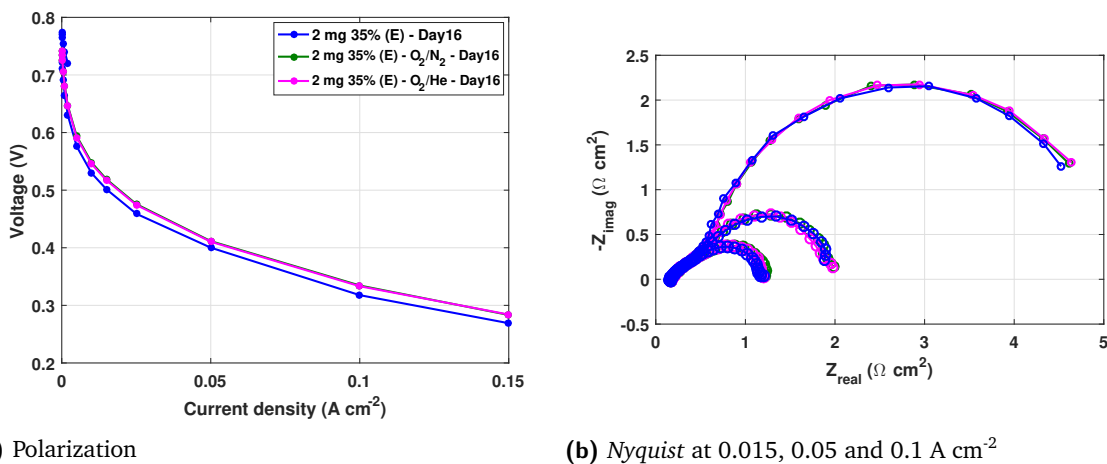
Fig. 5.11.: Molecular diffusivity effect

The polarization and *Nyquist* diagrams clearly prove the non-affection of this mass transfer resistance on the overall performances. The figure presents the results of the diagnostics [CF], [O2N2] and [O2He]: they all overlap. The slightly worse curve of the polarization in air may be due to a little lower O_2 concentration in the inlet flow, compared to the manually regulated mixtures.

5.4 Operation under nitrogen

The previous paragraph has been about maximizing the concentration of reacting molecules, the next object of interest in the cell response to the total elimination of the *ORR*: an inlet flow of inert nitrogen has fed the cell for fairly long time periods, straddling the galvanostatic and potentiostatic tests. The cell has been kept on fixed 0.6 V by means of the potentiostat described in *Appendix C,* producing of course zero current. The effect on the decay can be observed in *Figure 5.12* and *Figure 5.13*.
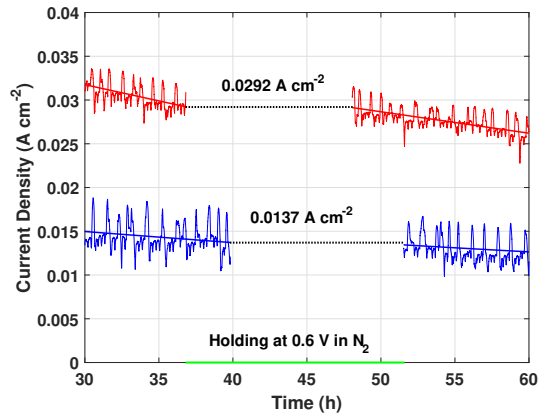
Fig. 5.12.: N_2 effect - potentiostatic test

(a) *2 mg 45% (F)*

(b) *2 mg 35% (E)*
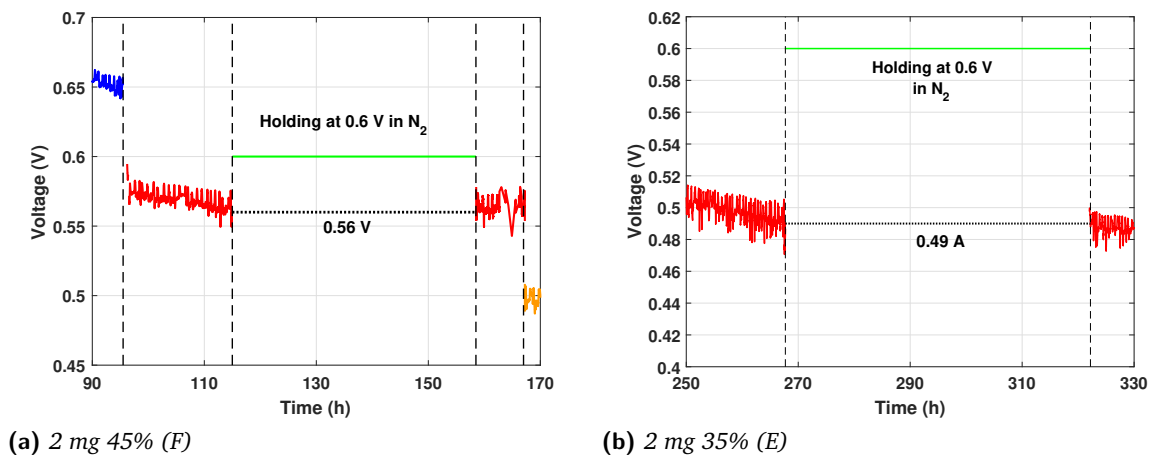
Fig. 5.13.: N_2 effect - galvanostatic test

It is evident that, during the time in nitrogen, the *MEA* does not go through any aging phenomenon: the voltage/current trend after this period restarts from the same value with which the former test has ended, no matter how long the holding in inert is (from ten to fifty hours the result remains the same). Nitrogen feeding results particularly beneficial for the *HFR* of the *2 mg 45%* (*Figure 5.3*): its value tend to decrease. The absence of current generation may hence allow the outflow of the water produced by the previous tests, involved in the flooding of the pores promoted by a higher Nafion content.

5.5 Analysis of the performances

The complete picture of the cells responses to different working conditions allows for a further performances analysis by means of the data collected during the diagnostics across the samples lifetime.

As previously said, the different test history for the two *MEAs* does not make the comparison more manageable. Moreover, it has been evinced the concrete possibility for the formation of hydrogen peroxide, which turns the more immediate 4e⁻ *ORR* into a two step (2x2 or 2+2 e⁻, depending whether the oxidation to water takes place on the same site or on another) reaction, altering the governing mechanisms of the *CCL* [34]. The parameter characterizing the kinetics of the reaction that can be extrapolated from the experimental curves is the the Tafel slope b, strictly interconnected with the charge transfer coefficient α through the linearized expression of the Tafel equation, where the overpotential deriving from kinetic limitations is function of the highest peak of the *Nyquist* curve (charge transfer resistance - R_{CT}) and of the operating current density. *Figure 5.14* is exemplary.
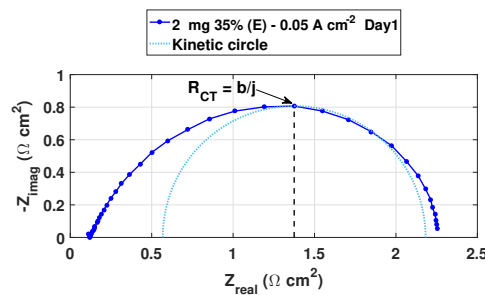
Fig. 5.14.: *Nyquist* - Kinetic circle

The main issue stems from the fact that, as the *ORR* is completed in two steps, each one of them is controlled by a different coefficient, whose distinction can not be discerned within the b value calculated from the experimental data. This of course makes the interpretation of the results even more complex. The drawing of the kinetic circle in *Figure 5.14*, makes explicit the necessity to examine not only the kinetic contribution to the impedance spectra, but also the ionic and electronic transport phenomena. The performances analysis starts with the plots of the polarization results for both cells across the entire lifetime.

As expected, the pure reactant gives the best output. Air at 2 bar$_g$ of backpressure prevails on the 0.5 bar$_g$ test, thanks to its enhancing effect on the fuel cell thermodynamics, increasing the exchange current densities of the reactions, accelerating the electrode kinetics, and improving the mass transfer process. The performance drop of the cells consists generally in a downwards parallel shift, indicating that the main loss stems from a poorer utilization of the active area. All the three diagrams reveal a much stronger impact of the aging process on the *2 mg 45%*. Both cells degrade at a constant rate going from *Day 1* to *Day 7* (*Day 13-16* of the *2 mg 35%* are consistent with the trend); but the thicker *MEA* worsens more substantially. The
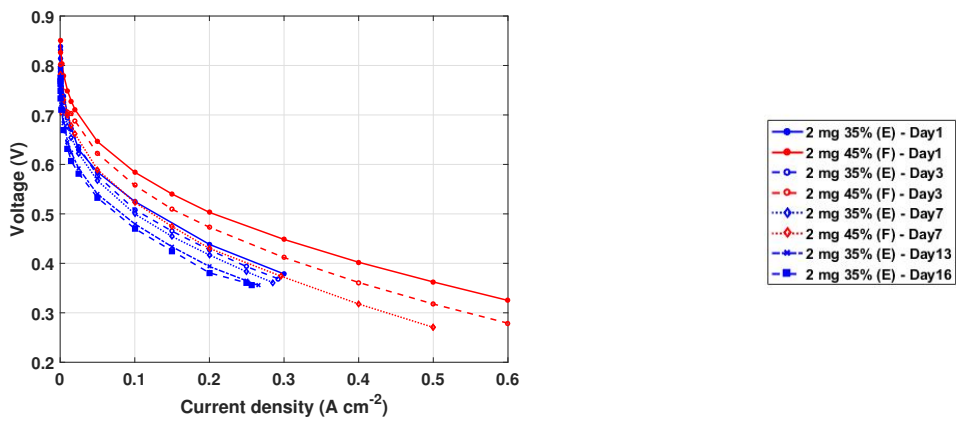
Fig. 5.15.: Polarization - *2 mg 45% (F)* and *2 mg 35% (E)*
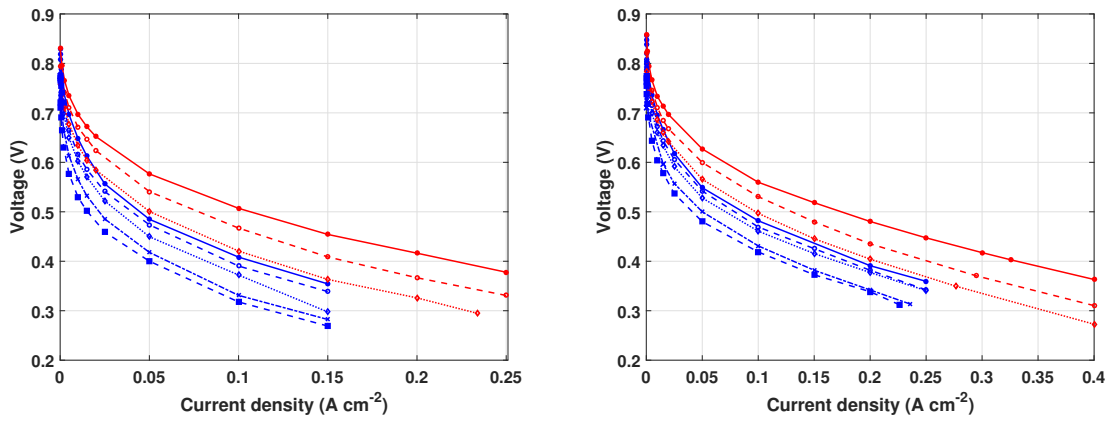
(a) *CF* - Life trend

(b) *CF2* - Life trend

Fig. 5.16.: Polarization - *2 mg 45% (F)* and *2 mg 35% (E)*

(a) O2 - Life trend

(b) Legend

most significant difference in output among time is appreciable in the *[CF]* test, confirming the importance that the favorable features of the other characterizations have towards the *ORR*. This is particularly evident for the *2 mg 35%* that, under O_2, undergoes the least decay (curves overlap at in the kinetic regime and, at highest currents, only 30 mV separates *Day 1* from *Day 7*), showing that the sites may be just hardly reachable rather than deactivated. More ionomer content seems instead to lead to a performance loss that is non-recoverable with a more concentrated inlet flow: electronic pathways to the active sites may have been broken by excess Nafion. The peculiar behavior of the *2 mg 35%*, with performances very similar to each other as time passes, agrees with the previously analyzed *Chapter 4*: further investigation are made in the next chapter. At very small current performance is similar between 35% and 45%, but in this range short-circuit current cannot be disregarded. Tafel plot has been thus used to allow for a clearer view.
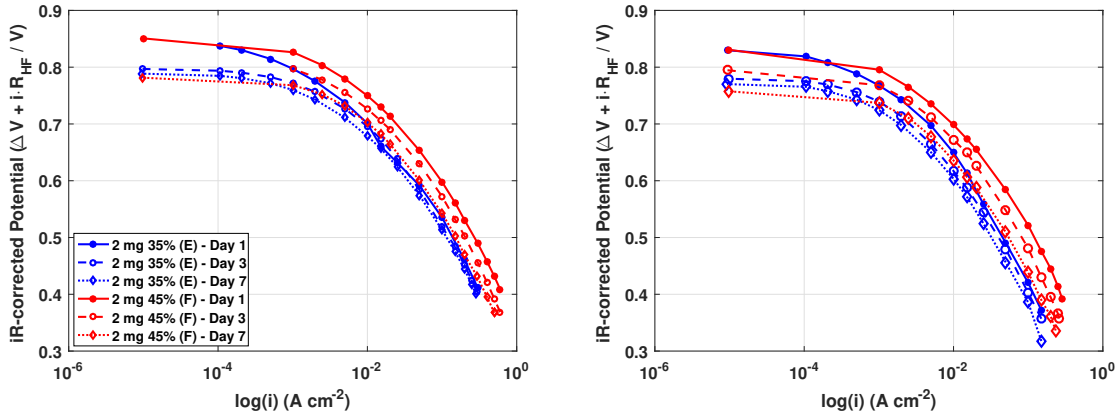
(a) *O2* - Life trend

(b) *CF* - Life trend

Fig. 5.17.: Tafel plot - *2 mg 45% (F)* and *2 mg 35% (E)*

More ionomer provides for more generated power especially under pure oxygen, when the more numerous interfaces can make the difference at the highest potential, whereas below 0.7 V the slopes tend to uniform, suggesting similar governing mechanisms and/or predominant effect of proton transport. *Figure 5.18* underlines the distinctive results recorded for the *2 mg 35% (E)*: while the performances, even if only slightly, decrease, the impedance spectra show a semicircle that counterintuitively tends to lower its charge transfer resistance, total impedance and ionic losses with time.
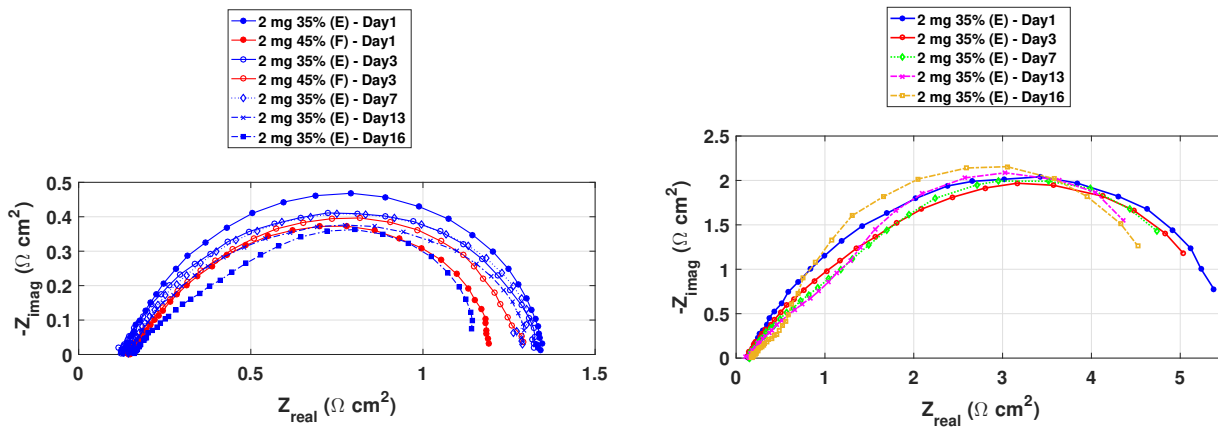
(a) 0.1 A cm^{-2}

(b) 0.015 A cm^{-2} only *2 mg 35% (E)*

Fig. 5.18.: *Nyquist - CF - 2 mg 45% (F)* and *2 mg 35% (E)* - Life trend

This is particularly noticeable at high currents (*Figure 5.18a*). At lower currents (*Figure 5.18b*) the trend does not reverse, but it is less evident, with all the curves (16-days test) basically having the same shape. A peculiar juxtaposition of factors

may have brought to this result. However, it seems that the governing kinetic mechanism of the lowest current regime has not changed for the whole test duration, while the active sites have reduced in number causing the downwards shift of the polarization. On the other hand, at higher current, a non-homogeneous catalyst structure coupled with non investigated phenomena may have acted together to push the ionic conductivity of the *CCL*. *HFR* (intersection with real axis in *Nyquist*) has itself another trend. The parameter improves from *Day 1* to *Day 3*, which may

	Day 1	Day 3	Day 7	Day 13	Day 16
$\mathbf{HFR_{35\%}}$ $[\mathbf{\Omega cm^2}]$	0.13	0.122	0.142	0.146	0.161

be due to a non uniform hydration and slow activation, as previously hypothesized. Then the value of *Day 7* is very similar to *Day 13* and suddenly grows on the last day. Irreversible damages concerning the electronic and/or the membrane conductivities may have taken place in the considered time interval. The following *Nyquist* plots represent the impedance spectra for both the *MEAs* from *Day 1* to *Day 7* for all three diagnostics, evincing with colored arrows the direction of the curves across time. The medium value of 0.05 A cm^{-2} has been chosen since the complete set of measurements is available for this current density. The just observed trend in

Fig. 5.19.: *Nyquist* - 0.05 A cm^{-2} - *2 mg 45% (F)* and *2 mg 35% (E)*

(a) *CF* - Life trend   **(b)** *CF2* - Life trend
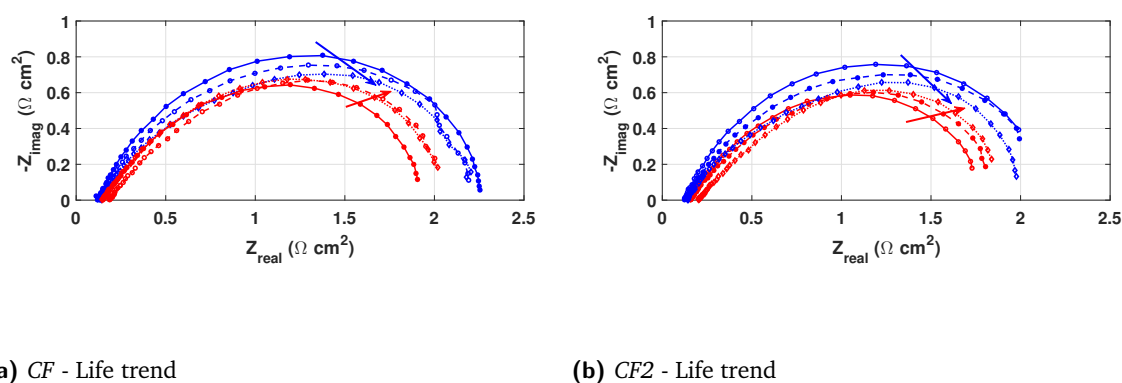
EIS curves shape is confirmed by all the figures. The *2 mg 35%* presents a change in every feature of the curve; the major differences are appreciable in the *[CF2]* diagram that results initially with the same points of the *[CF]*, but lower more. The *2 mg 45%* plots have instead a basically constant linear branch, with a growing charge transfer resistance and total impedance, suggesting very similar kinetic mechanisms. The *HFR* stays constant for the first days and doubles on the last, consistent with the other samples' early life behavior and indicating a deterioration in the solid phase and/or in the membrane with time. The comparison between *[CF]* and *[CF2]* plots leads to notice that the beneficial effect of the backpressure unveils mostly in the second half of the curve, affecting mainly the ionic phase conductivity. *[O2]*, on

**Fig. 5.20.:** *Nyquist - 0.05 A cm^{-2} - 2 mg 45% (F)* and *2 mg 35% (E)*
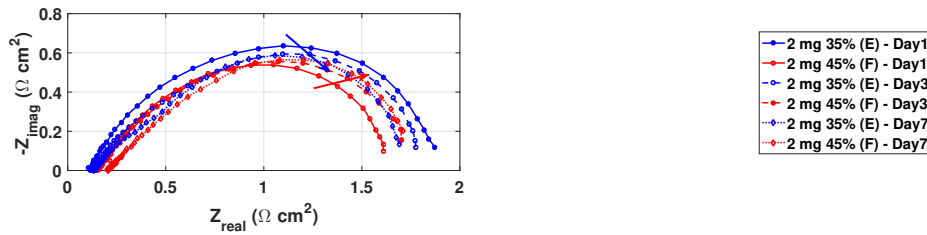
(a) O2 - Life trend

(b) Legend

	Day 1	Day 3	Day 7
HFR$_{45\%}$ [Ωcm^2]	0.145	0.145	0.187

the other hand, tends to iron out the difference in performances across the days and presents substantially lower R_{CT} and total impedance compared to the other tests. This may confirm that the most determinant factor causing spectra variation arises from a poor utilization of the active sites: pure oxygen allows for a better exploitation of the *CCL* and so the curves are much closer to each other. This is verified not only for the same cell output at different times, but globally for both cells spectra. It may mean that in the ionomer-richer *MEA*, sites have been deactivated and/or are permanently unreachable due to excess Nafion. The last step of this preliminary analysis concerns the study of the Tafel slopes as function of current density, giving indication about the reaction mechanisms. The first figure is a

Fig. 5.21.: Tafel slope over current density - *2 mg 45% (F)* and *2 mg 35% (E)*
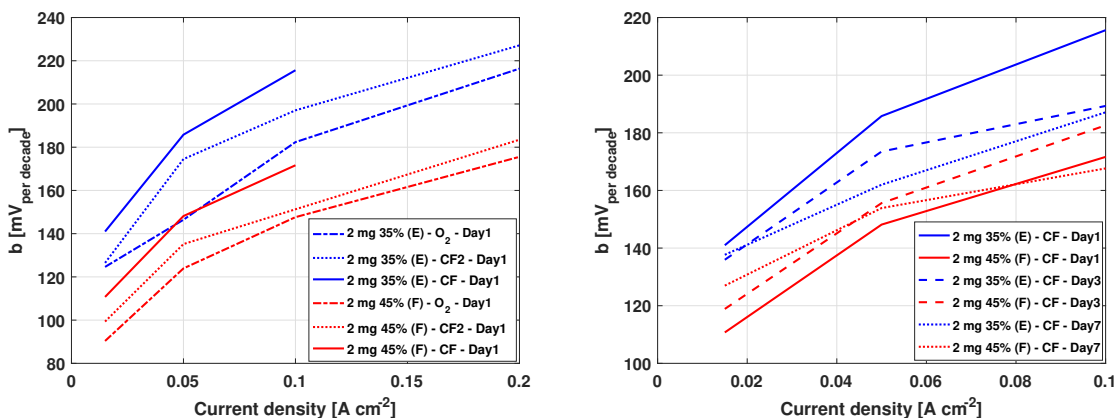
(a) *CF vs CF2 vs O$_2$*

(b) *CF - Life trend*

summary plot clarifying the cells response following a particular test rather than

Fig. 5.22.: Tafel slope over current density - *2 mg 45% (F)* and *2 mg 35% (E)*

(a) *CF2 - Life trend*

(b) *O2 - Life trend*
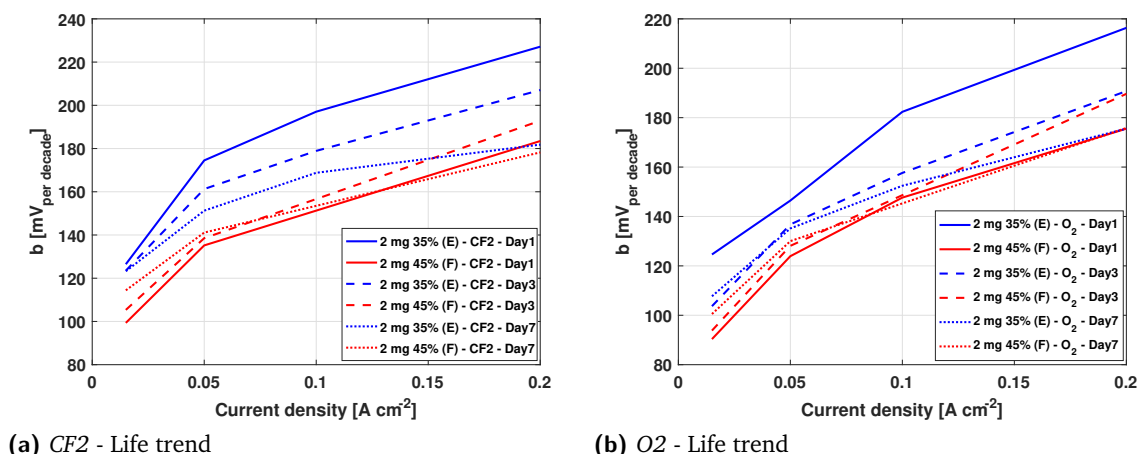
studying the evolution of the parameter with time. The parameter is calculated in when the *EIS* takes place, as previously seen by the definition of b. Generally, at identical current density, the values of the *2 mg 35%* are higher, as a result of a higher kinetic impedance. It follows that *[CF]* values are greater than the *[CF2]* that are greater than *[O2]* in accordance with the effect of partial pressure of O_2 on kinetics. On the basis of *Figure 5.21* and *Figure 5.22*, a smoother change in the Tafel slope among different currents occurs as the *MEA* becomes older (dotted lines). Similar kinetic mechanisms all along life are observed in the *2 mg 45%* at the higher currents, so that the corresponding loss in performances can be almost entirely attributed to ohmic limitations. At 0.015 A cm^{-2} instead, b appears much different across time, supporting the hypothesis of intermediate species formation altering the equilibrium of the *CCL* in the working regime controlled by kinetics. On the contrary, the *2 mg 35%* presents in that operating point the same value of b with aging (except for the test in oxygen), to diverge as currents grow.

5.6 Conclusion

The preliminary analysis has allowed to carry out an investigation ranging over various aspects of the functioning operations of a *PGM-Free PEMFC* during a long period of time. In particular, a linkage between cell output, intrinsic *MEA* features and working conditions has been tried to be established. The variety of executed tests is however followed by the impossibility to make more meaningful comparisons, which is in turn the object of the next chapter.

The main conclusions deduced along the analysis are below listed.

* *Day 0* characterization affects mostly the cells with more Nafion content, due to a strong reduction of the active area caused by the diagnostics.

* Degradation consists mainly in a downwards parallel shift, suggesting the reduction of the electrochemically active area along time. It is most evident for the 45% under *[CF]*. O_2 manages to access more sites: the 35% has in turn similar performances during the lifetime, suggesting the impossibility to reach the site to cause lower voltages in the other diagnostics; while the 45% results suggest a non recoverable deactivation.

* High currents negatively affect the degradation rate of the 45%, suggesting additional flooding, while low currents impact more the 35%, suggesting non-optimal ionomer hydration.

* Voltage signal critical stability makes the current effect ambiguous, and water production strongly affecting the re-distribution of the current in the *CCL* further complicates the analysis.

* Under reference air, *HFR* for the 45% tends to constantly increase, while it remains constant for the 35%.

* **O_2 deteriorates apparently permanently the *HFR*, more intensively for the 45%, while it does not influence the degradation trend of the reference air. Accordingly, the more probable parameter to be affected is σ_s^c, which plays a key role in the definition of *HFR* (*Section 3.2*). Effects on the performances need to be further investigated**.

* **N_2 seems to freeze the degradation process within the cell: current/voltage response restarts from the last value forgoing the period in N_2. *ORR* is confirmed to be the most contributing in the decay process**.

* Molecular diffusion resistance has a non-predominant contribution on the total performance loss, in the range of studied currents.

* The identification of the governing *ORR* mechanisms is complicated by the formation of H_2O_2, as the kinetic pathways can separate into either a 4, a 2+2, or a 2x2 e⁻ reaction [15]. b calculated from R_{CT} is in fact a global parameter.

* Impedance spectra of the 35% tends to improve with time. Next chapter analysis aims at verifying if this is common for other *2 mg 35% MEAs*. Impedance spectra of the 45% present a similar linear branch and charge transfer resistance with time, suggesting similar Tafel slopes; ending up with a greater total impedance (lower σ_m^c).

* Tafel slope trend is opposite between the two samples: at the lowest currents the 45% presents a different value among time, while for the 35% they coincide; at the highest current they get closer for the 45%, while diverging for the 35%. This, coupled with the entity of the changes, leads to the conclusion that similar mechanisms govern the life of the 45%, while a possible non-homogeneous structure of the 35% may lead to the observed behavior.

Degradation Analysis

<div style="text-align: right; font-size: 3em;">6</div>

A standardization of the degradation test procedures is pursued by the experimental work revolving around this chapter. The final objective is the collection of comparable results along the entire lifetime of the cell, in order to be able to better characterize the observed phenomena, by associating them with a certain morphological structure of the cathode catalyst layer rather than with a certain imposed condition.

The experimental steps are initially defined: the test is potentiostatic for the whole duration, current decay is therefore used as proxy of degradation. All the types of *MEAs* are involved in this analysis, that is intended to draw conclusions as general as possible.

Since the samples go through the same working history, the comparison between *BoL* and *EoL* is further interpreted by the mathematical model fitting. The evolution in time of the main operating parameters is hence outlined, in order to understand the deterioration pathway followed by each *CCL*. A linkage between the combination of ionomer content/catalyst loading with particular chemical mechanisms has been tried to be built.

At the conclusion of the potentiostatic test, the analysis continues by subjecting the cells to flows with varying relative humidity, to subsequently study its effect.

The last section of this experimental work has concerned two additional long tests aimed at evaluating the change in performances on the previously discussed potentiostatic holding caused by an alteration of a single operating parameter.

The chapter terminates with a summary of the observed behaviors of the cells, strictly connected to particular degradation phenomena.

6.1 Experimental procedure

The experimental study carried out in this chapter has begun with the *BoL* procedure described in *Chapter 4*. The analysis interests all the types of *MEAs*, in order to provide, at the end of the 160-hour test, the most complete picture.

The potentiostatic holding at 0.6 V follows *Day 1* characterization, and ends with the same diagnostic on *Day 7*. Performances have been avoided to be measured on *Day 3* in order to limit the perturbations in the degradation process. In this regard, only *[CF]* characterizations have been executed, in fact the effects of a change in diagnostic's backpressure/reactant had been already examined in the preliminary analysis. Nevertheless, in operando *EIS* measurements have been exploited every day to monitor the state of the cell. Those have been carried out at the ongoing output current and at the reference value of 0.6 A.

On *Day 7* an extra characterization has been carried out (*[CF2]*). At its end, the cell has started to be fed with inert nitrogen, that, as previously observed, does not affect the decay. *CV, LSV* and *CL* resistance have been then performed: the end of life has been waited for these measures to take place in the thought of limiting the perturbations along the potentiostatic holding.

While still under nitrogen, the cell relative humidity has been lowered to 80%, and, in order to allow for a stabilization of the internal conditions, it has been kept so for a period of about twelve hours. At this point air has been back to be pumped in just for the amount of time necessary to execute the *[RH80]* characterization. *CV, LSV* and *CL* resistance have been then carried out. This proceeding has been repeated for an inlet flow at 60% RH. The cell lifetime is concluded with one last fully saturated *[CF]* aimed at evaluating the effects on degradation of the tests under different *RHs*. A summarizing scheme follows. The details of each test are specified in *Appendix C*.

Procedure	Duration
BoL	20 h
CONT06V	160 h
CF	1 h
CF2	1 h
CV-LSV-CLR	30 min
N206V - RH80	12 h
RH80	1 h
CV-LSV-CLR	30 min
N206V - RH60	12 h
RH60	1 h
CV-LSV-CLR	30 min
N206V - RH100	12 h
CF	1 h

Tab. 6.1.: Degradation analysis

6.2 *BoL* - Summary

A brief summary of the conclusions drawn in *Chapter 4* here precedes the exposition of the results deriving from the complete degradation analysis.

The best performing *MEAs* at the end of the 20-hours *BoL* period are the (*2 mg 45%* and the *4 mg 35%*), which have the same thickness. *BoL* degradation results mostly in a reduction of active domain, reflected by a parallel downwards shift of the polarization curve between *Day 0* and *Day 1,* and no relevant changes in the *Nyquist* plot at high current. The thickest electrode pushes the *ORR* towards the membrane/*CCL* interface, lowering the reaction efficiency, which is made explicit by the current density profile plot across the *CCL*. Excess Nafion hinders electron transport, resulting in greater degradation rates for the 45% *MEAs* during the holding. On the other hand, 45% kinetic performances are always better, thanks to more site/proton interfaces. Lastly, the unusual behavior of the *2 mg 35%* impedance spectra along the lifetime still has to be verified.

Compression effect   All the analyzed *PGM-Free PEMFCs* present the same heterogeneous pattern of different thicknesses across the *CCL*. The relevance of the gasket choice has been thus evaluated before carrying on making further considerations along the cells lifetime. The examined *CCL* has been the *4 mg 45%,* which had presented the most considerable discrepancies in the measurements.

4 mg 45% (A) and *4 mg 45% (B)* performances on *Day 0* have been thus compared, where the first sample has been the least compressed. Gaskets specifics are:

	CCL $[\mu\mathrm{m}]$	**Gasket** $[\mu\mathrm{m}]$	**SubGasket** $[\mu\mathrm{m}]$	$\beta\,[\%]$
4 mg 45% (A)	325	300	125	80
4 mg 45% (B)	325	300	75	71
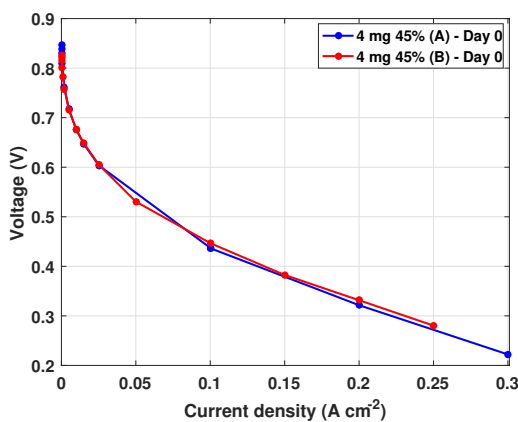
(a) Polarization
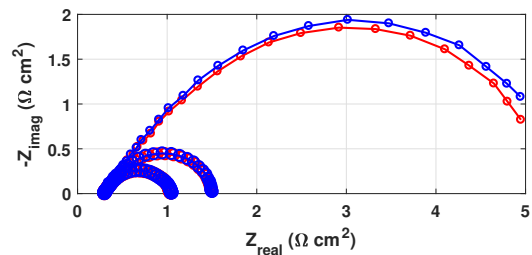
(b) *Nyquist* at 0.2, 0.1, 0.015 A cm^{-2}

Fig. 6.1.: Different *MEA* compression: effect on performances

Figure 6.1 shows the test results, indicating the irrelevant effect that a not negligible (10%) change in compression has on the global performances. It is then justified the preliminary choice of picking the gasket and sub-gasket types according to the average *CCL* measured thickness.

6.3 Results

The next paragraphs are intended to present the results obtained from the long testing procedure. The dissertation begins with the analysis of the degradation under the potentiostatic holding in air, separated from the evaluation of the cells response subjected to inlet flows at varying relative humidities.

6.3.1 160-hours potentiostatic test

The current density and the 1 kHz resistance outputs corresponding to an imposed voltage of 0.6 V are represented in *Figure 6.2*, where all the *MEAs* are plotted in a single diagram.

(a) Current density trend

(b) 1 kHz resistance trend
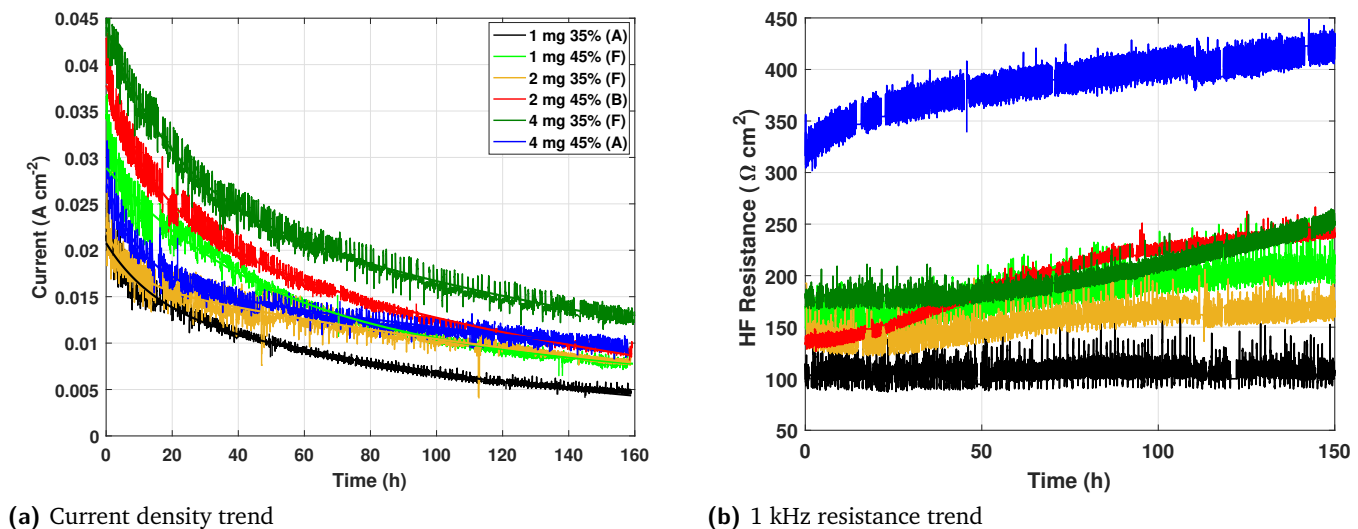
Fig. 6.2.: 160-hours potentiostatic test

Current trends have been interpolated by means of a bi-exponential fitting tool in *Matlab*® environment, and have been graphed over the experimental data with a continuous line. As done in *Chapter 4*, these have been the basis for the degradation rate and net current loss calculations. The values of the plotted resistance result instead a little different from the values of *HFR* specified in the next tables, as previously explained in *Section 4.4*.

(a) 35%

	mA h⁻¹	mA - 20h	mA - 160h	ΔI (20h over 160h)
1 mg 35% (A)	2.2	191	343	56%
2 mg 35% (F)	1.9	158	297	53%
4 mg 35% (F)	4.1	251	663	39%

(b) 45%

	mA h⁻¹	mA - 20 h	mA - 160h	ΔI (20h over 160h)
1 mg 45% (F)	3.7	334	600	56%
2 mg 45% (B)	4.0	313	615	51%
4 mg 45% (A)	2.6	227	420	54%

Tab. 6.2.: Degradation rate - 160-hours potentiostatic holding

As expected, all the samples show a drastic loss in performances, which is though attenuated as the time passes and the critical 20-hours region is exited. This is made more evident by the statistics in *Table 6.2,* whose last column shows that, for all the *MEAs* but the *4 mg 35%*, the decay occurring during the first 20 hours covers more than a half of the whole current loss. The greatest degradation coupled with the smallest relative loss during the first 20 hours of operation is noticeably faced by the best performing samples (*2 mg 45%* and *4 mg 35%*), which possibly start out with the best exploited catalytic surface area, and thus take more time to asymptotically reach their lowest activity.

The peculiar behavior of the *2 mg 35%* continues as it presents the scarcest worsening and a more constant *HFR* value compared to the corresponding *2 mg 45% MEA*. This may be the result of a good balance between catalyst and ionomer content in the *CCL* that assures a correct proton transport and branching of the carbon nanotubes, while not obstructing the micropores and water flow. Diagnostic curves are hence expected not to deviate much across the days.

The observation of the 45% *MEAs* currents reveals an inversion in the trend happening during the lifetime: the 4 mg does start as the weakest, but ends up generating more specific power at the 160th hour. The disadvantage of a thick *CCL* hindering the exploitation of the whole electrode may have been overcome by a high density of both catalytic sites and conductive Nafion in the restricted active part.

The *MEAs* with the smallest loading have a degradation behavior that concentrates the majority of the overall current density loss in the first 20 hours, while keeping the *HFR* stable. In this case, the initial isolation and/or deactivation of the sites affecting all the cells neutralizes the activity of the majority of the catalyst, that stays with circa the same subdued active surface for the remaining lifetime.

HFR diagram emphasizes the dependence of this parameter on the thickness of the catalyst layer: the thinnest samples is the least affected by the aging in contrast with the thickest one; the *2 mg 35%* and the *1 mg 45%* have the same rate of increase, just like the *4 mg 35%* behavior resembles the *2 mg 45%*.

Being the *2 mg 45%* the sample facing the greatest relative increase in *HFR* (+77% against the 20÷40% of all the other samples but the unchanged *1 mg 35%*), it is expected to observe for it the major changes in the *CCL* electronic conductivity, that, as studied in *Chapter 3*, is the more influencing operating parameter in the definition of the *HFR*.

The results of the diagnostics carried out on *Day 7*, fitted with the aforementioned mathematical model, are below exposed, followed by a summarizing table of the numerical operating parameters used in the model.
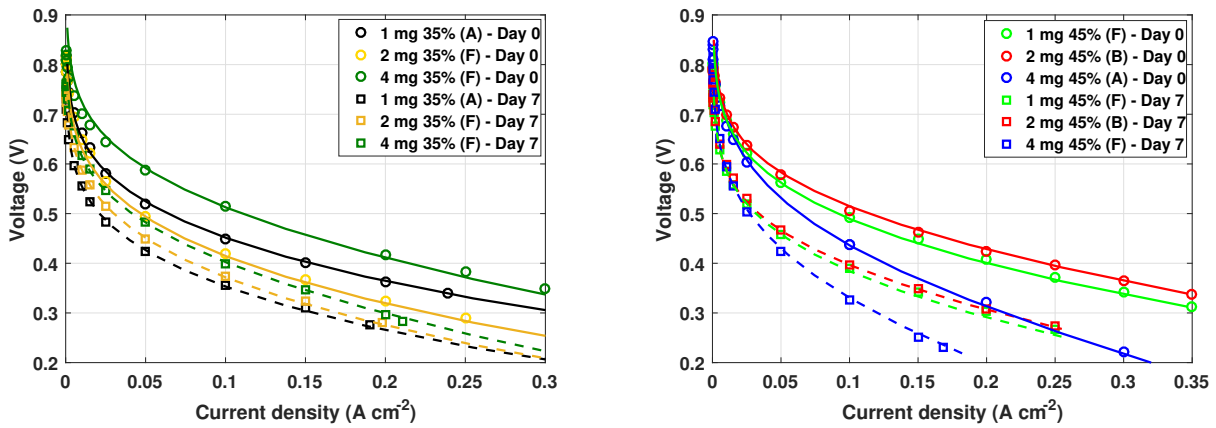
(a) 35%   **(b)** 45%

Fig. 6.3.: Polarization - Dots: experimental; line: model

(a) 35%

$[V]$	Day 0		Day 1		Day 7	
	0.015 A cm^{-2}	0.2 A cm^{-2}	0.015 A cm^{-2}	0.2 A cm^{-2}	0.015 A cm^{-2}	0.2 A cm^{-2}
1 mg	0.62	0.36	0.59	0.33	0.52	0.27
2 mg	0.62	0.32	0.61	0.31	0.56	0.28
4 mg	0.68	0.39	0.66	0.39	0.59	0.29

(b) 45%

$[V]$	Day 0		Day 1		Day 7	
	0.015 A cm^{-2}	0.2 A cm^{-2}	0.015 A cm^{-2}	0.2 A cm^{-2}	0.015 A cm^{-2}	0.2 A cm^{-2}
1 mg	0.66	0.41	0.63	0.38	0.56	0.3
2 mg	0.67	0.42	0.64	0.39	0.57	0.31
4 mg	0.65	0.33	0.61	0.27	0.56	0.2

Tab. 6.3.: Corresponding voltage at low and high currents - 160-hours potentiostatic holding

Diagnostic results are in line with the data acquired in operando. As evinced by *Table 6.3*, generally the *MEAs* ends up the 160 hours holding by losing circa 100

35%	1 mg		2 mg		4 mg	
	Day 0	Day 7	Day 0	Day 7	Day 0	Day 7
$\delta_{CCL}\,[\mu m]$	32		70		132	
$i_0\,[A\,m^{-3}]$	2880	576	960	480	2304	384
$\sigma_m^m\,[S\,m^{-1}]$	3.54	3.54	3.54	3.54	3.54	3.54
$\sigma_m^c\,[S\,m^{-1}]$	0.125	0.125	0.2	0.2	0.5	0.5
$\sigma_s^c\,[S\,m^{-1}]$	8.33	7.14	8.33	7.14	8.33	7.14
$C_{DL}\,[F\,m^{-3}]$	40e6	60e6	15e6	40e6	15e6	30e6

Tab. 6.4.: Optimized parameters applied to the model - *Day 0* vs *Day 7* - 35%

45%	1 mg		2 mg		4 mg	
	Day 0	Day 7	Day 0	Day 7	Day 0	Day 7
$\delta_{CCL}\,[\mu m]$	70		132		261	
$i_0\,[A\,m^{-3}]$	2304	384	1536	230	768	154
$\sigma_m^m\,[S\,m^{-1}]$	3.54	3.54	3.54	3.54	3.54	3.54
$\sigma_m^c\,[S\,m^{-1}]$	0.31	0.31	0.88	0.88	0.44	0.44
$\sigma_s^c\,[S\,m^{-1}]$	11.16	7.3	22	11	11.16	7.3
$C_{DL}\,[F\,m^{-3}]$	20e6	40e6	15e6	15e6	8e6	22e6

Tab. 6.5.: Optimized parameters applied to the model - *Day 0* vs *Day 7* - 45%

mV at both high and low currents. A slightly higher loss is observed for all the 45% samples, especially at 0.1 A cm^{-2} for the 4 mg, sign of the increasing ohmic losses. The comparison between *Day 1* and *Day 7* of these samples reveals that one third of the output loss belongs to the first 15 hours, underlining the importance of the ionic phase conductivity. Electronic pathways may have been hindered or flooding may have been induced more quickly due to the more abundant Nafion content. On the other hand, the effects of the first hours of degradation of the catalyst structure may be more appreciable in a *CCL* with initially more conductive ionomer promoting the *ORR*. The only trend exception is, as expected, the *2 mg 35%*, whose most significant loss amounts to 60 mV and belongs to the kinetic region, showing a good integrity of the *CCL* structure. It finishes performing better than the *1 mg 35%* in the whole operational range.

Accordingly, the model operational parameters reflect the polarization curves downwards shift by maintaining fairly constant values for all the properties but the exchange current density (*Table 6.4* and *Table 6.5*): the active area playing a role in

power generation has been reduced. The most substantial i_0 reduction is faced by the *2 mg 45%* and the *4 mg 35%*, which are the best performing *CCL*: the factor has decreased by almost 7 times, which has brought the polarization curves to perform basically the same as the *1 mg 45%*. This may originate from an initially active surface area wider than for the other samples, that has thus more margin to be reduced. It is peculiar that the least degrading *MEA* is the *2 mg 35%*, with a depletion of the 50% for the i_0. This contrasting behaviors emphasize the complexity of the internal mechanisms of a *PGM-Free PEMFC* and the importance of Nafion content optimization.

The linear relation existing between the *HFR* and *CCL* thickness allows to derive, as already done in *Section 4.2,* the ionic conductivity of the membrane and the solid phase conductivity. The results show a negligible alteration of the intrinsic properties of the electrolyte, while σ_s^c is divided by a factor of 1.5 for the 45% samples and 1.1 for the 35%. The contribution of the ionomer content to electron transport limitations is here confirmed. The *2 mg 45%* is the only one going under a more consistent worsening by halving its *CCL* ionic conductivity, as previously foreseen by the drastic relative increase of the *HFR*.

The conductivity of ionomer within the *CCL* appears instead unaltered from the fittings, which possibly indicates that the chemical attacks occurring during the operations affect mainly the carbonaceous support lowering only its conductivity.
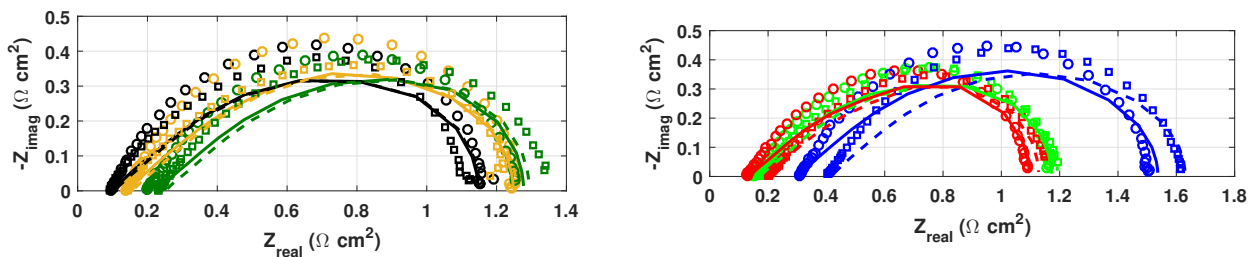
(a) 35%

(b) 45%

Fig. 6.4.: *Nyquist* at 0.1 A cm^2 - Dots: experimental; line: model

The dynamic state conditions are analyzed by means of the *Nyquist* plots of *Figure 6.4,* that make explicit the mainly ohmic nature of the losses at the reference current density of 0.1 A cm^{-2}. The charge transfer resistance corresponds to circa the same peak along the days, actually this tends to be shifted lower for the 1 and 2 mg samples, particularly for the 35% ones, confirming that the counter intuitive trend observed for the *2 mg 35%* of *Chapter 4* has not been just an isolated case. The total

$HFR\,[\Omega\,cm^2]$	35%			45%		
	1 mg	2 mg	4 mg	1 mg	2 mg	4 mg
Day 0	0.096	0.145	0.205	0.155	0.135	0.31
Day 1	0.096	0.13	0.18	0.135	0.135	0.34
Day 7	0.096	0.15	0.23	0.175	0.2	0.41
Relative increase	+0%	+15%	+28%	+29%	+48%	+32%

Tab. 6.6.: *HFR* values - 160-hours potentiostatic holding

impedance remains constant while the first intersection with the real axis slightly moves to the right (*HFR* exact values in *Table 6.6*), as expected from the 1 kHz resistance trend of *Figure 6.2* and the change in the σ_s^c as fitting parameter. This all results in a shorter linear branch that explains the constant value of σ_m^c.

The thicker 4 mg *MEAs* present instead a non changing R_{CT} coupled with a greater total impedance and relative increase in *HFR* compared to the other samples with less loading and same ionomer content. The key role of thickness is also underlined by comparing the resistance trends of *MEAs* with the same loading but more Nafion (*Table 6.6*). The *2 mg 45%*, that has started out with the lowest value, ends up being the most changing, as expected by the greatest reduction of the fitted σ_s^c.

Concerning the double layer capacitance, the *Bode* diagrams are approximated with increasing values of this parameter, which circa doubles from *Day 0* to *Day 7* for all the samples but the *2 mg 45%* that keeps it constant (*Table 6.5*). The same phenomena thus take place at lower frequencies on *Day 7* compared to *Day 0*.
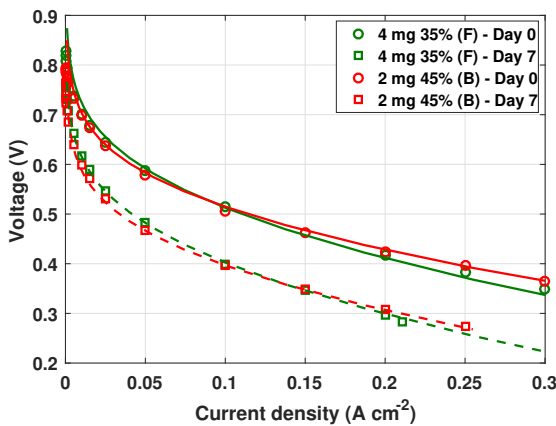
(a) Polarization
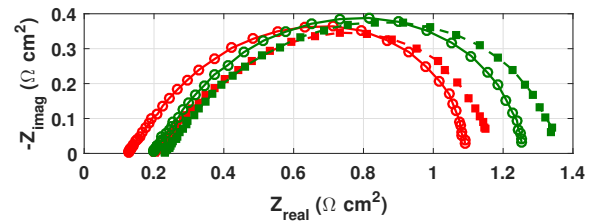
(b) *Nyquist* at 0.1 A cm^2

Fig. 6.5.: Best performing *MEAs* - Dots: experimental; line: model

The comparison between the best performing *MEAs - 2 mg 45%* and *4 mg 35%* - is shown in *Figure 6.5*. The trend observed during *Day 0* has not significantly changed: the higher catalyst loading performs better in the kinetic region, while more Nafion pushes the output in the higher currents range. On the other hand, this latter gap has been decreasing along the lifetime, as a result of a much greater lowering of electronic conductivity for the *2 mg 45%*. The better σ_m^c of the 45% allows it to have a lower total impedance and charge transfer resistance. From the observation of the life trend, it would have been though expected, if a longer holding had been carried out, to see the *1 mg 45%* and *2 mg 35%* to generate the most specific power.

The conclusions drawn from the observation of the diagnostic results are confirmed by the in operando *EIS* measurements during the entire test duration. The impedance spectra of *Day 1 - 3 - 6* for the imposed reference current of 0.6 A (0.0284 A cm^{-2}) are plotted in *Figure 6.6*.
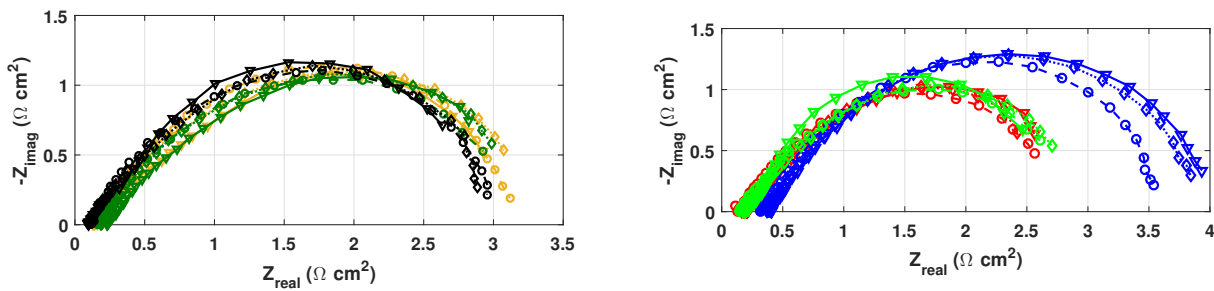
(a) 35%   **(b)** 45%

Fig. 6.6.: In operando *EIS* at 0.6 A. Circle: *Day 1*; diamond: *Day 3*; triangle: *Day 6*

The highest charge transfer resistance for this low current operation range belongs to the *1 mg 35%* in *Figure 6.6a*, showing the thinnest thickness limitations in the kinetic regimes; and to the *4 mg 45%* in *Figure 6.6b*, confirming the negative effect of the excessive thickness. In general though, the peak values are similar for both the 35% and 45%, as in the *Nyquist* plots resulting from the characterization procedure; while the increase in the total impedance is more relevant for the highest loading, as previously noticed.

The current profile evolution in time along the *MEA* is presented in *Figure 6.7* at the reference current density of 0.1 A cm^{-2}.

(a) 35%   **(b)** 45%
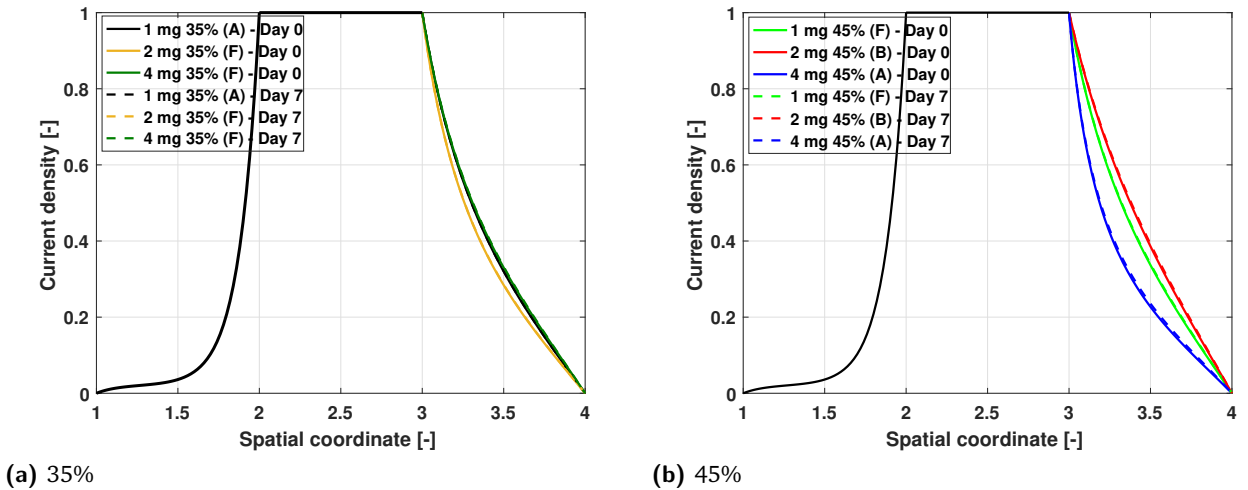
Fig. 6.7.: Modeled current density profile along the *MEA* at 0.1 A cm^2

As seen by the sensitivity analysis carried out in *Chapter 3,* the only operating parameter causing a sensible variation in the current density profile within the *CCL* by changing of only one order of magnitude is the ionic phase conductivity, which remains constant in the current modeling. The present decrease of σ_s^c is not enough to appreciate a curve alteration. The profiles result therefore basically overlapped, with a slightly more noticeable shift of the reaction towards the *GDL* for the 45% *MEAs* (1.5 reduction factor against 1.1 of the 35%).

Backpressure effect   On the last day of testing, an additional characterization, particularly the *[CF2]*, has been executed in order to have more means of comparison and to evaluate the cells response to a backpressure boost.

(a) 35%   **(b)** 45%
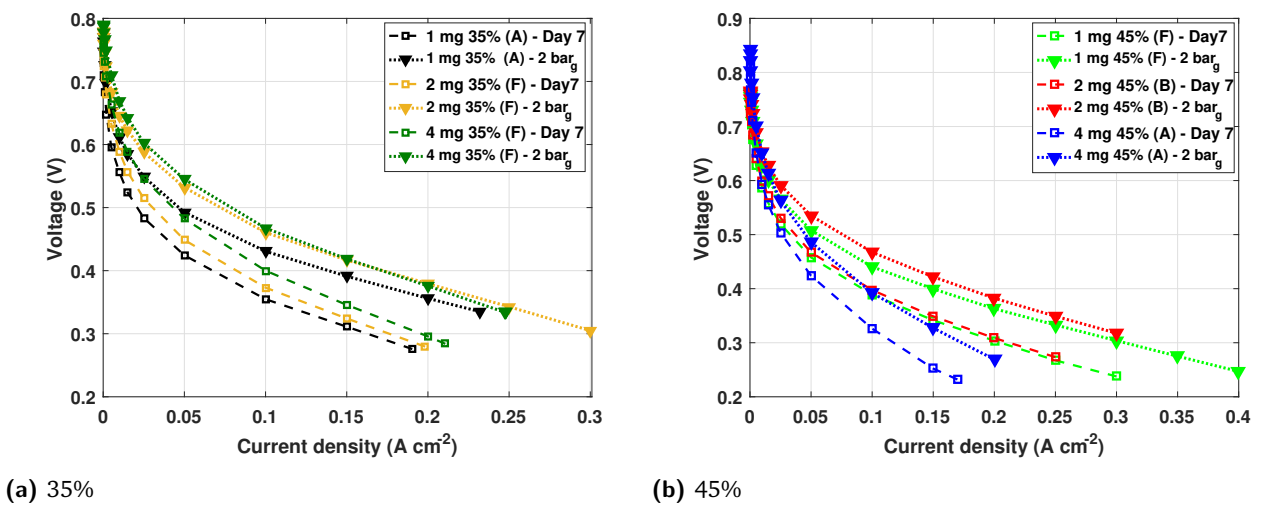
Fig. 6.8.: Backpressure effect - Polarization

(a) 35%   **(b)** 45%
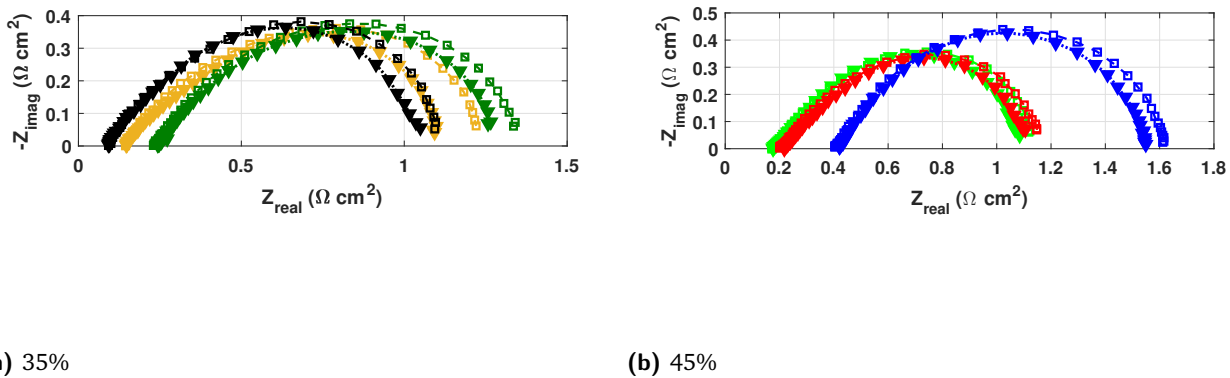
Fig. 6.9.: Backpressure effect - *Nyquist* at 0.1 A cm^{-2}

In the preliminary analysis of *Chapter 4*, the increase of this working parameter has lead performances on *Day 7* of the *2 mg 35%* and the *2 mg 45%* to be very similar to those of *[CF]* characterization on *Day 1*. Also in the present analysis the 2 mg are the samples taking the most advantage from the change of the working conditions: the 35% reaches the corresponding 4 mg, and the 45% detaches from the corresponding 1 mg. The *2 mg 35%* presents moreover the most substantial reduction in the total impedance, mirroring an improvement especially in the ohmic regime.

The major alteration in the shape is faced by the *1 mg 35%*, which benefits from the backpressure especially in the ohmically limited region. This may mean that the best exploitation of the thinnest samples requires for a standard operating pressure higher than 0.5 bar$_g$ in order to allow for the best protons and electron transport since both the catalyst loading and the ionomer content are the scarcest. The least affected *MEAs* are the 4 mg: degradation of too many interconnected carbon nanotubes may not be recoverable by only increasing the pressure of the reactant. Both the *HFR* and the linear branch do not go under specific changes: current density profile generated by the *ORR* is not moved. Polarization curves obtained from this characterization end up being very similar to those of *[CF]* on *Day 1*, except for the *1-2 mg 35%* that overcome even *Day 0* performances.

In conclusion, backpressure results to help mostly in the promotion of the *ORR* in the cells with the least ionic pathways, pushing the protons to the active sites.

6.3.2 Tests under different *RH*

This paragraph concerns the experiments carried out after the 160 hours poten-tiostatic holding: purposes and working conditions drastically change. The non degrading action of nitrogen to the cell structure has been very much exploited

during the long periods necessary for the stabilization of *MEA* operation subjected to a different relative humidity.

Figure 6.10 and *Figure 6.11* show the effects that a progressive drying of the cell has on the performances.
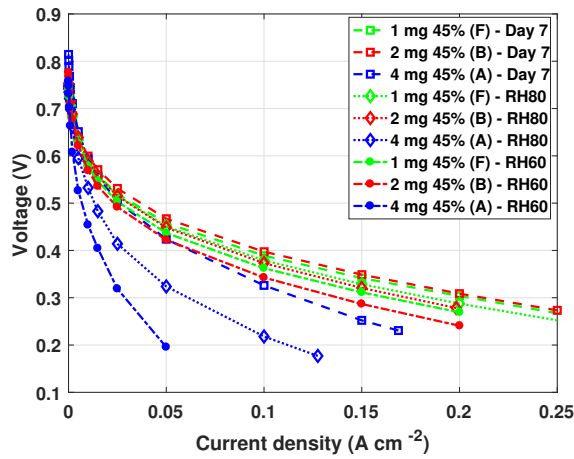
(a) Polarization

**Fig. 6.10.:** Relative humidity effect
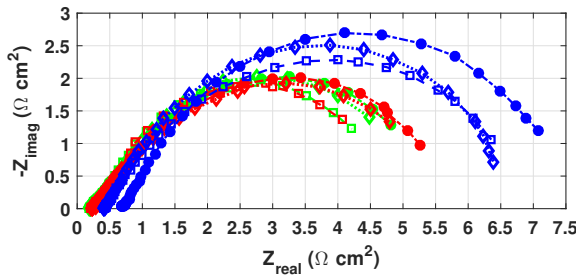
(a) Nyquist at 0.015 A cm^2
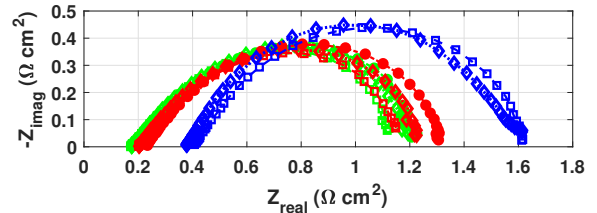
(b) Nyquist at 0.1 A cm^2

Fig. 6.11.: Relative humidity effect

It is evident that the most impacted *MEA* is the *4 mg 45%*, a dry-out is fatal for its performances. Its *EIS* measurement at the reference current density has not been executed because the point has not been reached. Even if the difference in the voltage response between *[CF]* and *[RH80]* is considerable, this is not translated into a sensible variation of the impedance spectra: they basically overlap at 0.1 A cm^{-2}. This means that, for this current density, the relative humidity has just affected the surface of the active catalytic area, reducing it: protons are stuck in a

thinnest layer on the membrane/*CCL* interface. However, the shapes of the curves in the smallest currents regime reveal changing kinetic mechanisms leading to a final almost vertical *[RH60]* output. This is translated into an increase in charge transfer resistance at the smallest current density (*Figure 6.11a*) and consequently in the Tafel slope. *[RH60]* for the 4 mg is the only case for which even the *HFR* substantially increases, and the semi-circle finishes with a total impedance that is almost double the corresponding value of the 1 mg. A different behavior is observed for the 1 and 2 mg samples: performances keep reducing with decreasing flow saturation, but the change is less drastic. Only the *2 mg 45%* appears slightly more affected than the 1 mg by the period under *[N2-RH60]*. In the ohmically limited regime, the 2 mg spectra in particular reveal the most negative impact that a less saturated inlet flow has on its intrinsic ionic conductivity: the total impedance grows as RH drops.

Figure 6.12 and *Figure 6.13* represent the comparison between fully saturated *[CFs]* before and after the period under varying relative humidity and in-between characterizations.
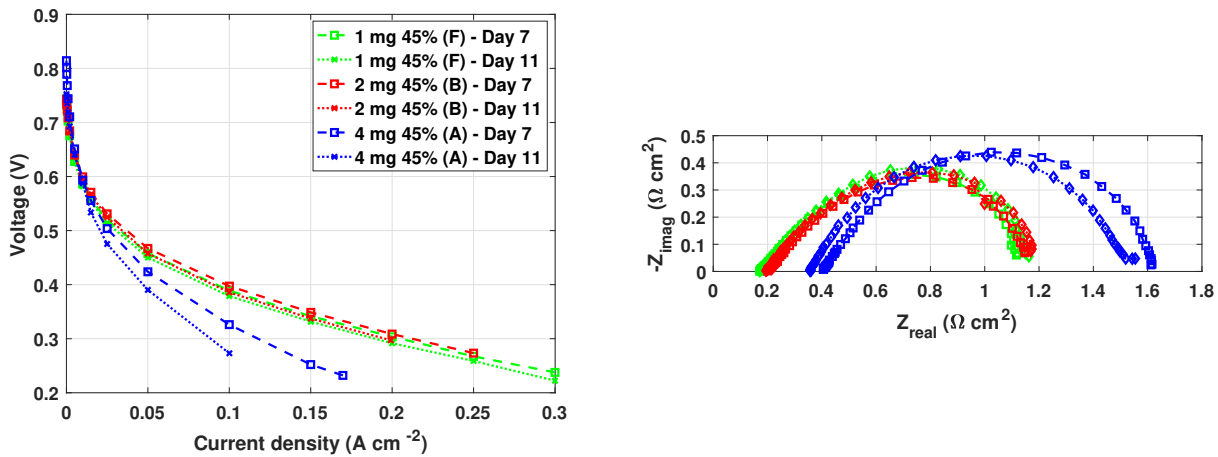
(a) Polarization

(b) Nyquist at 0.1 A cm^2

Fig. 6.12.: *[CF]* pre and post period at different *RH*

As expected, the greatest difference can be observed for the 4 mg, that decreases its output voltage while increasing the *HFR*. On the other hand, once they are put back to be fully humidified, the 1 and 2 mg samples results to be unaffected by the four days spent in nitrogen and the subsequent characterizations.

This is all confirmed by both the zoom on the *OCV* section of the polarization and the Tafel plot. The first shows identical curves for the 1 and 2 mg, while the thickest *MEA* undergoes a noticeable voltage drop. The second shows the same governing mechanisms for the thinnest samples, while the 4 mg presents a peculiar behavior that sees its *[CF - Day 7]* as the best performing up to 0.01 A cm^{-2}, where then its *[CF - Day 11]* performs better than its *[CF - Day 7]*, but both worse than the 1 and 2 mg *[CFs]*.
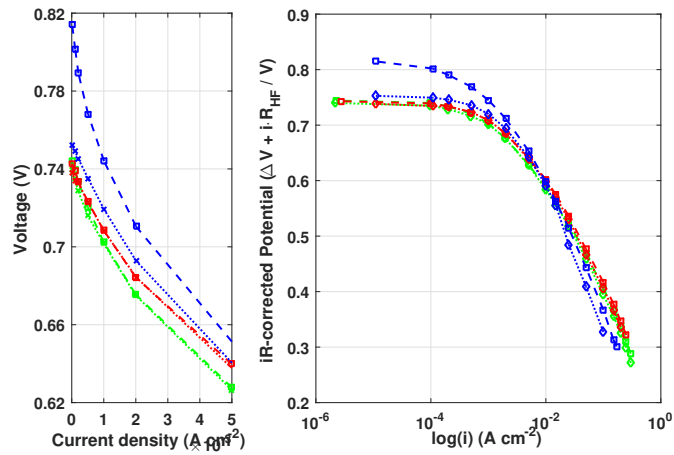
Fig. 6.13.: *[CF] pre and post period at different RH*

According to the schedule presented in *Table 6.2*, the periods under different relative humidities have been characterized also by means of diagnostics in nitrogen. The following graphs show how *RH* and backpressure affect the results obtained from the techniques described in *Section 2.4*.
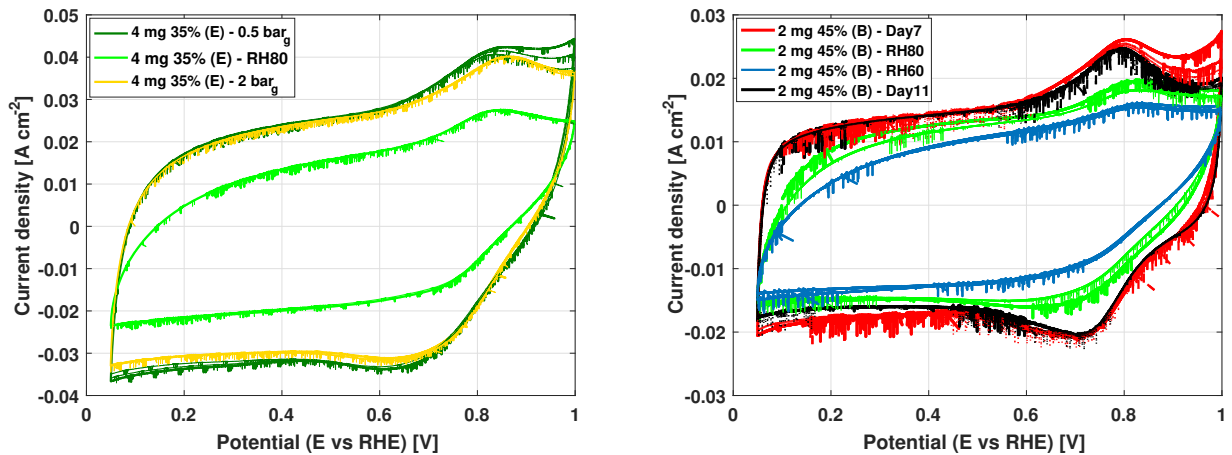
(a) *4 mg 35%*

(b) *2 mg 45%*

Fig. 6.14.: *RH/BP effect - CV*

As previously discussed, quantitative analyses are not very accessible on these measures.

What can be observed starting from the *CV* is a more definite evidence of peaks corresponding to the oxidation/reduction peaks in traditional *Pt/C PEMFC* during operation under fully saturated flow. This particular shape could be linked to similar electrochemical reactions happening to the iron molecules rather than platinum. 100% *RH* operating condition has been further used as an additional mean of control

(a) *4 mg 45%*
(b) Summary - 45%
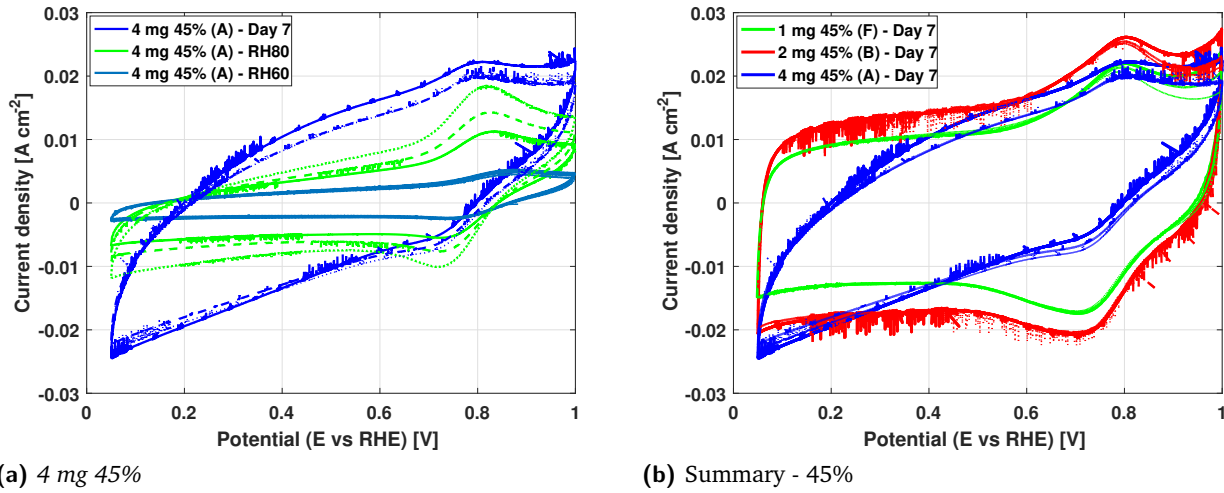
Fig. 6.15.: *RH/BP* effect - *CV*

regarding the C_{DL} parameter fitted in the model. Observing all the *CVs* shapes, the potential at which the double layer current density has been evaluated has been chosen where averagely the curves have the flatter slope: 0.4 V.

$$C_{DL} = \frac{\Delta j}{SR \cdot \delta_{CCL}} = \left[\frac{F}{m^3}\right] \tag{6.1}$$

Calculations for each cell validate the order of magnitude used in the model, some values are more similar (25e6 against 22e6 $\mathrm{F\,m^{-3}}$ used in the model for the *4 mg 45%*), while other deviate more (80e6 against 40e6 $\mathrm{F\,m^{-3}}$ used in the model for the *1 mg 45%*).

As no *ORR* occurs, backpressure confirms to have no influence on the output (*Figure 6.14a*). On the other hand, relative humidity clearly alters the curve shape: it tends to be symmetrically squeezed towards the zero axis, making the aforementioned peaks less evident. This holds for both the 35% and 45% *MEAs*. Moreover, as shown by *Figure 6.14b*, the period under different *RHs* appear not to be affecting the *2 mg 45%* active area, confirming what previously observed in the characterization of *Figure 6.12*. The most peculiar behavior is presented by the thickest *CCL* (*Figure 6.15b*): even if the current densities corresponding to the extreme imposed potentials are consistent with the other data, the internal trend of the 100% RH curve resembles a diagonal and no flat part is observed. As the saturation of the flow decreases (*Figure 6.15a*), the *CV* plot tends to stabilize to a more regular shape, and the squeezing phenomenon is particularly verified.

In order to provide for more consistent and quantitative information, more experimental work has to be conducted.

Figure 6.16 represents a focus on the *CL* resistance: unlike the *CV* plot, here the period under different *RHs* changes the curve shape by increasing the resistance of
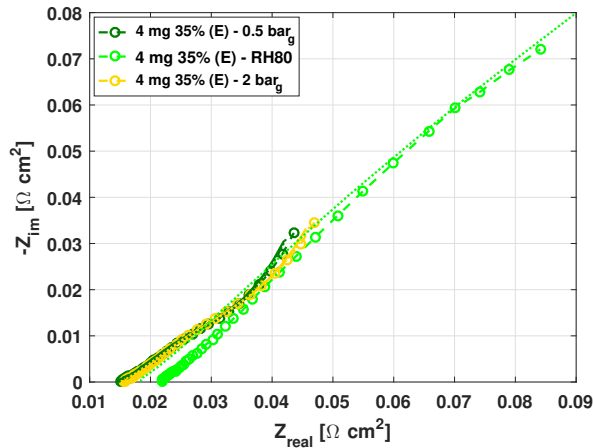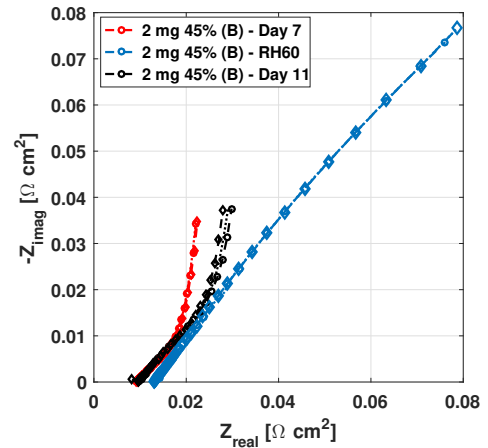
(a) 35%   **(b)** 45%

Fig. 6.16.: *RH/BP effect - CLR*

the catalyst layer (*Figure 6.16b*). Backpressure has again no influence on the output (*Figure 6.16a*). Tests with not fully saturated flow reflect the complex phenomena happening within the *CCL* with a line much different from the ideal vertical shape, resembling a bisector, no R_{CL} can be determined. The intersection with the real axis shows also an increasing ohmic resistance.

Further tests are necessary to understand the switch in output as *RH* drops.

Lastly, in *Figure 6.17*, *LSV* results are exposed.
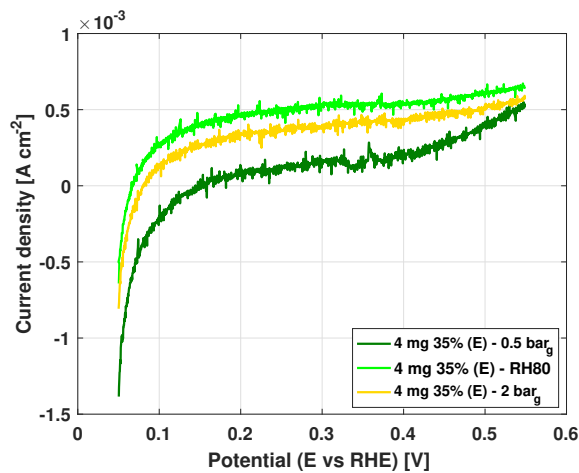
Fig. 6.17.: *RH/BP effect - LSV*

This plot is the only one presenting a substantial difference between the test at 0.5 bar$_g$ and the test at 2 bar$_g$. Both an increased backpressure and a decreased relative humidity are translated into an upward shift of the curve, coupled with a less steep change in slope starting from 0.35 V. This behavior reflects a more intense membrane decay: Nafion particularly suffers from non-optimal hydration,

and excessive compression may contribute to a thinning of the electrolyte.
The change in slope of the *LSV* curve has to be further deepened: more studies are required.

6.4 Additional tests

Once the standardized potentiostatic test has been carried out for all the *MEAs*, two further modified tests have been executed. The purpose has been the study of the impact on the degradation process of the alteration of two considered relevant parameters, in particular the backpressure and the reactant nature.
In practice, the procedure that has been followed from *Day 1* to *Day 7* has been kept the same, but for one single operating parameter. The warm-up has been executed in the exact same way as described in *Section 2.3.2*, while the rest of the *BoL* procedure (the overnight at 0.6 V) has undergone the corresponding parameter change.

6.4.1 Backpressure effect

The effect of a change in backpressure has been investigated for the *4 mg 35%*: operations have been carried out at 2 instead of 0.5 bar_g. Every day, a period of one hour has been spent at 0.5 bar_g in order to understand the effect of the higher backpressure on the degradation process.
Results of the 160-hours potentiostatic holding are below exposed.

(a) Raw data   **(b)** Rescaled data
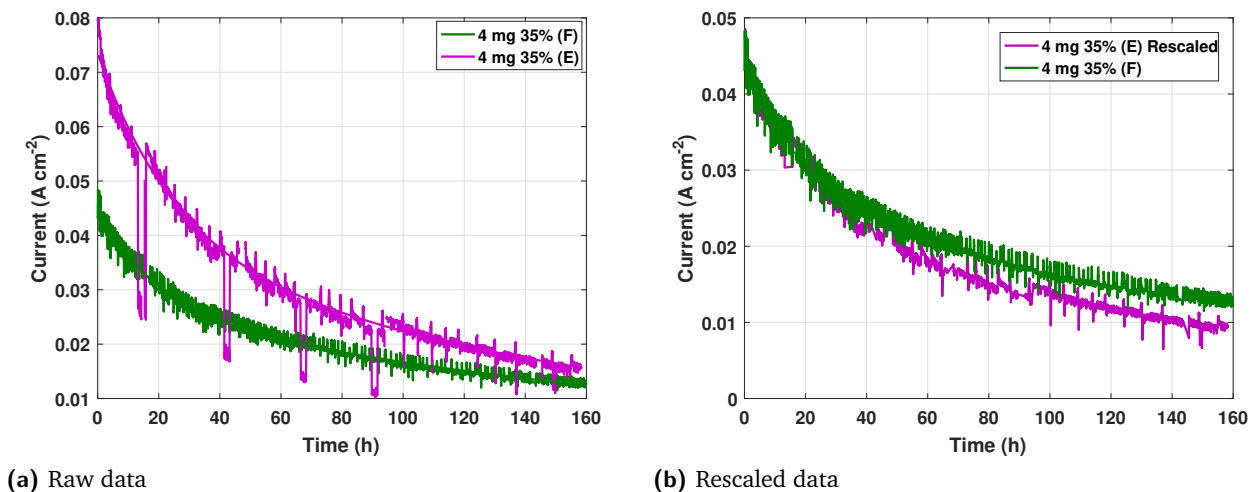
Fig. 6.18.: Current density trend - potentiostatic test (0.5 vs 2 bar_g)

Quantifying the degradation rate of the *[CONT06V2BP]* to 7.8 mA h^{-1}, against the 4.1 of the *[CONT06V]* makes even clearer the dramatic effect that an higher
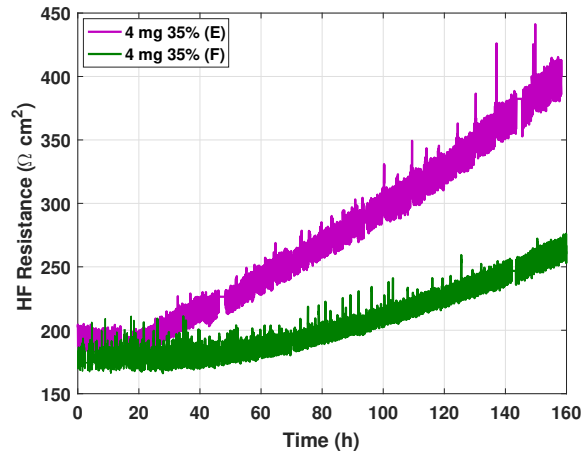
Fig. 6.19.: 1 kHz resistance - potentiostatic test (0.5 vs 2 bar$_g$)

backpressure has on the decay of the *MEA*. Furthermore, the periods during which the pressure has been put back to the original conditions show a comparable entity of the loss. The rescaling of the experimental data (according to the procedure of *Section 2.3.5*) on the highest current density of the *4 mg 35% (F)* shows that the more drastic degradation rate suffered by the *4 mg 35% (E)* starts to become appreciable not right away, but after some hours of operation, when the side effects of an excessive compression take place.

From *Figure 6.19*, the relative increase in the 1 kHz resistance can be derived: the new operating conditions bring to an increase of +102%, against the +42% of the other sample. Ohmic regime is thus the most affected, as seen in *Figure 6.20*.
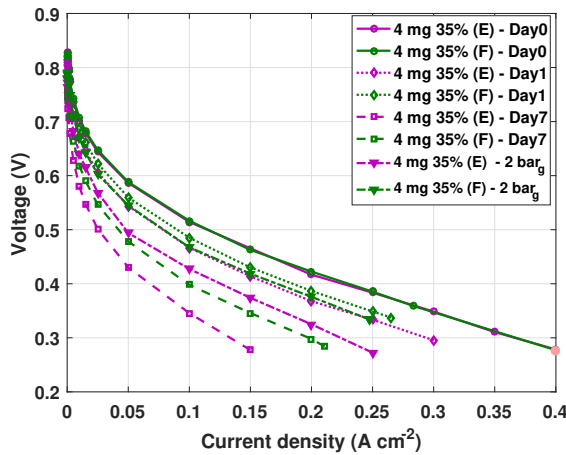
(a) Polarization
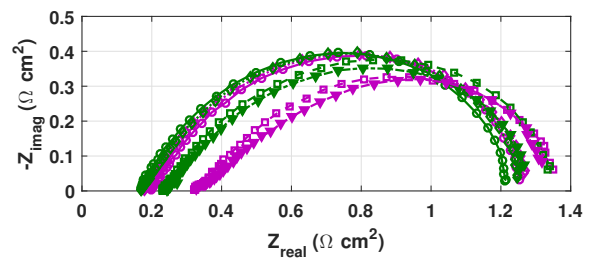
(b) *Nyquist* at 0.1 A cm^2

Fig. 6.20.: *4 mg 35%*: 0.5 vs 2 bar$_g$ performances

As already foreseen, performances on *Day 0* overlap assuring repeatability. Discrepancies on *Day 1* are still irrelevant both in the polarization and *Nyquist* curves,

as expected by the first 20-hours result in the rescaled current density plot. Nevertheless, *HFR* already shows a greater value while not interfering with the total impedance. It is worth mentioning that all the diagnostics have been carried out at the reference backpressure, in order to make more meaningful comparisons. On *Day 7* differences are well marked: *HFR* has drastically increased, and the peak on the *Nyquist* plot has moved to the right, extending and flattening the linear branch, revealing problems in the electrons transport that are also reflected in a steeper polarization curve. Issues may also regard the status of the membrane, as the previous *LSV* measurements have shown the negative impact of a backpressure increase. On the other hand, the charge transfer resistance has lowered and the total impedance has not noticeably changed its value: the action of the backpressure may have not undermined the ionic phase.

By means of the *[CF2]* characterization, the different nature of the *[CONT06V2BP]* degradation compared to the *[CONT06V]* is evinced: while the *4 mg 35% (F)* performances go back to *Day 1* outputs, they are not so successfully recovered for the *4 mg 35% (E)*.

6.4.2 Oxygen concentration effect

The effect of a change in reactant concentration at the cathode inlet flow has been investigated for the *4 mg 45%*: operations have been carried out with a constant flow of pure O_2 instead of air. In this case, no daily 1-hour period back to the reference conditions has been accomplished, being the reactant change a little more complex on the workstation.

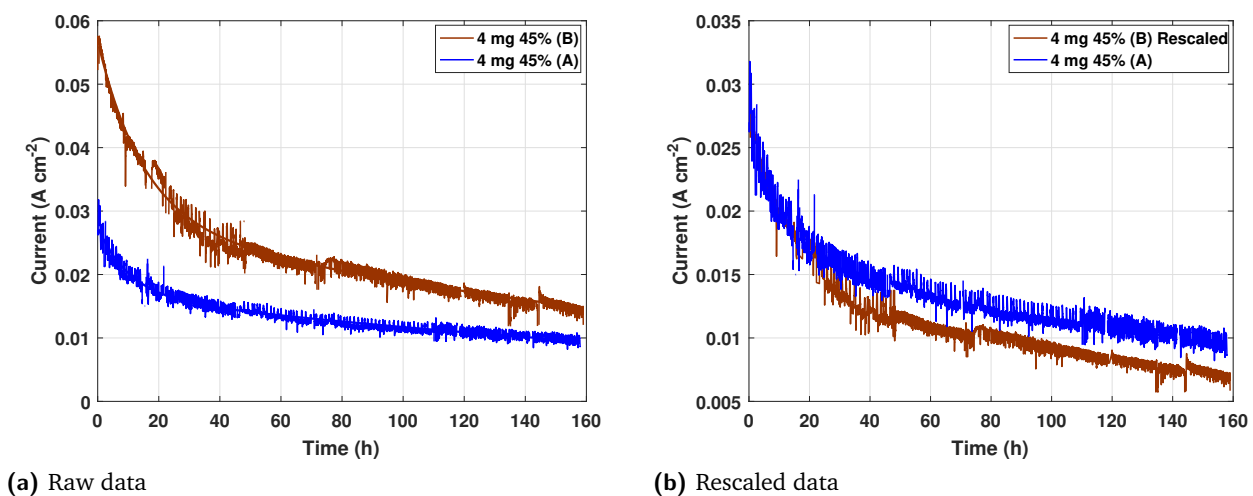Results of the 160-hours potentiostatic holding are below presented.

(a) Raw data   **(b)** Rescaled data

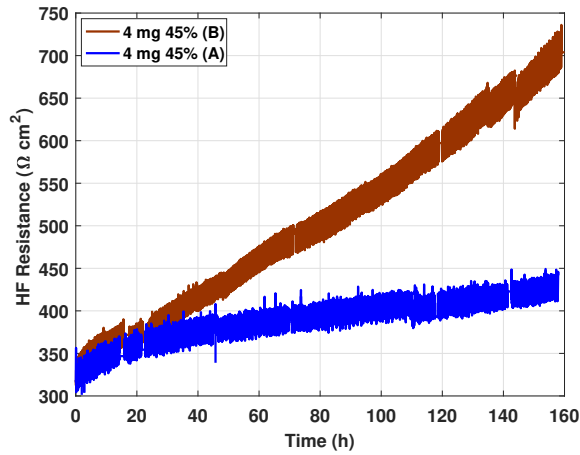**Fig. 6.21.:** Current density trend - potentiostatic test (air vs O_2)

Fig. 6.22.: 1 kHz resistance - potentiostatic test (air vs O_2)

In the case of *[O206V]* the degradation rate amounts to 5.8 $\mathrm{mA\,h^{-1}}$, which is more than double than the 2.6 of the *[CONT06V]*. Higher reactant concentration thus results to be more aggressive than higher backpressure. As in the previous test, the negative effect on decay of the new operating conditions becomes evident only starting from the 20th hour, as underlined by the rescaled current density plot. *Figure 6.22* allows for the calculation of the relative increase in the 1 kHz resistance: +109% of the *4 mg 45% (B)* in contrast with +31% of the *4 mg 45% (A)* stresses the impact of pure O_2 on the *MEA* structure. A drastic decrease of σ_s^c may be thus the main reason for this cell behavior, as seen in *Chapter 5*. Additional losses may have been caused by *ROS* formation from hydrogen peroxide.

Performances are characterized by means of *Figure 6.23* and *Figure 6.24*.
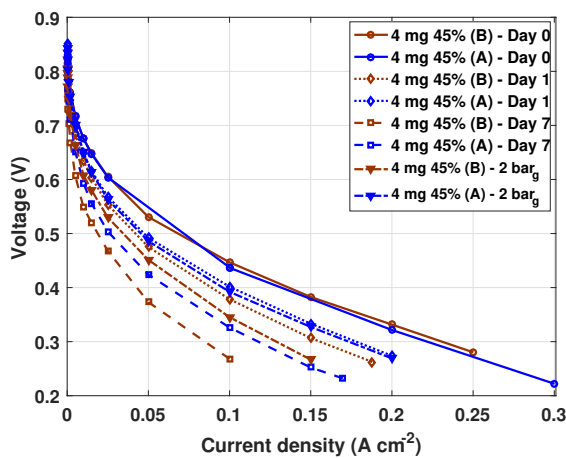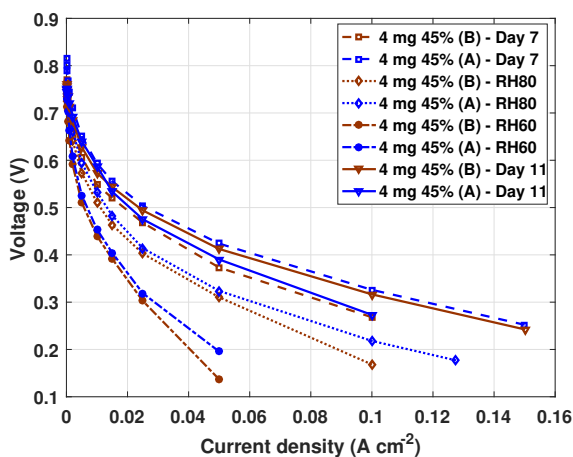

(a) Polarization
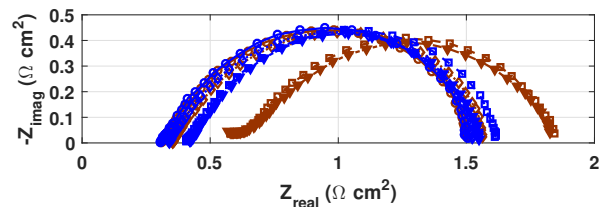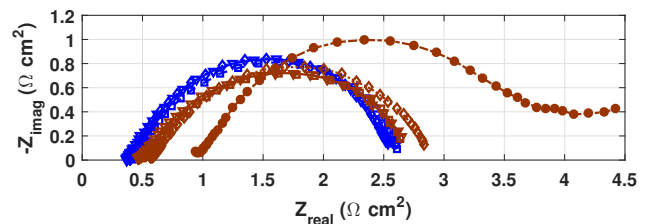

(b) *Nyquist* at 0.1 A cm^2

Fig. 6.23.: *4 mg 45%*: air vs O_2 performances *[CF] - [CF2]*

Given that all the measurements have been executed under reference *[CF]-[CF2]* conditions, repeatability is assured on *Day 0*, while *Day 1* performances start to differentiate especially in the higher currents region, sign of the rapidly growing *HFR*. *Day 7* presents differences right from the smallest currents, coupled with a distinct increase in *HFR* and total impedance. Even for this working regime, the final impedance spectra appear to have a longer linear branch and lower imaginary peak. *Nyquist [CF2]* curve for the *4 mg 45% (B)* does not present relevant alterations compared to *Day 7 [CF]*: increasing backpressure is not enough to recover performances to a significant level, as also clarified by the polarization plot. As the curve shift resembles the behavior of the previous test in a more remarkable way, it is hypothesized here too a negative action concerning particularly the solid phase conductivity.

The results in *Figure 6.24* outline the effect of periods spent under different *RHs*.

(a) Polarization

(b) *Nyquist* at 0.05 A cm^2

Fig. 6.24.: *4 mg 45%*: air vs O$_2$ performances *RH* effect

The dry-out of the *CCL* under nitrogen appears to be very beneficial to the sample subjected to pure O$_2$ for 160 hours: performances get closer to the reference sample, and at the end of the varying saturation test, *[CF]* performances not only are better than the corresponding *4 mg 45% (A) [CF]* but also better than *Day 7 [CF]*. The hypothesis is then that the main reason for the previous poor output originates from a consistent flooding occurring under pure oxygen: all the reachable sites react but the action of the Nafion is not enough to drag out all the produced water that so accumulates in the micropores, making them unavailable.

Figure 6.24b presents a particular trend for the *EIS* measurement at *[RH60]* for the *4 mg 45% (B)*: either the measurement may have been unsuccessful, or other phenomena have been about to happen. Further studies are again necessary.

6.5 Conclusion

The degradation analysis exposed in this chapter has allowed for a standardization of operation that has lead to well comparable results constituting the basis for further characterizations, such as those carried out in the last section.

Since the main focuses of the test have been repeatability and stability of the working conditions, the diagnostics requiring an interruption of the regular operations have been avoided throughout the main body of the holding.

Being then the procedure the same for all the *MEAs*, the gathered experimental data has brought to establish interconnections between the catalyst layer morphology and the decay phenomena.

The main conclusions drawn along the analysis are below listed.

* **The least degrading *MEA* is the *2 mg 35%*, the optimal configuration fr the degradation is thus identified**. *4 mg 45%* starts out with the lowest current density response, and finishes better than the other 45% samples.

* **More than the 50% of the total net current loss generally occurs in the first 20 hours of operation**. Exceptions are the same thickness and best performing *2 mg 45%* and *4 mg 35%*, presenting a more homogeneously spread degradation, but with a highest rate $[\mathrm{mA\,h^{-1}}]$. This suggest that degradation may be strictly linked to more physical mechanisms.

* Total cell impedance increases substantially in time only for the 4 mg samples, while the charge transfer resistance remains circa constant showing no remarkable change in the governing mechanisms at the reference current. For the 1 and 2 mg *MEAs*, this parameter even tends to be lowered with time. Along the test duration, σ_m^c remains circa constant, suggesting that proton transport limitations do not have a fundamental impact on performance drop along the electrode (more specific tools would be needed to extend the consideration to a local level).

* The fitting parameters changing in the model from *Day 0* to *Day 7* are: i_0, σ_s^c and C_{DL}, evincing the dominant natures of the losses. Current profile shape is thus not particularly affected. **The parameter that mostly faces the consequences of the ongoing decay is i_0, which, given its definition in *Chapter 3*, shows that performances worsening can be mainly ascribed to a loss in active sites**.

* *MEA* compression has a negligible effect on performances in the investigated range.

* Averagely the voltage response during characterization drops of circa 100 mV, with a slightly higher loss for the 45% *MEAs*, which can be the result of excess thickness and/or Nafion squeezing the *ORR* on the membrane/*CCL* interface.

* High frequency resistance trends are particularly function of the electrode thickness, growing more with time as they are thicker. It results that the main associated mechanism is the lowering of electrical conductivity within the *CCL* with time.
* The 2 mg performances benefit the most from a boost in backpressure: active sites are not deactivated but rather isolated.
* Characterization under not fully saturated flow is particularly suffered by the thickest *CCL*, both in the kinetic and in the ohmic regimes. Once the sample is put back to 100% *RH* performances drop, unlike the other samples that present polarization and *EIS* curves much similar to those of the *[CF]* previous the tests under different relative humidities.
* Standard electrochemical diagnostics in H_2/N_2 give dissenting results compared to *Pt/C PEMFC*, these instruments will have to be appositely re-thought for this specific catalyst. *CV* plots have been useful to understand the double layer trend in accordance with the numerical model.
* The 160-hours potentiostatic holding under a four times higher backpressure causes initially a much higher current output, but also a much greater degradation rate and *HFR*. This is translated in a more significant performances drop, that seems to be particularly attributed to a lowering in the electronic conductivity according to the impedance spectra shapes. This suggests a strong interconnection between *ORR* rate and degradation mechanisms.
* The 160-hours potentiostatic holding under a five times higher oxygen concentration causes initially a much higher current output, but also a much greater degradation rate and *HFR*. The observed performances recovery following a dry-out of the *CCL* has brought to consider the micropore flooding as a relevant cause of performances drop during O_2 operation, which has to be associated to the previously observed more affecting σ_s^c worsening.

Conclusions

<div style="text-align: right; font-size: 3em;">7</div>

In the present work, the performances of Fe-N-C *PEMFC* cathode catalyst layers have been analyzed in the light of a future application of this technology on commercial scale. The main issues of this kind of catalyst layer are: poor volumetric activity compared to Pt catalyst layers, that results in thicker *CCL* with higher transport losses; and poor stability in typical operating conditions of a fuel cell. Accordingly, the focus of the investigation has been the characterization of the performance stability and durability of materials along the aging process, trying to relate key structural parameters, such as catalyst loading and ionomer content in the *CCL*, with the observed cell response. A standardization of operation protocol has been outlined in order to allow for relevant comparisons aimed at defining the main ongoing degradation phenomena according to the specific working conditions. A better comprehension of the complex physical phenomena has been pursued through the coupling of experimental campaigns with a macro-homogeneous one-dimensional *PEMFC* model developed within the *MRT Fuel Cell Lab* that simulates both the steady and dynamic state operation. This allows for an interpretation that links the experimental results to the physical parameters proper of the *CCL*. The impact of each variable on the polarization, *Nyquist* and *Bode* plots has been initially weighed up by means of a sensitivity analysis. Suitable configurations for optimal performances and stability have been further identified among the tested range of samples.

The degradation pathway followed by *PGM-Free PEMFCs* can be structured in two main periods that find their borderline at the 15th hour of operation: the preceding time is marked by the strongest exponential decay rate of the performances, generally accounting for more than the 50% of the total net output loss incurred during the entire lifetime; while the succeeding presents an attenuated trend for the performance stability decay. This behavior has already been observed in the literature, on the other hand the associated physical mechanisms remain unknown, and the absence of a rigorous operational protocol in the *PGM-Free* community does not allow for meaningful comparisons of performances. On a wider scale, a standardized procedure will help in better evaluating not only the structural parameters on the same type of catalyst layer (Fe-N-C in the current study), but also the effects on performance stability of different metals (e.g. cobalt, nickel, manganese) employed in the catalyst synthesis. The original protocol developed within this work has thus the purpose of representing a valid starting point for a further community-recognized

standard definition.

A preliminary analysis characterizing the *BoL* of each *MEA* has emphasized the importance of the thickness on performance: the samples giving the best outputs are found to be the *2 mg 45%* and the *4 mg 35%* which have the same thickness rather than common catalyst loading or ionomer content. Thickness is found to be a delicate parameter to be optimized since, as it increases, the kinetically controlled regime results favored, while the ohmically limited region suffers from an *ORR* pushed towards the membrane/*CCL* interface. In addition, *HFR* is also much dependent on this parameter: as the electrode thickens, the resistance assumes an ascending trend and a higher value. The relevant thickness leads moreover the resistance to be mostly dependent on the electronic conductivity of the catalyst layer, whose value is one order of magnitude greater than the corresponding ionic conductivity of the material.

At the end of the standardized potentiostatic procedure, the comparison between the characterization results of *Day 0* and *Day 7* fitted with the physical model has allowed to delineate the predominant nature of the aging losses. It seems that the durability worsening can be mainly ascribed to a loss in active area. Nevertheless, the carried out measurements have not allowed to understand if the loss concerns a reduction in the number of active sites, rather than a reduction in the specific activity per site. In this regard, ex-situ analyses of the composition of the surface of the catalyst are necessary. The fairly parallel downward shift of the polarization curves that reduces its *OCV* according to the performances trend (very rapid at the beginning), coupled with *Nyquist* plots changing their *HFR* and total impedance value over time is well reflected by the fitting parameters evolution within the model. In fact the parameter that mostly faces the consequences of the ongoing decay is i_0, the exchange current density, which is strictly correlated with the intrinsic catalytic activity being a proxy of the utilization of the active area. Even though it is not possible to safely identify if the most affected by the physical degradation phenomena is the site density or the turnover frequency of the sites, this parameter points out the progressive decrease in activity to be the main cause of performances drop. Being σ_s^c the only other variable subjected to a variation, the hypothesis of the electronic pathways to be the most affected by the oxygen action is validated.

Further tests involving a change in the nature of the inlet cathodic flow have allowed the evaluation of the impact on stability and performances of pure oxygen and nitrogen. A more concentrated reactant is reflected in higher outputs, while the performances during continuous operations and characterizations decrease at a more than double rate compared to operations under air; and the *HFR* suffers from a sharp unrecoverable rise. Performances however appear to be and potentially recoverable in contrast with the *HFR*. In fact, performances in air following a period in O_2 do not particularly suffer from it; and a potential reversibility of the degradation due to O_2 appears to be possible after a dry-out period. Micropore flooding is hence believed to be the cause, as in pure oxygen sites that would not work in air due to

local transport resistances are reachable. This hypothesis demands of course for further confirmations. The catalyst feature whose alteration results in such behaviors is the solid phase conductivity, indicating that the attacks of the oxygen are mainly against the electron-conductive carbonaceous paths. Operation under inert confirms the *ORR* to be the most influencing in the decay process: in the studied range, current/voltage (according to the ongoing test) response after a period in nitrogen restarts from the last value previously registered.

Among all the causes of overpotential loss for *PGM-Free PEMFCs*, it has been possible to consider the contribution of mass transport, and in particular of molecular diffusion, to be negligible for the studied operating range.

The results of the standardized protocol carried out at a higher backpressure suggests that the physical degradation mechanism affecting the performance stability is function of the operating condition.

In conclusion, even if there is still a long way to go for a commercial scale consolidation of this technology, there are still many aspects that have to be better investigated and improved. In this regard, more tests based on a reference are necessary, and ex-situ analyses would be very helpful in the understanding of the evolution of the morphological structure of the *PGM-Free CCL* over time. The aforementioned standardized protocol could be adopted by the *PGM-Free* community, in order to better outline the effects of structural parameters of the catalyst layer on the performance stability, and evaluate the materials durability. The main purpose of its rigorous application is therefore contributing in the development of more stable catalysts for a future commercialization.

Acronyms

Symbol	Meaning
ACL	Anode Catalyst Layer
BoL	Beginning of Life
CCL	Cathode Catalyst Layer
CV	Cyclic Voltammetry
ECSA	ElectroChemically active Surface Area
EIS	Electrochemical Impedance Spectroscopy
EoL	End of Life
EXAFS	Extended X-ray Absorption Fine Structure
GDL	Gas Diffusion Layer
HFR	High Frequency Resistance
LSV	Linear Sweep Voltammetry
HOR	Hydrogen Oxidation Reaction
MEA	Membrane Electrode Assembly
MPL	MicroPorous Layer
OCV	Open Circuit Voltage
ORR	Oxygen Reduction Reaction
PEMFC	Polymeric Electrolyte Membrane Fuel Cell
PGM	Precious Group Metal
RHE	Reference Hydrogen Electrode
ROS	Radical Oxygen Species
SHE	Standard Hydrogen Electrode
XANES	X-ray Absorption Near Edge Structure
XPS	X-ray Photoelectron Spectroscopy

Tested Cells

CCL Load $mg\,cm^{-2}$	Nafion in CCL $wt_\%$	UNM Name	MRT Name
1	35	35-35-1 A	1 mg 35% (A)
		35-35-1 B	1 mg 35% (B)
		35-35-1 C	1 mg 35% (C)
1	45	104-45-1 D	1 mg 45% (D)
		104-45-1 E	1 mg 45% (E)
		104-45-1 F	1 mg 45% (F)
2	35	35-35-2 D	2 mg 35% (D)
		35-35-2 E	2 mg 35% (E)
		35-35-2 F	2 mg 35% (F)
2	45	16-45-2 A	2 mg 45% (A)
		16-45-2 B	2 mg 45% (B)
		16-45-2 F	2 mg 45% (F)
4	35	16-45-4 D	4 mg 35% (D)
		16-45-4 E	4 mg 35% (E)
		16-45-4 F	4 mg 35% (F)
4	45	104-35-4 A	4 mg 45% (A)
		104-35-4 B	4 mg 45% (B)
		104-35-4 C	4 mg 45% (C)

Above, the scheme of the samples used during the experimental work is presented. The total number of tested cells is 18, three for each *Cathode Catalyst Layer* loading - Nafion content combination. This is to validate repeatability. It also allows to change the tests scheme within a particular set of samples: the first tested cell represents the base case essential for a comparison when the operating conditions vary. Only in this way the effects of certain phenomena can be evaluated.

The different considerations made during the drafting of the thesis do not take into account the *2 mg 45% (A)* sample, since it has been assembled and tested on a different station that forced the *MEA* to function in a not comparable regime; and the *2 mg 35% (D)* sample since, being the first experiment, its testing has been mainly aimed at validating the functionality of the workstation.

Measuring Instruments

<div style="text-align: right; font-size: xx-large;">B</div>

An attentive description of the different components of the workstation is made in the following paragraphs: technical specifications and functions are presented.

B.1 Potentiostat/Galvanostat

Some diagnostic measures, specifically *CL resistance, CV and LSV*, are obtained by means of the modular potentiostat/galvanostat *Metrohm AUTOLAB PGSTAT30®*. Being able to work as both load and power supply, it allows to carry out these tests where an inert gas (N_2) is used. The frequency range of more than 1 MHz, together with the module *FRA2 (Frequence Response Analyzer)*, allows to carry out suitable impedance spectroscopies. The apparatus is controlled by means of *NOVA* interface, the electrochemistry software from *Metrohm AUTOLAB®*. The combination *PGSTAT30/FRA2* can reveal impedances in potentiostatic and galvanostatic mode in the range of 1 mOhm - 100 GOhm, and capacitances between 0.1 pF and 5000 F.

(a)

Mode	Voltage reading	Fixed voltage
Working range	$\pm 10\,V$	$\pm 10\,V$
Resolution	$300\,\mu V$	$150\,\mu V$
Margin of error	$\pm 0.2\% \pm 2\,mV$	$\pm 0.2\% \pm 2\,mV$

(b)

Mode	Current reading	Fixed current
Working range	$\pm 1.2\,A\,(\pm 10\,A$ if booster on)	$\pm 1.2\,A\,(\pm 10\,A$ if booster on)
Resolution	0.0003%	0.003%
Margin of error	$\pm 0.2\%$	$\pm 0.2\%$

(c)

Frequency Response Analyzer	
Frequency range	$10\,\mu Hz \div 1\,MHz$
Margin of error	$\pm 0.003\%$

B.2 Electronic load

The electronic load has been fundamental to fulfill different tasks in the workstation. Throughout long tests, it has served to force a certain current/voltage value to the fuel cell while reading the voltage/current response at the electrodes. During characterization tests the current has been imposed and the output voltage has been used to build up the polarization curve. The electronic load also absorbs the produced power acting as a dissipating electrical resistance. Lastly it allows a measure of electrochemical impedance spectroscopy in galvanostatic mode.

In this work a model of the series *Chroma DC electronic load 63600* has been employed. In order to have a redundancy check, the device is connected to the computer both via the data acquisition board *NI USB-6210* and via *GPIB (General Purpose Interface Bus)*. So its configuration includes four *senses* (two cables for the anode, two for the cathode) to measure and set the voltage and the current independent from the cable resistance, and the *sources*, through which current flows to the load.

Mode	Voltage reading	Current reading
Working range	$0 \div 80$ V	$0 \div 60$ A
Margin of error	0.5% FS	0.5% FS

B.3 Milliohmmeter

This piece of equipment measures the ohmic resistance of the membrane sending to the fuel cell an alternating current signal with a frequency of 1 kHz, and receiving in response the corresponding value of the membrane impedance.

$$\text{Model:} \quad \text{Tsuruga 3566}$$
$$\text{Margin of error:} \quad 1\,m\Omega \cdot cm^2$$

The milliohmeter communicates with the *LabView*® software by means of the *GPIB*.

B.4 Thermocouples

The working station is equipped with diverse thermocouples in order to monitor the temperature of the components. This device, due to the thermoelectric effect, produces a temperature-dependent voltage which can be interpreted to measure temperature. In this work, six *K-Type* thermocouples have been used. The core materials are Chromel® and Alumel®, very resistant to oxidizing environments. Two

are inserted in small holes in the end plates of the cell, two measure the temperature of the humidity sensors, and two are in the humidifiers. The temperature of the pre-heating tubes is instead read by two *T-Type* thermocouples, which are made by copper and constantan, resistant to humid environments. The data acquisition

Type	K	T
Temperature limits	$-270 \div 1370\,^{\circ}C$	$-270 \div 400\,^{\circ}C$
Calibration range	$40 \div 90\,^{\circ}C$	$40 \div 90\,^{\circ}C$

board *NI USB-9211* receives the signals from the humidifiers and the cell. The external temperature regulator *ASCON Linea M3 Serie $\delta 2$* is instead connected to the pre-heating pipes and the humidity sensors.

B.5 Temperature controllers

The temperature of the cell and the humidifiers is managed by a *PID (Proportional Integrative Derivative)* algorithm developed in *LabView*® environment. The controller acts on glow plugs located in the end plates of the cell and on electrical resistances in the humidifiers, providing thermal energy when necessary, and keeping the system at the desired set-point of $80\,^{\circ}C$. However, if operating conditions deviate from 100% RH, humidifiers' temperature must be modified.

The four *ASCON Linea M3 Serie $\delta 2$* temperature controllers work also by means of a *PID* algorithm, so the signal sent by the thermocouple is compared with the imposed value. The instrument varies the current to the resistance in order to minimize the difference between the two values. This current goes trough specific relay switches, which prevent the passage of too high currents. Specifications follows.

Supply voltage	220 V AC
Input	K/T thermocouple
Output	Electric power
Regulator	*PID*
Resolution	$1\,^{\circ}F$
Relay model	*Carlo Gavazzi* RS1A23D40
Relay control voltage	$4.5 \div 32$ V DC

B.6 Humidity sensors

This instrument, placed in order to analyze the outlet products, connected to the cell by metal tubes, measures the relative humidity of the flux passing through it. It is composed of a probe connected to a control unit, which is able to elaborate the received signal. The probe is basically a porous steeled cap containing a small

capacitive sensor and a thermocouple. The sensor varies its capacity according to the variations of the humidification level of its dielectric, so that it is possible to understand the partial pressure of the vapor within the flow. The temperature of the aluminum casing containing the probe is set through glow plugs to $105\,°C$, so to avoid the presence of water drops, which would distort the humidity measure. It is monitored by a thermocouple, and the water saturation pressure is then obtained. Finally the values of the relative humidity of both anode and cathode outputs are sent to the data acquisition board *NI USB-6210*. Specifications follow.

Model	*Vaisala HMT333*
Probe model	Humicap HMT333
Supply voltage	$10 \div 35$ V DC
Output voltage	$2 \div 10$ V DC
Temperature range	$0 \div 120\,°C$
Margin of error [Temperature]	$\pm 0.1\,°C$ at $22.13\,°C$
Margin of error [Humidity]	$\pm 0.6\%$ RH for 0 - 4% RH $\pm 1.0\%$ RH for 40 - 97% RH

B.7 Flowmeters

Flowmeters are installed so to control and measure the gaseous reactants feeding the fuel cell system. They function by means of an inner valve that allows the passage of the desired quantity of flux. By means of the *LabView*® interface, it is possible to set the flow rate as percentage of the instrument full scale.In this work two identical flowmeters have been used: one for H_2, one for air/O_2 and for N_2.

Model	*Brooks 5850S*
Flow rate range	$0 \div 2$ Nl min^{-1}
Margin of error	0.2% FS - 0.7% FS on the reading
Supply voltage	$15 \div 28$ V DC
Output voltage	$0 \div 5$ V DC

B.8 Humidifiers

The purpose of this appliance is to humidify to the requested level the reactants coming from the flowmeters entering the cell. The gases gurgle across the water filling the humidifier.
Its working conditions are of 100% relative humidity, defined as $RH = \dfrac{p_v}{p_{sat}(T_{hum})}$, where p_v is the partial pressure of the water vapor within the flow and $p_{sat}(T_{hum})$ is the saturation pressure at the humidifier temperature. The cell, on the other hand,

operates at the constant temperature (and so at constant saturation pressure) of $80\,^{\circ}C$. Once the cell *RH* is decided, the consequent change in p_v sets the humidifier temperature. The flows arrive to the cell distribution channel via the pre-heating

Type of test	T_{hum} $[^{\circ}C]$
100% RH	80
90% RH	77.6
80% RH	74.6
60% RH	67.9

pipes, kept at $85\,^{\circ}C$, so that water condensation is minimized while the reactants temperature does not risk to be dangerous for the cell.

B.9 Centrifugal pump

The micro-pump serves to feed the humidifiers with the distilled water needed to humidify the reactants. It is controlled by two electric switches, one for the anode and one for the cathode humidifier. In the present work a *RS® Micropump M200S* has been used. Specifications are the following:

Input voltage	$2 \div 4$ V DC
Power usage	$1.11 \div 2$ W
Flow rate	$507 \div 661$ ml min^{-1}

B.10 Tubing and connections

The passage of the liquid and gaseous flows is assured by *Teflon® PFA* tubes, having an external diameter of 1/8 inches. This flexible thermoplastic material provides good performances, being chemically inert and without corrosion problems in the long run. The connections between tubes or with other components are made with junctions in *stainless steel 316* or brass produced by *Swagelok®*.

B.11 Pressure transducers

The workstation is provided with four pressure transducers, at the inlet and outlet of both anode and cathode, measuring the absolute pressure of reactants and products. The downstream signals are received by the data acquisition board *NI USB-6008*, while the upstream signals by the data acquisition board *NI USB-6210*.

(a) Cathode

Position	Upstream	Downstream
Model	*GE Druck PMP 1400*	*GE Druck PMP 4070*
Full scale	4 bar	3 bar
Supply voltage	$9 \div 30$ V DC	$9 \div 32$ V DC
Output voltage	$0 \div 5$ V DC	$0 \div 5$ V DC

(b) Anode

Position	Upstream and Downstream
Model	*Keller Druck Series 33x*
Full scale	3 bar
Supply voltage	$13 \div 28$ V DC
Output voltage	$0 \div 10$ V DC

B.12 Backpressure regulator

Two backpressure regulators are placed downstream the cell. This device works like a fluid transistor by forming a unique force balance on an flexible membrane between three separate pressures. The body and the cap material are *stainless steel 316*. The fluid inlet pressure and the downstream vent pressure exist on the wetted side of a diaphragm made of *PTFE*, separated by orifices. The pilot air set-point pressure, supplied by a manual pressure regulator, is on the non-wetted side of the diaphragm. It regulates the higher inlet pressure by opening up only as much as necessary to hold back the desired pressure at the inlet.

The tests carried out during the experimental part of the thesis have requested cell operating pressures of $0.5 bar_g$ and $2 bar_g$. Both the two backpressure and the two associated manual pressure regulators has been provided by *Equilibar®*.

(a) Backpressure regulator

Model	GSD6
Maximum working pressure	3 bar
Maxium operating temperature	$200°C$

(b) Manual pressure regulator

Model	10242-Z22435
Maximum supply	35 bar
Range	$0.1 \div 4 bar_{abs}$

Tests

C

Here a complete list of the tests carried out in the experimental work follows, for each one of them the reference name used in the thesis, the operational features and the investigation purpose are clarified.

C.1 Degradation tests

Degradation tests are expected, thanks to their consistent duration, to be able to characterize phenomena of interest influencing the global performance of the cell. Each operational parameter has been set for a specific purpose, whether for the definition of a reference case or for the isolation of a particular response.

C.1.1 Potentiostatic tests

Potentiostatic tests are carried out by fixing the voltage by means of the electronic load or the potentiostat (in the case of tests in Nitrogen) described in *Appendix B*.

(a) [CONT06V] - Continuum 0.6 V

Anode:	60 ml min^{-1} H$_2$
Cathode:	200 ml min^{-1} Air
RH:	100%
BP:	0.5 bar$_g$
Potential:	0.6 V
Duration:	160 h

(b) [CONT06V2BP] - Continuum 0.6 V 2 bar$_g$

Anode:	60 ml min^{-1} H$_2$
Cathode:	200 ml min^{-1} Air
RH:	100%
BP:	2 bar$_g$
Potential:	0.6 V
Duration:	160 h

(c) [N206V] - Nitrogen 0.6 V

Anode:	60 ml min^{-1} H$_2$
Cathode:	200 ml min^{-1} N$_2$
RH:	100 - 80 - 60 %
BP:	0.5 bar$_g$
Potential:	0.6 V
Duration:	10-60 h

(d) [O206V] - Oxygen 0.6 V

Anode:	60 ml min^{-1} H$_2$
Cathode:	100 ml min^{-1} O$_2$
RH:	100%
BP:	0.5 bar$_g$
Potential:	0.6 V
Duration:	160 h

C.1.2 Galvanostatic tests

Galvanostatic tests are carried out by fixing the current to the desired value by means of the electronic load described in *Appendix B*.

(a) [CONT03A] - Continuum 0.3 A

Anode:	60 ml min^{-1} H$_2$
Cathode:	200 ml min^{-1} Air
RH:	100%
BP:	0.5 bar$_g$
Current:	0.3174 A
Duration:	20 h

(b) [CONT05A] - Continuum 0.5 A

Anode:	60 ml min^{-1} H$_2$
Cathode:	200 ml min^{-1} Air
RH:	100%
BP:	0.5 bar$_g$
Current:	0.5 A
Duration:	10-30 h

(c) [CONT1A] - Continuum 1 A

Anode:	60 ml min^{-1} H$_2$
Cathode:	200 ml min^{-1} Air
RH:	100%
BP:	0.5 bar$_g$
Current:	1.058 A
Duration:	10-20 h

(d) [O205A] - Oxygen 0.5 A

Anode:	60 ml min^{-1} H$_2$
Cathode:	200 ml min^{-1} O$_2$
RH:	100%
BP:	0.5 bar$_g$
Current:	0.5 A
Duration:	24 h

C.2 Polarization tests

The polarization curve is the diagnostic technique able to represent in the most immediate way the status of the fuel cell assembly: voltage response to the current density imposed by the electronic load (described in *Appendix B*) is plotted so that the various overpotential contributions can be identified. The parameters common to all the tests are the cell operating temperature of **80°C**, together with the reference point denoted by a current density of **0.025 A cm^{-2}** held for **300 s**. Lastly, also the first applied current after j_{ref} (**0.05 A cm^{-2}**) and the last (**0 A cm^{-2}**) stay the same.

j [A cm^{-2}]	Number of acquisitions
0.05	180
0.1	180
0.15	180
•	
•	180
j_{max}	
•	
•	180
•	
0.05	180
0.025	60

0.015	60
0.01	60
0.005	60
0.002	60
0.001	60
0.0005	60
0.0002	60
0.0001	60
0	35

Each acquisition takes 1 second. The dots indicate increasing values with a 0.05 A cm^{-2} step until j_{max} is reached, and the corresponding descending ones.

C.2.1 Constant flow

In this type of test the flow rates are fixed assuring a λ greater than 10, avoiding different reactant concentrations along the serpentines. This includes procedures with air, O_2 + N_2, or O_2 + He feeding the cathode.

Tests in air   Flows are: 500 ml min^{-1} of H_2 at the anode and 1000 ml min^{-1} of air at the cathode.

(a) [CF]

When:	BOL $\rightarrow$ EOL
RH:	100%
BP:	0.5 bar$_g$
j_{max}	0.4 $\rightarrow$ 0.15/0.2 A cm^{-2}

(b) [CF2]

When:	BOL $\rightarrow$ EOL
RH:	100%
BP:	2 bar$_g$
j_{max}	0.6 $\rightarrow$ 0.3/0.35 A cm^{-2}

(c) [RH80]

When:	EOL
RH:	80%
BP:	0.5 bar$_g$
j_{max}	0.15/0.2 A cm^{-2}

(d) [RH60]

When:	EOL
RH:	60%
BP:	0.5 bar$_g$
j_{max}	0.1/0.2 A cm^{-2}

Tests in pure O_2 + inert   These tests are arranged so to keep the oxygen concentration to the same percentage at which it is present in air (20.9 %). Anodic flux remains 500 ml min^{-1} of H_2, and the cathode is fed with $0.209 \cdot 1000 = 209 \, ml \, min^{-1}$ of O_2 plus $0.791 \cdot 1000 = 791 \, ml \, min^{-1}$ of He or N_2.

(a) [O2N2]		(b) [O2He]	
When:	EOL	When:	EOL
RH:	100%	RH:	100%
BP:	0.5 bar$_g$	BP:	0.5 bar$_g$
j_{max}	0.15 A cm^{-2}	j_{max}	0.15 A cm^{-2}

C.2.2 Constant stoichiometry

This type of polarization has been thought exclusively for tests in pure oxygen, where the whole flow is reacting, eliminating any concentration issue. A λ factor equals to 2 has been chosen. Operating parameters follow:

(a) [O2]	
When:	BOL $\rightarrow$ EOL
RH:	100%
BP:	0.5 bar$_g$
j_{max}	0.8 $\rightarrow$ 0.4 A cm^{-2}

C.3 Electrochemical Impedance Spectroscopy

This type of test has been exploited both in operando and meanwhile polarizations, by means of the electronic load (described in *Appendix B*). The specific *EIS* parameters stay the same, but reactant flow rates, pressures and RH vary according to the kind of procedure that is being carried out.

f_{min}:	0.07 Hz
f_{max}:	20 000 Hz
Number of frequencies:	50
Number of cycles:	5
Time per cycle:	1 s
Sine wave amplitude:	10% I_{DC}

C.4 Tests in Nitrogen

These diagnostic techniques use the inert Nitrogen to feed the cathode, the working electrode to which the voltage is applied by the potentiostat (described in *Appendix B*). As the reactant change requests, these tests are executed only when the degradation ones are terminated. The anode acts as reference electrode. Flow rates are fixed for all the procedures: 50 ml min^{-1} of H_2 and 50 ml min^{-1} of N_2.

C.4.1 Cyclic Voltammetry

In order to qualitatively reason about the effect of degradation tests on the catalytic surface, this diagnostic technique is used at the beginning and at the end of those, under different operating conditions: 0.5 vs 2 bar$_g$, 100 vs 80 vs 60 % RH.

Start potential:	0.1 V
Upper vertex potential:	1 V
Lower vertex potential:	0.05 V
Stop potential:	0.1 V
Number of scans:	10
Scan rate:	0.05 V s^{-1}
Step:	0.000244 V

C.4.2 Linear Sweep Voltammetry

The status of the polymeric membrane of the cell is evaluated at its *EoL*, keeping the operational parameters unchanged so to be able to make consistent comparisons. Flows are thus fully saturated and under a constant pressure of 0.5 bar$_g$.

Start potential:	0.05 V
Stop potential:	0.55 V
Scan rate:	0.001 V s^{-1}
Step:	0.000244 V

C.4.3 Catalyst Layer resistance

The ionic conductivity of Nafion faces the consequences of the series of degradation tests, so that their impact is studied by measuring the membrane resistance both at their beginning and at their end. Operating conditions are adjusted accordingly: 0.5 or 2 bar$_g$, 100, 80 or 60 % RH.

Applied potential:	0.4 V
First applied frequency:	10 000 Hz
Last applied frequency:	1 Hz
Number of frequencies:	10 per decade
Frequency step type:	Points per decade
Amplitude:	0.01 V$_{RMS}$
Wave type:	Sine
Number of repetitions:	3

Bibliography

[1] Saeed Asghari, Ali Mokmeli, and Mahrokh Samavati. „Study of PEM fuel cell performance by electrochemical impedance spectroscopy". In: *International Journal of Hydrogen Energy* 35.17 (2010), pp. 9283–9290 (cit. on p. 41).

[2] Siddharth Komini Babu, Hoon T Chung, Piotr Zelenay, and Shawn Litster. „In-situ through-plane measurements of ionic potential distributions in non-precious metal catalyst electrode for PEFC". In: *ECS Transactions* 69.17 (2015), pp. 23–33 (cit. on p. 7).

[3] Dustin Banham, Siyu Ye, Katie Pei, et al. „A review of the stability and durability of non-precious metal catalysts for the oxygen reduction reaction in proton exchange membrane fuel cells". In: *Journal of Power Sources* 285 (2015), pp. 334–348 (cit. on p. 9).

[4] Frano Barbir. *PEM fuel cells: theory and practice*. Academic Press, 2012 (cit. on p. 3).

[5] ANDREA BARICCI. „A combined experimental and modelling approach for the improved characterization of high temperature PEM fuel cells". PhD thesis. Italy, 2015 (cit. on p. 46).

[6] Florida Solar Energy Center. *Procedure for performing PEM single cell testing*. 2009. URL: https://www1.eere.energy.gov/hydrogenandfuelcells/pdfs/htmwg_may09_pem_single_cell_testing.pdf (cit. on p. 29).

[7] Fanny Charreteur, Frédéric Jaouen, Stéphane Ruggeri, and Jean-Pol Dodelet. „Fe/N/C non-precious catalysts for PEM fuel cells: Influence of the structural parameters of pristine commercial carbon blacks on their activity for oxygen reduction". In: *Electrochimica acta* 53.6 (2008), pp. 2925–2938 (cit. on pp. 7, 8).

[8] Jerzy Chlistunoff. „RRDE and voltammetric study of ORR on pyrolyzed Fe/polyaniline catalyst. On the origins of variable Tafel slopes". In: *The Journal of Physical Chemistry C* 115.14 (2011), pp. 6496–6507 (cit. on p. 12).

[9] Chang Hyuck Choi, Claudio Baldizzone, George Polymeros, et al. „Minimizing operando demetallation of Fe-NC electrocatalysts in acidic medium". In: *ACS Catalysis* 6.5 (2016), pp. 3136–3146 (cit. on pp. 10, 11).

[10] Chang Hyuck Choi, Sung Hyeon Park, and Seong Ihl Woo. „N-doped carbon prepared by pyrolysis of dicyandiamide with various MeCl 2· xH 2 O (Me= Co, Fe, and Ni) composites: effect of type and amount of metal seed on oxygen reduction reactions". In: *Applied Catalysis B: Environmental* 119 (2012), pp. 123–131 (cit. on p. 10).

[11] Ja-Yeon Choi, Lijun Yang, Takeaki Kishimoto, et al. „Is the rapid initial performance loss of Fe/N/C non precious metal catalysts due to micropore flooding?" In: *Energy & Environmental Science* (2017) (cit. on pp. 14, 15, 50).

[12] Office of Energy Efficiency and Renewable Energy. *Multi-Year Research, Development, and Demonstration Plan*. 2016. URL: `https://energy.gov/sites/prod/files/2016/10/f33/fcto_myrdd_fuel_cells.pdf` (cit. on p. 4).

[13] Magali Ferrandon, Xiaoping Wang, A Jeremy Kropf, et al. „Stability of iron species in heat-treated polyaniline–iron–carbon polymer electrolyte fuel cell cathode catalysts". In: *Electrochimica Acta* 110 (2013), pp. 282–291 (cit. on p. 10).

[14] EN Fuller. „Schettle. Pd, JC Giddings". In: *Industrial and Engineering Chemistry* 58 (1966), pp. 19–27 (cit. on p. 47).

[15] Vincent Goellner, Vanessa Armel, Andrea Zitolo, Emiliano Fonda, and Frédéric Jaouen. „Degradation by hydrogen peroxide of metal-nitrogen-carbon catalysts for oxygen reduction". In: *Journal of The Electrochemical Society* 162.6 (2015), H403–H414 (cit. on pp. 12, 60, 94).

[16] Fritz Haber and Joseph Weiss. „The catalytic decomposition of hydrogen peroxide by iron salts". In: *Proceedings of the Royal Society of London A: Mathematical, Physical and Engineering Sciences*. Vol. 147. 861. The Royal Society. 1934, pp. 332–351 (cit. on p. 12).

[17] Taehee Han, Nilesh V Dale, Kev Adjemian, Vijayadurga Nallathambi, and Scott Calabrese Barton. „Electrochemical oxidation of surface oxides to partially recover the performance of non-PGM catalyst under fuel cell operation". In: *ECS Transactions* 41.1 (2011), pp. 2289–2296 (cit. on p. 10).

[18] Juan Herranz, Frédéric Jaouen, Michel Lefèvre, et al. „Unveiling N-protonation and anion-binding effects on Fe/N/C catalysts for O2 reduction in proton-exchange-membrane fuel cells". In: *The Journal of Physical Chemistry C* 115.32 (2011), pp. 16087–16097 (cit. on p. 13).

[19] Edward F Holby and Piotr Zelenay. „Linking structure to function: the search for active sites in non-platinum group metal oxygen reduction reaction catalysts". In: *Nano Energy* 29 (2016), pp. 54–64 (cit. on p. 6).

[20] Frédéric Jaouen and Jean-Pol Dodelet. „O2 reduction mechanism on non-noble metal catalysts for PEM fuel cells. Part I: Experimental rates of O2 electroreduction, H2O2 electroreduction, and H2O2 disproportionation". In: *The Journal of Physical Chemistry C* 113.34 (2009), pp. 15422–15432 (cit. on p. 12).

[21] Frédéric Jaouen, Eric Proietti, Michel Lefèvre, et al. „Recent advances in non-precious metal catalysis for oxygen-reduction reaction in polymer electrolyte fuel cells". In: *Energy & Environmental Science* 4.1 (2011), pp. 114–130 (cit. on p. 6).

[22] Ioannis Katsounaros, Wolfgang B Schneider, Josef C Meier, et al. „Hydrogen peroxide electrochemistry on platinum: towards understanding the oxygen reduction reaction mechanism". In: *Physical Chemistry Chemical Physics* 14.20 (2012), pp. 7384–7391 (cit. on pp. 12, 84).

[23] Shyam Kattel, Plamen Atanassov, and Boris Kiefer. „A density functional theory study of oxygen reduction reaction on non-PGM Fe–N x–C electrocatalysts". In: *Physical Chemistry Chemical Physics* 16.27 (2014), pp. 13800–13806 (cit. on p. 7).

[24] AA Kulikovsky. „A physical model for catalyst layer impedance". In: *Journal of Electro-analytical Chemistry* 669 (2012), pp. 28–34 (cit. on pp. 46, 49).

[25] Michel Lefèvre, Eric Proietti, Frédéric Jaouen, and Jean-Pol Dodelet. „Iron-based catalysts with improved oxygen reduction activity in polymer electrolyte fuel cells". In: *science* 324.5923 (2009), pp. 71–74 (cit. on p. 8).

[26] Nathaniel D Leonard, Kateryna Artyushkova, Barr Halevi, et al. „Modeling of low-temperature fuel cell electrodes using non-precious metal catalysts". In: *Journal of The Electrochemical Society* 162.10 (2015), F1253–F1261 (cit. on pp. 16, 17, 60, 62).

[27] Yuxiu Liu, Michael W Murphy, Daniel R Baker, et al. „Proton conduction and oxygen reduction kinetics in PEM fuel cell cathodes: effects of ionomer-to-carbon ratio and relative humidity". In: *Journal of The Electrochemical Society* 156.8 (2009), B970–B980 (cit. on p. 8).

[28] Zhenyu Liu, Jesse S Wainright, Morton H Litt, and Robert F Savinell. „Study of the oxygen reduction reaction (ORR) at Pt interfaced with phosphoric acid doped polybenzimidazole at elevated temperature and low relative humidity". In: *Electrochimica Acta* 51.19 (2006), pp. 3914–3923 (cit. on p. 46).

[29] Dzmitry Malevich, Barath Ram Jayasankar, Ela Halliop, et al. „On the determination of PEM fuel cell catalyst layer resistance from impedance measurement in h2/n2 cells". In: *Journal of the Electrochemical Society* 159.12 (2012), F888–F895 (cit. on p. 44).

[30] D Malko, A Kucernack, and T Lopes. *In situ electrochemical quantification of active sites in Fe–N/C non-precious metal catalysts*. 2016. URL: http://dx.doi.org/10.1038/ncomms13285 (cit. on p. 6).

[31] W Mérida, DA Harrington, JM Le Canut, and G McLean. „Characterisation of proton exchange membrane fuel cell (PEMFC) failures via electrochemical impedance spectroscopy". In: *Journal of power sources* 161.1 (2006), pp. 264–274 (cit. on p. 41).

[32] Nobuaki Nonoyama, Shinobu Okazaki, Adam Z Weber, Yoshihiro Ikogi, and Toshihiko Yoshida. „Analysis of oxygen-transport diffusion resistance in proton-exchange-membrane fuel cells". In: *Journal of The Electrochemical Society* 158.4 (2011), B416–B423 (cit. on p. 86).

[33] Mark E Orazem and Bernard Tribollet. *Electrochemical impedance spectroscopy*. Vol. 48. John Wiley & Sons, 2011 (cit. on p. 41).

[34] Michael H Robson, Alexey Serov, Kateryna Artyushkova, and Plamen Atanassov. „A mechanistic study of 4-aminoantipyrine and iron derived non-platinum group metal catalyst on the oxygen reduction reaction". In: *Electrochimica Acta* 90 (2013), pp. 656–665 (cit. on p. 88).

[35] Nastaran Ranjbar Sahraie, Ulrike I Kramm, Julian Steinberg, et al. „Quantifying the density and utilization of active sites in non-precious metal oxygen electroreduction catalysts". In: *Nature communications* 6 (2015) (cit. on pp. vii, xi).

[36] DB Spry, A Goun, K Glusac, David E Moilanen, and MD Fayer. „Proton transport and the water environment in nafion fuel cell membranes and AOT reverse micelles". In: *Journal of the American Chemical Society* 129.26 (2007), pp. 8122–8130 (cit. on p. 14).

[37] Sarah Stariha, Kateryna Artyushkova, Alexey Serov, and Plamen Atanassov. „Non-PGM membrane electrode assemblies: Optimization for performance". In: *International Journal of Hydrogen Energy* 40.42 (2015), pp. 14676–14682 (cit. on pp. 8, 9, 21, 38).

[38] Sarah Stariha, Kateryna Artyushkova, Michael J Workman, et al. „PGM-free Fe-NC catalysts for oxygen reduction reaction: Catalyst layer design". In: *Journal of Power Sources* 326 (2016), pp. 43–49 (cit. on p. 8).

[39] Lu Wang, Adriano Ambrosi, and Martin Pumera. „"Metal-Free" Catalytic Oxygen Reduction Reaction on Heteroatom-Doped Graphene is Caused by Trace Metal Impurities". In: *Angewandte Chemie International Edition* 52.51 (2013), pp. 13818–13821 (cit. on p. 6).

[40] D Weng, JS Wainright, U Landau, and RF Savinell. „Electro-osmotic drag coefficient of water and methanol in polymer electrolytes at elevated temperatures". In: *Journal of the Electrochemical Society* 143.4 (1996), pp. 1260–1263 (cit. on p. 48).

[41] Jaclyn D Wiggins-Camacho and Keith J Stevenson. „Mechanistic discussion of the oxygen reduction reaction at nitrogen-doped carbon nanotubes". In: *The Journal of Physical Chemistry C* 115.40 (2011), pp. 20002–20010 (cit. on p. 12).

[42] Gang Wu and Piotr Zelenay. „Nanostructured nonprecious metal catalysts for oxygen reduction reaction". In: *Accounts of chemical research* 46.8 (2013), pp. 1878–1889 (cit. on p. 6).

[43] Gang Wu, Kateryna Artyushkova, Magali Ferrandon, et al. „Performance durability of polyaniline-derived non-precious cathode catalysts". In: *ECS Transactions* 25.1 (2009), pp. 1299–1311 (cit. on p. 12).

[44] Jian Xie, Fan Xu, David L Wood, et al. „Influence of ionomer content on the structure and performance of PEFC membrane electrode assemblies". In: *Electrochimica Acta* 55.24 (2010), pp. 7404–7412 (cit. on p. 22).

[45] Gaixia Zhang, Régis Chenitz, Michel Lefèvre, Shuhui Sun, and Jean-Pol Dodelet. „Is iron involved in the lack of stability of Fe/N/C electrocatalysts used to reduce oxygen at the cathode of PEM fuel cells?" In: *Nano Energy* 29 (2016), pp. 111–125 (cit. on pp. viii, xii, 14, 15).

[46] Eric R Ziegel. *Probability and Statistics for Engineering and the Sciences*. 2004 (cit. on p. 35).

[47] Joseph M Ziegelbauer, Tim S Olson, Svitlana Pylypenko, et al. „Direct spectroscopic observation of the structural origin of peroxide generation from Co-based pyrolyzed porphyrins for ORR applications". In: *The Journal of Physical Chemistry C* 112.24 (2008), pp. 8839–8849 (cit. on p. 6).

[48] Andrea Zitolo, Vincent Goellner, Vanessa Armel, et al. „Identification of catalytic sites for oxygen reduction in iron-and nitrogen-doped graphene materials". In: *Nature materials* 14.9 (2015), pp. 937–942 (cit. on p. 6).

List of Figures

List of Tables